Strategies for improving the outcoupling efficiency in organic light emitting diodes for lighting and display applications

Savanna Rae LLOYD

Japan Advanced Institute of Science and Technology

Doctoral Dissertation

Strategies for improving the outcoupling efficiency in organic light emitting diodes for lighting and display applications

Savanna Rae LLOYD

Supervisor: Hideyuki Murata

Graduate School of Advanced Science and Technology

Japan Advanced Institute of Science and Technology

Materials Science

December 2022

Abstract

Organic light emitting diodes have been able to achieve up to 100% in their internal quantum efficiencies. The realization of 100% in their external quantum efficiencies, however, are limited by the low light outcoupling efficiency (η_{out}) of ~20%. The η_{out} describes the fraction of photons that escape into the forward viewing direction relative to the total amount generated and is heavily influenced by the device structure and materials used. Low η_{out} results from light lost to substrate guided modes (due to light rays being totally internally reflected, TIR, at the air/glass interface) and evanescent modes (due to coupling between the EM radiation and surface plasmons, SPs at the organic/cathode interface). The aim of this research is to enhance η_{out} by targeting these light loss channels via device and materials engineering strategies, respectively.

Hole patterns were first micromachined via a femtosecond laser (IMRA America Inc.) onto the air/glass side of the OLED substrate. Simulated results revealed that the maximum η_{out} maybe realized by using hole patterns with conical shape, 5 μm diameter, 10 μm depth, arranged in a rectangular lattice and separated by 1 μm. Experimental results agreed well with simulation and showed that up to 60% η_{out} enhancement ($\Delta\eta_{out}$) can be achieved in patterned devices. The mechanism of $\Delta\eta_{out}$ is ascribed to the extraction of substrate guided modes where a smaller contact angle is made between the incident light rays and slanted conical surface, therefore TIR events at the air/glass interface can be avoided. Additionally, strong scattering events at the air/glass interface disarray interference effects that would normally cause viewing angle dependence (VAD) of the emission (EL) spectra. VAD was reduced from 11 nm to 4 nm thanks to the substrate patterning. Past strategies for $\Delta\eta_{out}$ have unfortunately resulted in the VAD of the EL spectra while textures used to reduce VAD have no effect on η_{out}. Our strategy represents an improvement milestone in this regard for general lighting OLEDs since our air/glass patterns demonstrate simultaneous $\Delta\eta_{out}$ and reduction of VAD.

A materials engineering approach was used to develop potential strategies that can prevent losses to evanescent modes. π-conjugated polymers used as the emissive layer in OLEDs naturally adopt a horizontal orientation relative to the z-axis and thus emit TE-polarized radiation. Since SPs only couple to TM-polarized radiation, losses to evanescent modes are reduced and η_{out} is enhanced. For the realization of highly efficient OLED displays, these devices must naturally emit linearly polarized luminescence (LPL). This will be achieved by the uniaxial orientation of the polymer's molecular chain and transition dipole moment (TDM) in the x-y plane. For this purpose, we have devised a novel strategy, "solution withdrawal coating (SWC)" for the simultaneous deposition of the polymer film and control over uniaxial orientation. P3HT was used as the proof-of-concept material and demonstrated that up to 0.43 in optical anisotropy is possible. P3HT readily forms solution-state aggregates (nanofibrils) after UV-irradiation and fibrils readily align parallel to the direction of the moving solution during SWC. Although UV-irradiation does not induce molecular aggregation in solution for all OLED polymers (ex. F8BT), other strategies maybe explored, ex. electric field induced alignment. Once solution-state alignment is achieved, uniaxial orientation of polymer chains is expected, and LPL can be realized.

Keywords: Organic light-emitting diodes, outcoupling efficiency, substrate patterning, substrate guided modes, evanescent modes, molecular orientation.

Contents

List of Figures

List of Tables

Chapter 1
Introduction

1.1 Introduction to organic light-emitting diodes

In 1987 Tang and Van Slyke were successful in demonstrating the first novel double-layer electroluminescent device which utilized organic semiconductor materials[1]. Since then, the on-going development of organic light emitting diodes (OLEDs) have revolutionized the general lighting and display market. Unlike their inorganic counterparts (LED/LCD), the OLED offers many advantages such as aesthetic versatility (fabrication on flexible substrates), thinner device structure, wide viewing angle, fast response time and excellent colour quality due to self-emitting materials[2]. Before these devices can be fully adopted as competitive alternatives to LED/LCD sources, challenges related to their light extraction efficiency and practical fabrication processes for large-scale manufacturing must be addressed. In typical bottom-emitting OLEDs the low outcoupling efficiency (η_{out}) of 20% remains one of the limiting factors to achieving high external quantum efficiency (η_{ext}, ratio between photons escaping into air to injected charges)[3]. In a simple OLED architecture that utilizes an isotropic fluorescent emitter, substrate

guided modes and coupling to surface plasmon polariton (SPP, evanescent) modes are two of the largest contributors to light loss. Since no universal strategy exists for simultaneously extracting these modes or suppressing coupling to them in the first place, they will be targeted separately to enhance the η_{out}. The aim of this research is to explore such strategies that are most amenable to large-scale manufacturing (simple, least amount of fabrication steps and scalable) for the two main applications of OLED devices: general lighting and display.

Chapters 2 and 3 will explore the enhancement of η_{out} by the extraction of substrate guided modes through targeting the air/glass interface of the OLED. Past strategies to enhance the η_{out} have usually required complex and multi-step processes for fabrication of the outcoupling structure and are often accompanied by strong colour shifting with increasing viewing angle[4]. On the other hand, scattering/diffusive nanoporous films that have been previously been engineered have no effect on the outcoupling efficiency.[5),6)] This phenomenon may be attributed to the consistent air pockets that maintain an effective refractive index mismatch at the air/nanoporous film/glass interface and does not extract substrate guided modes into air. Our strategy utilizes a simple single-step ytterbium-doped fiber laser to inscribe hole patterns at the air/glass substrate interface of the OLED. The patterns induce a scattering effect that is capable of extracting substrate guided modes and reducing colour shifting in OLEDs fabricated via thermal vacuum

evaporation deposition. Thus, a simultaneous enhancement of the η_{out} and reduction of spectral shifting[7),8)] is achieved since the contact angle at the patterned surface is reduced and light rays are scattered in directions away from the new surface normal. Devices utilizing this strategy are most suited to general lighting applications.

Chapter 4 will explore the enhancement of η_{out} by the suppression of light coupling to evanescent modes through targeting the organic semiconductor/metal interface of the OLED. Common strategies to reduce coupling to these modes often involve disrupting the planarity of organic thin film/cathode interface through the creation of corrugated microcavities.[9)] The complexity of these steps make these strategies unsuitable for large-scale practical manufacturing and display applications. Our strategy utilizes a luminescent π-conjugated polymer as the emitting layer to reduce the coupling to evanescent modes, thanks to its intrinsic horizontal orientation in the *x*-*y* plane (relative to the substrate surface).[10)] To take full advantage of efficiency (that is essential for display applications), the uniaxial orientation of the molecules in the *x*-*y* plane are controlled during the deposition stage using our newly developed 'Solution Withdrawal Coating (SWC)' strategy. Thus, film deposition containing molecules with high degrees of orientation is achieved in a single step. The simplicity of device fabrication and solution processability of these devices makes it amenable to large scale manufacturing and display applications.

Chapter 2
General optical properties of OLEDs

2.1 Light generation in OLEDs

The simple bottom emitting OLED device (Fig. 2.1 (a)) consists of a stack of various thin film organic semiconductor materials (conjugated polymer or small molecule) sandwiched between a reflective cathode and a semi-transparent anode that has been pre-deposited on a transparent substrate (rigid glass or flexible plastic).[1)] Years of technological development have yielded heterojunction multi-layer thin film OLED stacking structures to maximize their device efficiency and performance relative to their working mechanism.[11)] Fig. 2.1 (b) illustrates the general operational mechanism of light production in an OLED. A voltage is applied between the anode and cathode to inject holes through the highest occupied molecular orbital (HOMO) and electrons through the lowest unoccupied molecular orbital (LUMO), respectively, into the nm-thick thin film organic layers.[12)] The electron- and hole- transport layers (ETL, HTL) facilitate the movement of charge carriers via ‘hopping’ mechanism towards the emissive layer (EML) wherein they

generate tightly bound electron-hole pairs (excitons of high binding energy). Electron- and hole- blocking layers (EBL, HBL) prevent the transport of electrons and holes, respectively, past the EML and confine the recombination zone to the EML. The radiative recombination of the excitons and relaxation of the molecular excited state of the EML produces photons. A small portion of the photons are then emitted into free space after travelling through the transparent thin films and substrate and being reflected by the metal cathode. [13)]

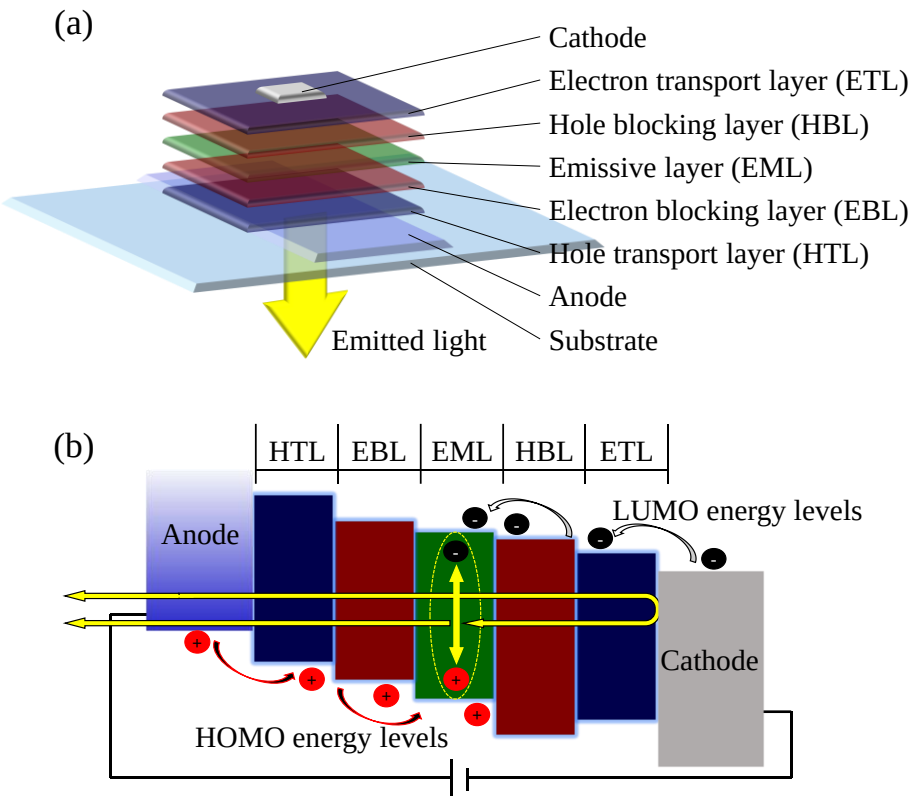

Fig. 2.1 (a) Schematic diagram of OLED and (b) charge transport, exciton generation, recombination process for light generation and emission pathway.

The efficiency of the OLED is therefore greatly dependent on the device structure and the properties of the charge carrier transport and emissive materials. The primary figure of merit used to evaluate OLED device performance is the external quantum efficiency (η_{ext}) which describes the ratio of photons emitted into the effective forward viewing direction (free space) to the number of injected electrons.[13] The η_{ext} can be described by the following equation:

$$\eta_{ext} = \eta_{int} \times \eta_{out} \tag{2.1}$$

where the η_{int} is the internal quantum efficiency and η_{out} is the outcoupling efficiency. η_{int} describes the ratio of internally generated photons to the number of injected electrons and the η_{out} describes the ratio of photons emitted into the effective forward viewing direction to the number of internally generated photons.[14),15)] The η_{int} is described by the following equation:

$$\eta_{int} = \gamma \times \eta_{exc} \times \phi_{PL} \tag{2.2}$$

γ is the charge-balance factor and determines the equality of electrons and holes injected into the device used for exciton formation. η_{exc} is the exciton branching ratio and describes the formation fraction of excitons that are allowed to decay radiatively based on spin-statistics under electrical excitation ϕ_{PL} is the photoluminescence (PL) quantum yield of the emitter in free space. [16)–18)]

The surrounding medium of the device, however, heavily influences the probability of the exciton radiative decay and the emitter's quantum efficiency within the OLED's microcavity (Purcell Effect). To reflect this consideration, Equation 2.1 can be re-written as:

$$\eta_{ext} = \gamma \times \eta_{exc} \times \phi_{eff}(\phi_{PL}, \Gamma) \times \eta_{out}(\Theta, \Gamma) \qquad (2.3)$$

where ϕ_{eff} is the effective quantum yield and is influenced by the ϕ_{PL} and Γ that is the Purcell factor (geometric factor of the device including emission zone position, exciton distance from the cathode and surrounding localized E-field). Indeed, the η_{out} will also be influenced by Γ and Θ, which describes the fraction of horizontally oriented emitting transition dipole moments (TDM) relative to the x-y plane of the substrate. This fraction maybe treated as $\Theta = {}^{p_\parallel}/_{p_\parallel + p_\perp}$ where $p_\parallel$ and $p_\perp$ represent the horizontal and vertical components of the emissive dipole, respectively. [18)–20)] To appreciate this, it must be understood that the molecular excited state of organic semiconducting luminescent species are treated as oscillating electrical dipoles pointing in a specific direction (see Section 2.2.2).[21)]

Advances in materials development have propelled the realization of up to 100% in η_{int} via optimization of the γ, η_{exc} and ϕ_{PL} parameters. A heterojunction device featuring energy band compatibility that facilitate small charge carrier injection barrier at the electrode/organic interface and balanced mobility through

the organic films allow for the realization of unity in γ. The η_{exc} depends on the type of emitter material used where according to spin-statistics, electrical excitation induces the formation of singlet and triplet excited states in a 1:3 ratio. Traditional fluorescent emitters only allow radiative relaxation from singlet excited states thus limiting their η_{exc} to 25%. Conversely, metal-organic complexes in phosphorescent emitters demonstrate strong spin-orbit coupling thus allowing radiative relaxation from both singlet and triplet excited states and realization of 100% in η_{exc}.[22)–24)] High ϕ_{PL} nearing 100% have been realized in thermally activated delayed fluorescent (TADF) emitter materials via the reverse intersystem crossing mechanism that up-converts triplets to singlet excitons.[25),26)] In summary, 100% in η_{int} have been realized by choosing the appropriate emitter materials.

The η_{out} for a bottom-emitting OLED device featuring a reflective cathode, transparent anode, utilizing an isotropic dipole emitter and absent an outcoupling structure can be approximated by the following equation (based on classical geometric ray optics):

$$\eta_{out} = 1 - \sqrt{1 - \left(\frac{1}{n_{org}^2}\right)} \approx \frac{1}{2n_{org}^2} \tag{2.4}$$

where n_{org} is the refractive index of the EML. Organic semiconductor emitters usually have a refractive index between 1.7 - 1.8, thus η_{out} maybe approximated to be 20%.[14),27)–29)] The maximum theoretical limit of η_{ext} for an OLED utilizing a

highly efficient phosphorescent/TADF emitter is therefore less than 20% based on Equation 2.1, where η_{out} is the limiting factor preventing OLED from achieving their full performance potential. To fully realize 100% in η_{ext} in OLEDs, attention must be given to optimizing the η_{out} parameter.

2.2 Outcoupled modes and light loss channels

The ~20% η_{out} in OLEDs is a result of the photons able to escape the device and into the free space perpendicular to the x-y plane of the substrate and are known as outcoupled modes. Approximately 80% of generated photons being trapped within the device itself are due to light loss channels borne out of the OLEDs inherent structure and are known as guided modes. These light loss mechanisms can therefore be assigned to specific interfaces along the OLED structure where such losses occur. Fig. 2.2 illustrates the air/substrate, substrate/organic and organic/metal interfaces where light is reflected and trapped in the substrate as substrate guided modes, trapped within the thin film organic layers as organic waveguided modes and coupled to surface plasmon polaritons (SPPs) as evanescent modes, respectively.[30),31)] The absolute contributions depend on the emitter used and device structure. The mathematical explanations behind their mechanisms will be separated into a geometric ray-optics or wave-optics treatment which are necessary for the appropriate description of their propagation in media with thicknesses either greater than or on the order of the wavelength of light.

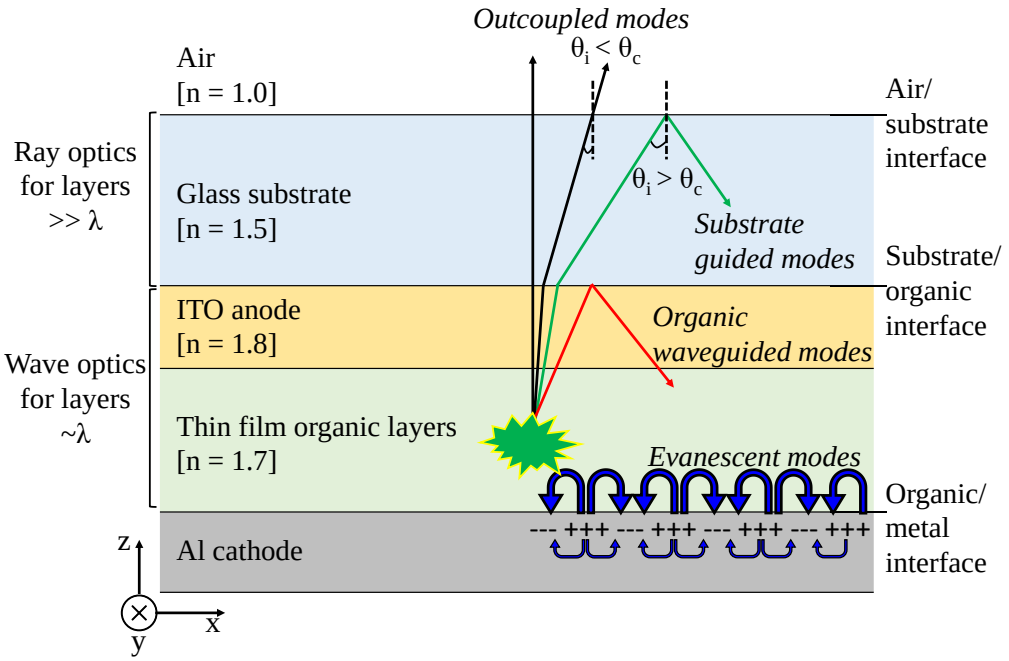

Fig. 2.2 Schematic cross-sectional diagram of the outcoupled modes and light loss mechanisms (substrate guided, organic waveguided and evanescent modes) following photon generation in OLEDs. The typical refractive index (n) of the thin films have been defined around the wavelength of 520 nm.

2.2.1 Substrate and organic waveguided modes

Since the wavelength of visible light (400 – 700 nm) is much smaller than the thickness of the glass substrate (0.70 mm), it may be considered as a homogenous and optically thick incoherent layer. Using a simplified geometric ray optic treatment of light is therefore adequate for explaining the optical effects leading to substrate guided mechanisms.

After photons are generated within the emissive layer, they travel through the thin films, enter the glass substrate, and escape the device into the forward viewing direction of air. The refractive index (n) mismatch between air (n_{air} = 1.0) and the glass substrate (n_{glass} = 1.5) only permit light rays within a limited range of incident angles (θ_i) to escape when impinging on the air/substrate interface (Fig. 2.2). All θ are defined by the angle between the light propagation direction and surface normal. This phenomenon is governed by Snell's law which relates the angle of incidence (θ_1) to the angle of refraction (θ_2) for light rays propagating from one medium (n_1) into another (n_2) and is described by Equation 2.5.

$$n_1 \sin\theta_1 = n_2 \sin\theta_2 \tag{2.5}$$

At the critical angle of incidence (θ_c), the light rays are no longer refracted into free space but instead propagate along the surface of the substrate (θ_2 = 90^o). Equation 2.5 can therefore be re-written as Equation 2.6 to reflect this condition.

$$\theta_c = \sin^{-1}\left(\frac{n_2}{n_2}\right) \tag{2.6}$$

Light rays impinging on the air/substrate interface at angles greater than the θ_c will experience total internal reflection (TIR) and will therefore be trapped within the substrate as substrate guided modes. They may also undergo multiple reflection events between the air/substrate and substrate/organic interface before eventually escaping through the edge of the substrate. Due to the low reflectivity of the

underlying organic layers, these reflection events will be dampened. Outcoupled and substrate guided modes are therefore incident rays which impinge on the air/substrate interface within ($0 \leq \theta_i < \theta_c$) and outside ($\theta_i \geq \theta_c$) the cone of the critical angle, respectively.

A geometric-ray optic approach to understanding the mechanism of organic waveguided modes can be considered in a similar fashion to substrate guided modes; the refractive index mismatch between the glass substrate (n_{glass} = 1.5) and organic layers (where n_{org} can range from 1.7 to 2.1)[32] induces a cone of critical angle condition for rays meeting this substrate/organic interface. Light rays incident at angles greater than θ_c will experience TIR, be trapped and guided within the organic layers. This explanation, however, is over-simplified and is better described by the classical electromagnetic (EM) wave-optics model (CPS model) since the wavelength of light (400 – 700 nm) and the thickness of the organic thin films (150 – 200 nm) are of similar order. The CPS model considers the OLED to be a multilayer microcavity that is embedded with dipole emitters and thus is able to predict the fraction of outcoupled and guided modes by taking into account the Purcell factor and orientation of TDM.[33),34)]

The concept of the in-plane component of the wavevector (k_x) will first be introduced to understand the wave-optics model and its role in classifying outcoupled and guided mode distribution within a bottom-emitting OLED. According to the de Broglie relation ($\vec{p} = h\vec{k}$), the wavevector ($\vec{k}$) includes information about a waves' propagation direction and media.[35] Maxwell's equations ensures the conservation of $\vec{k}$ across all boundaries and dielectric media.[36] Fig. 2.3 shows the orientation of k_x relative to the OLED plane and the simulated power dissipation to various modes based on a simple device structure.

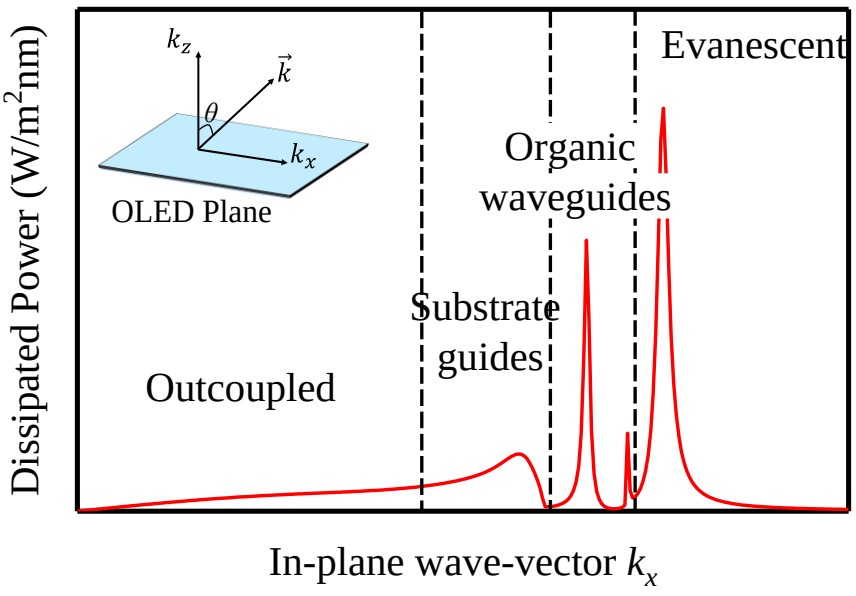

Fig. 2.3 Simulated power dissipation as a function of the in-plane wavevector for an isotropic dipole emitter (inset shows wavevector orientation).

Equation 2.7 describes the definition of the in-plane component of the wavevector

$$k_x = \left|\vec{k}\right| \sin\theta \tag{2.7}$$

where $\left|\vec{k}\right|$ is the scalar quantity and magnitude of the wavevector and θ is the travelling angle of light with respect to the surface normal. Equation 2.7 can be re-written to reflect the magnitude of $\left|\vec{k}\right|$ as described by Equation 2.8,

$$k_x = \frac{2\pi n}{\lambda} \sin\theta \tag{2.8}$$

where n is the refractive index of the media within which the light wave propagates and λ is the wavelength in vacuum. For n = 1, the free space wavevector maybe defined as $k_o = {}^{2\pi}/_{\lambda} = {}^{\omega}/_{c}$, where ω is the angular frequency and c is the speed of light in a vacuum. A dispersion relation describes the distribution of radiation coupled to the various modes and for simplicity, their boundaries or 'kinematic limits of propagation' can be explained in terms of k_o.[2),37)]

According to this dispersion relationship wavevectors propagating between within the range $0 \leq k_x < k_o$ will be coupled into free space as outcoupled modes. Wavevectors with a magnitude of k_o will propagate on the surface and not be counted as far-field emission. Wavevectors whose magnitude lies within the range of $k_o < k_x < n_{glass}k_o$ will be trapped within the substrate as substrate guided modes due to TIR at the air/substrate interface. Multiple damped TIR events (due to the

low reflectivity of the underlying organic layers) will eventually lead to their escape through the edge of the substrate. Since their escape is not into the useful far-field in the direction of the surface normal, they do not count towards outcoupled modes.

Wavevectors that lie within the range of $n_{glass}k_o \leq k_x < n_{organic}k_o$ will be trapped within the organic layers as organic waveguided modes.[38),39)] The slab waveguide formed by the optical cavity may lead to the parasitic absorption light by the transparent thin organic films or aid their escape through the edges of the device.[40)]

Wavevectors with a magnitude $k_x \geq n_{organic}k_o$ experience coupling to surface plasmon polaritons and are lost as evanescent modes and will be discussed in more detail in the next section.[38),39)]

2.2.2 Evanescent modes

The continuous repelling and relocation of free electrons by surrounding localized excess charges at the surface of the metal gives rise to plasmonic oscillations. Their constant relocation induces a fluctuating electron charge density having a parallel and perpendicular E-field component at the organic/metal interface, resulting in surface plasmons (SPs). The coupling between SPs and photons give rise to SPPs otherwise known as evanescent modes.[41)] The SPP wavevector (k_{SPP}) is given by Equation 2.9 where ε_m and ε_d are the complex dielectric function of the metal and organic layer, respectively.[19),38),42)–44)]

$$k_{SPP} = k_o \sqrt{\frac{\varepsilon_m \varepsilon_d}{\varepsilon_m + \varepsilon_d}} = \frac{\omega}{c} \sqrt{\frac{\varepsilon_m \varepsilon_d}{\varepsilon_m + \varepsilon_d}} \quad (2.9)$$

Since surface plasmons are largely p-polarized since they propagate perpendicularly relative to the x-y plane of the OLED and will solely be excited by the p-polarized radiation of light. The loss to evanescent modes is largely influenced by the orientation of the TDM and the resulting polarization state of its radiative emission. SPs exhibit p-polarized modes and thus propagate along the boundary of the organic/metal interface, perpendicular to OLED's *x-y* plane. Thus, the SPs will only be excited by radiation of a similar polarization state within the near-field and its effect diminishes with increasing distance between the location of exciton formation and metal surface (organic/metal interface).[2),42),45)]

The polarization state of the TDM far-field emission is strongest in the direction perpendicular to the TDM's orientational vector. The classical emission of isotropic dipoles can be decomposed into three main combinations of orthogonal dipoles: horizontal-TE, horizontal-TM and vertical-TM.[46)] The horizontal and vertical assignment refer to orientation of the TDM either parallel or perpendicular to x-y plane of the OLED. TE and TM represent the transverse electric and transverse magnetic polarization of light, respectively, where TE-polarizations and TM-polarizations support the propagation of s-polarized and p-polarized waves, respectively (Fig. 2.4). Only the p-polarized light produced by TDM of

perpendicular orientation will excite SPs and lead to evanescent mode losses thus TDM orientation is a very important factor that affects η_{out}. With some exceptions, most vacuum deposited small molecule amorphous emitters usually adopt an isotropic orientation while most polymeric systems deposited from solution adopt a preferential horizontal orientation.[21),47)]

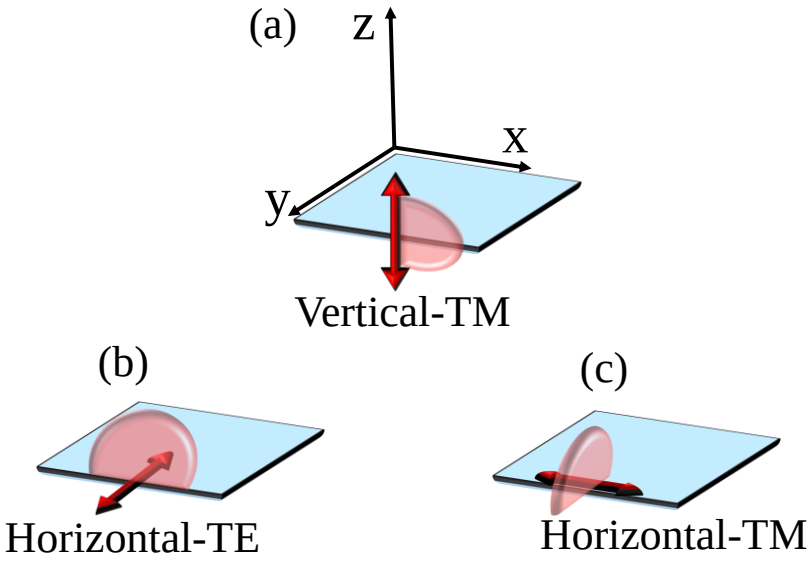

Fig. 2.4 Orthogonal orientations of TDMs (represented by red arrow) and the direction of their far field emission (transparent red semi-circle).

2.3 Studies to improve the outcoupling efficiency in OLEDs via interface modulation

Efforts to improve the η_{out} in OLEDs have relied on extracting guided modes and or reducing the coupling events between the emitted radiation and SPs. The approaches used in these studies encompass both device and materials engineering approaches wherein the 3 main interfacial sites for light loss are targeted. It is sometimes difficult to separate the strategies into the light loss channels they target since one mode may have a cascading 'domino' effect on the other.[48] Fig. 2.5 illustrates some of the most popular strategies for improving the η_{out} in OLEDs.

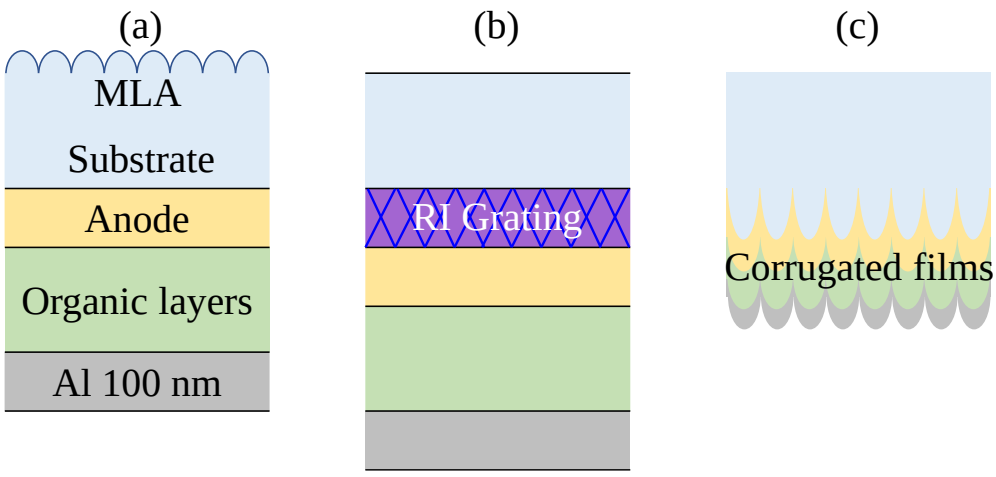

Fig. 2.5 Examples of device engineering strategies used to increase the outcoupling efficiency by targeting the (a) air/substrate (MLA) (b) substrate/organic (RI grating) and (c) organic/metal interface (corrugations).

2.3.1 Air/substrate interface

Successful device engineering strategies that have targeted the air/substrate interface to extract substrate guided modes include the fabrication of both nm- and μm size scattering structures. Externally fabricated microlens arrays (MLA) are one of the most popular strategies for extracting substrate guided modes via scattering mechanisms. Past research have shown successful enhancement in η_{out} by utilizing MLA of different shapes (pyramidal, hemispherical) arranged in a well-defined and ordered lattice[32),49)–51)] and those with random orientation (wrinkle like MLA).[52)] A polydimethylsiloxane (PDMS)-based MLA has also been incorporated with colour conversion phosphors (red and green) to down convert the purely blue emitted light from the OLED into white light while also enhancing the outcoupling efficiency.[53)] Nanolens arrays (NLA) have demonstrated the most success in experiment with randomly arranged corrugated structures at the air/substrate interface [54)] while those with well-defined features (shape, height, periodicity, etc.) have only been demonstrated in simulation.[55)] There have been reports of structures combining both μm- and nm-sized features to create the scattering medium. One study used inspiration from the firefly lantern's ultrastructure (nm-scale trenches arranged in μm-scale periodicities and height) to create a UV-resin replica as the textured scattering layer[56)] while other studies utilize nm-scale diffusive particles as a thin monolayer in polystyrene over the glass substrate[57)] or embedded into a planarized

μm-thick polymer matrix layer[58),59)]. Instead of embedding particles, other studies have utilized air voids as scattering centres for redirecting originally substrate guided modes.[60)] Common among these structures is that they rely on the mechanism of scattering and widening the cone of the critical angle at the air/glass interface. The light rays impinging at the air/glass interface are intended to impinge on the curved surface of the micro or nanolens structure at an angle smaller than the critical angle and thus escape into the forward viewing direction as outcoupled modes.

2.3.2 Substrate/organic interface

Enhancing the η_{out} via extraction of organic waveguided modes typically target device modifications at the substrate/organic interface where extraction of organic waveguided modes into outcoupled modes typically rely on the 'domino effect'. This phenomenon involves the extraction of organic waveguided modes into the substrate which can be extracted later by externally attached outcoupling structures. Popular non-textured strategies to extract organic waveguided modes include using a high refractive index (HRI) substrate, where $n_{HIR} > n_{substrate}$. Here, the refractive index mismatch between the substrate and organic layers which perpetrates organic waveguided modes in the first instance is eliminated. A cone of the critical angle is also eliminated since light rays will now propagate from a media of low refractive index (organic layers) into media of higher refractive index (HRI

substrate).[61)–63)] By combining this technique with an external scattering structure, the organic waveguided modes that have been guided into the substrate maybe extracted and confirmed experimentally. Conversely, other studies have used low refractive index (LRI) materials between the substrate (ex. hydrophobic silica aerogel) and a very thin (50 nm) EML to eliminate losses to organic waveguided modes in the first instance so generated light will either be limited by substrate guided modes only.[27)]

Redirecting organic waveguided modes using refractive index modulation has been achieved via refractive index grids that typically consist of a nm-thick layer that blends both LRI and HRI materials in a well-defined μm-size or nm-size dimensions inserted between the substrate and organic layers.[32),51),64)] In one study, the HRI indium tin oxide (ITO) anode (n_{ITO} = 1.8) was etched into trench like formation and a LIR magnesium fluoride MgF_2 (n_{MgF2} = 1.38) was used to fill the voids in a columnar like structure.[65)] Other studies have used titanium dioxide (TiO_2) and silicon dioxide (SiO_2) as the HRI matrix and LRI grid materials, respectively.[55),66)] The refractive index grid mechanism combines both a scattering and refractive index matching function to allow the propagation of originally waveguided modes into the substrate. Other studies use alternative scattering approach: LRI SiO_2 nanoparticles (as scattering centres)[59)] either within a LRI

matrix of solution processable HTL[67] or HRI TiO_2 to encourage coupling of organic waveguided modes into the substrate.[68]

2.3.3 Organic/metal interface

The most popular textured technique for reducing losses to evanescent modes involves depositing the organic layers over random or ordered nm-scale structures meant to induce nm-scale wave-like undulations in the subsequent layers (Fig. 2.5 (c)). The well-defined structures used to create these undulations are known as Bragg-diffraction gratings or 2D periodical corrugations. Since energy and momentum are not conserved simultaneously for SPP modes they are confined to the organic/metal interface and do not couple to far-field radiation. By choosing an appropriate grating period, the SPP wavevector may gain momentum and overlap to the guided mode wavevector and later be extracted into free space. The Bragg diffraction grating scattering mechanism is described by Equation 2.10 where k'_{SPP}, λ_g and m is the wavevector for the new SPP mode, grating period of the structure and scattering order respectively.[69]

$$k'_{SPP} = k_{SPP} \pm m\frac{2\pi}{\lambda_g} \qquad (2.10)$$

For these structures to be effective and have maximum interactive strength with SPPs, the corrugations must be fabricated on the nm-scale (also in accordance with the wavelength of light).

The nm-scale dimensions of well-defined periodical grating structures made at the organic/metal interface have been optimized in many numerical-based studies[70] while photonic crystals fabricated via nanoimprinting lithography techniques have been experimentally successful in surface plasmon resonance (SPR).[71] Other experimental-based studies have had to employ creative techniques for the fabrication of OLED devices over quasi-random Bragg-diffraction structures etched into the substrate and or anode surface; the most common being deposition of the layers via solution processes (spin-coating). Undulations in the subsequently deposited layers have been achieved via moulds created from nm-scale patterned elastomeric perfluoropolyether (PFPE)[72], treating the substrate surface with sand-blasting and post polishing[73] or RIE etching of nm-monolayer-silica array particles over glass[74] and sapphire substrates[75].

Conversely, there are many non-textured approaches to reduce the formation of evanescent modes. Simulations based on the CPS-model reveal that appropriate tuning of the anode and organic layers[76] can lead to the confinement the emission zone position furthest away from the metal cathode (usually around the second antinode of outcoupling).[77] These approaches, however, may not be realistic for practical OLED devices since they will require high driving voltage due to very thick layers. Removing the metal cathode to eliminate SP formation at the organic/metal interface all together have proven efficient for enhancing the $\eta_{out.}$

Semi-transparent electrode alternatives include indium zinc oxide (IZO) wherein there is simultaneous top and bottom emission[78] and near zero evanescent mode formation. Other approaches have targeted refractive index modulation where either the ETL or EML refractive index is reduced. This has been confirmed in simulation[79] and later via experiment by depositing the EML/ETL at an oblique angle wherein its refractive index was reduced by 17%.[43] The lower refractive index caused the SPP wavevector to shift closer to the outcoupled mode line, thus reducing non-radiative coupling between light emitted from the EML/ETL material and SPs. (Equation 2.9). Control over coupling to SPs can also be tuned by choice of emitter based on intrinsic orientation during deposition. As mentioned in Section 2.2.2, the emission from vertically oriented TDM couple strongly to the TM-polarized SPs. Controlling the orientation of the emitter's TDM is of paramount importance to reducing coupling to the SPs and improving η_{out}. Most solution processed polymers that are typically deposited via spin coating naturally adopt in-plane orientation[80] while vacuum deposited TADF materials have demonstrated very high horizontal orientation factors due to their high molecular planarity. In addition to their high PLQY, their resulting emission couples weakly to SPs and devices including these materials demonstrate high η_{ext} from high η_{out} and η_{int}.[81,82]

2.3.4 Simultaneous modulation at multiple interfaces

The strategies mentioned previously have been useful in improving the η_{out} by targeting only one channel of light loss. There exists, however, other reports that have fabricated outcoupling structures at one interface capable of targeting more than one light loss channel simultaneously. For example simultaneous redirection of organic waveguided modes and excitation of SPPs into SPR have been achieved by inducing wave-like undulations in the organic and metal layers from pre-patterned moulds located between the substrate and anode on both the μm-scale[83),84)] and nm-scale[4),69),84)].

2.4 Issues associated with the inclusion of outcoupling structures

2.4.1 Fabrication processes

The fabrication of the textured outcoupling structures discussed in the previous sections may include multiple complex steps and can be very time consuming. For example, the typical fabrication steps of MLAs include the programming of the design, deposition of a photoresist, optical lithography, resist development and multiple stamping with a PDMS master mould and reflow processes over flexible poly(methyl methacrylate) (PMMA) to imprint the periodic

structure.[40] Fabricating nm-scale patterning of the substrate/anode surface and subsequent deposition of the organic and metal thin films to create wave-like undulations for the extraction of organic waveguided and or evanescent modes is equally challenging. For outcoupling structures to be realistically incorporated into end-user manufacturing, simpler and efficient techniques would be most desirable.

2.4.2 Viewing angle dependence in bottom-emitting OLEDs

OLEDs intrinsically suffer from viewing angle dependence wherein the apparent colour of the device appears to change when the viewing angle relative to the surface normal is increased. This phenomenon is perpetuated by the weak microcavity formed between the highly reflective cathode and weakly reflective anode. Since the thickness of the organic layers between the anode and cathode are on the same order as the wavelength of emitted light (100's of nanometers), this microcavity is resonant for only one optical mode. For a Fabry-Perot cavity, the emitted light intensity I (λ, θ_{air}) for each wavelength (λ) and viewing angle relative to the normal direction (θ_{air}) can be described by Equation 2.11. R_t (R_b) is the reflectivity of the top (bottom) electrode, $\Delta\phi_t$ ($\Delta\phi_b$) is the phase difference between the forward propagating and reflected light from the top (bottom) electrode. Equation 2.12 and Equation 2.13 define $\Delta\phi_t$ and $\Delta\phi_b$, respectively, where d_t (d_b) is

the distance from the emission zone to the top (bottom) electrode, φ_t (φ_b) is the phase change after reflection at the top (bottom) electrode and θ_{org} is the

$$(\lambda, \theta_{air}) = I_o(\lambda) \cdot (1 - R_t) \cdot \frac{1 + R_b + 2\sqrt{R_b}\cos\Delta\phi_b}{1 + R_t R_b - 2\sqrt{R_t R_b}\cos(\Delta\phi_t + \Delta\phi_b)} \quad (2.11)$$

$$\Delta\phi_t = \frac{2\pi}{\lambda} 2nd_t \cos\theta_{org} - \varphi_t \quad (2.12)$$

$$\Delta\phi_b = \frac{2\pi}{\lambda} 2nd_b \cos\theta_{org} - \varphi_b \quad (2.13)$$

propagation angle of light within the organic layers. Since the anode is much less reflective than the cathode, I (λ, θ_{air}) is mainly influenced by R_b and $\Delta\phi_b$. When the viewing angle relative to the surface normal increases, cos(θ_{org}) decreases and so too does the wavelength supported by the cavity. This leads to an apparent 'blue-shift' in the colour of the emitted spectrum.[85)]

To suppress the viewing angle dependence in OLEDs, transparent nanoporous polymer thin films have been attached to the air/glass interface of the device. These films promote the scattering of light to reduce the interference effect that causes colour shifting in the first instance. The limitation with these structures, however, is they have no effect (enhancement nor reduction) on the η_{out}.[5),6)] For outcoupling structures intended to enhance the η_{out} (as discussed in Section 2.3) the

colour shifting problem may be enhanced. This effect is typically observed with outcoupling structures fabricated on the nm-size scale (ex. Bragg-diffraction gratings)[4),86)–89)] since these outcoupling structures support only a very small range of emitted wavelengths in the forward viewing direction. To the best our knowledge, no outcoupling structure has demonstrated simultaneous enhancement in η_{out} and suppression of viewing angle dependence in OLEDs.

2.5 Aim of the study

My research focuses on improving the outcoupling efficiency of OLEDs by targeting 2 of the main modes of light loss: substrate guided modes and evanescent modes. Consideration for outcoupling techniques that are most amenable large-scale manufacturing (simple steps, low cost, high scalability, etc.) while not compromising viewing angle-dependence will be explored.

Chapter 3
Extraction of substrate guided modes via substrate patterning

3.1 Introduction

The ability of OLEDs to be fabricated over flexible substrates has broadened their applicability to a wide range of versatile aesthetic purposes. For example, they may be used for foldable[90),91)] and wearable[92),93)] displays and lighting sources. The general lighting and display applications of OLEDs demand high η_{ext} for conserved power consumption while achieving high brightness and good colour quality over wide viewing angles with Lambertian-like distribution to preserve the image quality.[94)] Methods amenable to their large scale fabrication typically favour solution processes (ex. inkjet, roll-to-roll manufacturing) over vapour deposition processes to deposit the organic semiconducting materials.[95)] The use of poly(3,4-ethlenedioxythiophene) polystyrene sulfonate (PEDOT:PSS) is a widely used solution processable material that may function as a supplementary anode or

HTL.[96)–98)] Unfortunately, its inclusion in the OLED may greatly compromise the intrinsic transmissivity of radiation through the glass substrate and reduce the η_{out} if a thick layer (60 – 100 nm) is required. Therefore, it is imperative that devices of both high and low intrinsic transmittance be included in the studies of enhancing the η_{out} and preservation of viewing angle dependence.

Past efforts to enhance η_{out} by introducing patterns at the air/substrate interface of the device typically involve protruding structures (ex. MLA or NLA) that have no effect on or promote viewing angle dependence. Recently, another study has employed the femtosecond (fs) laser to inscribe μm-sized inverted structures over flexible OLED substrates to enhance the η_{out} where the dimensions of their patterns included holes of diameters ≥ 30 μm with spacings up to 150 μm.[99)] The large separation between the patterns and low density of holes, however, are not amenable for the suppression of viewing angle dependence since the scattering power of the patterned substrate is likely to be low.

The aim of this study will be to employ patterning at the air/substrate interface (over the glass substrate surface) to enhance the η_{out} while simultaneously suppressing the viewing angle dependence. μm-scale patterns will be targeted since nm-sized structures are known to induce strong viewing angle dependence. To enhance the scattering power of the hole patterns, smaller periodicity and greater hole density compared to past studies as mentioned earlier will be employed while

the influence of hole shape will also be investigated. To demonstrate the impact of the patterns on the η_{out} and viewing angle dependence, a simple 'proof of concept' vacuum evaporated OLED with high and low transmittance will be studied. Using highly efficient, state-of-the-art emitter materials for high η_{int} is not of primary focus here since the main concern involves purely optical effects of generated light. Similar results are expected to be obtained for other device structures with high η_{int}.

3.2 Experimental

3.2.1 Femtosecond laser patterning

The chosen technology for creating the air/substrate hole patterns inscribed into the glass substrate is the femtosecond (fs) laser developed by IMRA America Inc. Advances in fs-laser technology has propelled their applications in many fields including the medical field as corrective eye surgery (ophthalmological surgery; laser-assisted in situ keratomileusis (LASIK))[100], industrial fields as photolithographic applications[101], biological sciences for cutting samples[102] and 3D micromachining of channels used in microfluidic devices.[103,104] Unlike picosecond (ps) lasers, the ultra-short pulses from a fs-laser allow for the accurate and precise machining of desired patterns (down to μm-scale) onto both glass and flexible plastic substrates with very fine detailing and little to no post processing. Since the pulse durations in ps-lasers are longer, the machining surface requires

longer exposure time for material changes to be induced. This will eventually lead to heating, thermal tensions, shock wave propagation, etc. all of which cause damage to the surface and compromise the intrinsic material characteristics.[105)–107)] Thus, fs-lasers are most desirable for small scale (μm-dimensional) patterning purposes and simplify the outcoupling structure fabrication process due to its 'one-step' feasibility.

The mechanism of using fs-lasers for micromachining relies on the induced optical breakdown that results result from a laser beam irradiating a sample and ionizing the electrons which transfer energy to the surrounding lattice.[105)] The mechanism of structural damage will be different dependent on the target class of material since this process is also driven by absorption and therefore optical bandgap properties.[108)] The optical bandgap (E_B) of transparent insulators (as is the case for glass and most flexible substrates) are much greater than the photon (E_p) thus the electronic transitions are forbidden. The mechanism for light absorption from the laser must therefore be nonlinear where the E-field strength of the laser must be approximately equal to the E-field energy binding the valence electrons in the atoms (~10^9 V/m). This is realized by utilizing high intensity laser pulses that have tight focus.[105)] Due to the ultra-short pulse nature of fs-laser irradiation, the ablation process is considered a direct solid to vapour transition. Since the fs-laser pulse is less than 1 ps, the electron excitation time is smaller than the time required

for electron-phonon scattering which occurs on a timescale of 1-10 ps. The fs pulse will be terminated before the electrons can thermally excite ions and cause diffusive heating throughout the sample and outside of the target focally irradiated area.[105)] Fs-lasers therefore have much smaller heat affected zone (HAZ) that result in material expulsion and debris compared to lasers with longer pulse duration times.

3.2.2 SETFOS simulation programme optical models

The simulation programme, SETFOS 5.1.2, FLUXiM AG will be used to simulate the mode contributions within the OLED and optimize the dimensions of the glass patterns made at the air/substrate interface. SETFOS is a simulation software specifically designed for organic and perovskite solar cells and LEDs. The optical models employed in SETFOS assume that the emission characteristics of a dipole are similar to that of a Hertzian dipole and the far field emission characteristics are dominated by the interference effects from the surrounding optical multilayer within which the dipole is embedded.[33),34)] Additionally, when defining the multilayer stack (including substrate, thin film organic layers and metal cathode), the simulation assumes the EML is transparent, the planes of the films are infinitely extended along the x-direction and the planes of the films are lossy. Lossy dielectrics are assumed as media where a fraction of the EM radiation decreases exponentially during and within the direction of propagation.

The oscillating dipole moment $\vec{p}$ in the SETFOS model is defined by Equation 3.1 where b_o is the intrinsic power of the dipole, ω is the undamped oscillator frequency, m is the effective mass of the dipole, e is elementary charge and $E_R(\omega)$ is the interface-reflected field at the dipole position. The radiative power of vertically ($\perp$) and horizontally ($\parallel$) dipoles in a birefringent emitter is defined by Equation 3.2 and Equation 3.3, respectively.

$$\frac{d^2}{dt^2}\vec{p} + b_o\frac{d\vec{p}}{dt} + \omega^2\vec{p} = \frac{e^2}{m}E_R(\omega) \tag{3.1}$$

$$q_o b_{o\perp} = \frac{|p|^2\omega k_o^3}{12\pi\varepsilon_o}n_{or} \tag{3.2}$$

$$q_o b_{o\parallel} = \frac{|p|^2\omega k_o^3}{12\pi\varepsilon_o}n_{or}\left(\frac{3n_{or}^2 + 3n_{ex}^2}{4n_{or}^2}\right) \tag{3.3}$$

n_{or}, n_{ex}, q_o, k_o is the ordinary refractive index, extraordinary refractive index, intrinsic quantum efficiency and free space wavevector. The impact of the optical environment on the radiative part of the dipole (via optical feedback due to interference effects) is given by Equation 3.4 where b is the power of the dipole within the optical cavity and F is the Purcell factor and described by Equation 3.5. $f(u)$ describes the infinitesimal radiation of a dipole for an angle at any given position, for all wavelengths and accounts for the optical feedback of the multilayer structure of the OLED device.

$$b = q_o b_o F + (1 - q_o) b_o \tag{3.4}$$

$$F = \int_0^\infty f(u) du \tag{3.5}$$

$f(u)$ is a function of the normalized in-plane wavevector (u) described by Equation 3.6 where $k_{\parallel}$ is the in-plane wavevector and n_e is the emitter refractive index. A simplistic view of this equation for isotropic emitters is given by Equation 3.7 where θ_e and θ are the emission angle of radiation from the emitter and top layer of the OLED stack, respectively. For θ_e between 0° and 90°, u is defined by Equation 3.7, for u > 1, $f(u)$ is radiation at imaginary emission angles and represents waves coupling to evanescent modes.

$$u = \frac{k_{\parallel}}{k_o n_e} \tag{3.6}$$

$$u = \sin\theta_e = \frac{\sin\theta}{n_e} \tag{3.7}$$

The 'Mode Analysis' optical model uses stepwise integration of Equation 3.5 to calculate the power dissipated to the various modes (outcoupled, substrate guided, organic waveguided and evanescent modes) since it is proportional to *F*. The fraction of radiated power is integrated within the refractive index limits as defined

below where n_t and n_e are the refractive index of the top layer and EML, respectively.

1. $0 < u < {}^{n_t}/_{n_e}$ for radiative modes
2. ${}^{n_t}/_{n_e} < u < 1$ for organic waveguided modes
3. $1 < u < \infty$ for evanescent modes

The 'Scattering' function is also enabled with the 'Mode Analysis' and the '3D Ray Tracing' tool to calculate the power distribution to the various modes when an outcoupling structure is included in the OLED architecture. Its development is based on scalar scattering mechanisms[109),110)] and bi-directional scattering distribution functions (BSDF).[111)–113)] The outcoupling structure is sandwiched between two optically incoherent layers (air and substrate) which conform to the shape of the scattering structure (Fig. 3.1); this defines texture to the air side of the

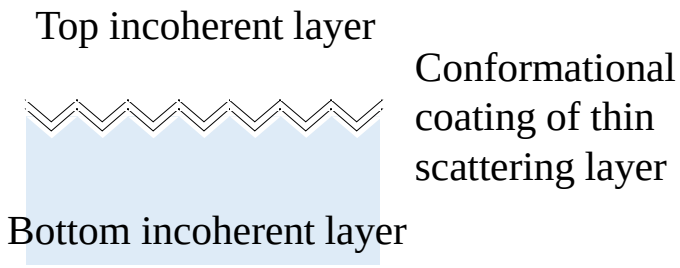

Fig. 3.1 Conformation of the surrounding top (air) and bottom (glass substrate) incoherent layers to the thin scattering layer in SETFOS used in defining the patterned air/substrate interface.

glass substrate. The definition of its shape is imported into SETFOS as an x-y-z texture map after manual design within Microsoft Excel. The ‘z’ values represent the height of the structure at any position defined by the ‘x’ and ‘y’ coordinates.

3.3 Materials

As mentioned in Section 3.1 a simple fluorescent OLED architecture will be utilized. The optical properties of each material must first be defined for the simulation to proceed with power dissipation calculations. The imported n-k dispersion diagrams for the anode, organic layers and ETL are shown in Fig. 3.2. The n-k dispersion diagrams used for the cathode are shown in Fig. 3.3.

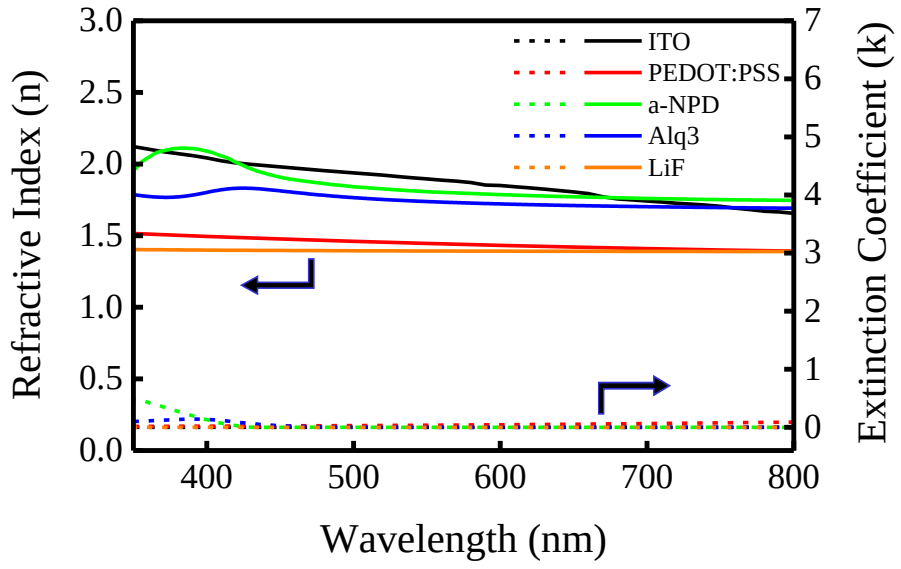

Fig. 3.2 The n-k dispersion for ITO, PEDOT:PSS, α-NPD, Alq_3 and LiF used in the simulation programme.

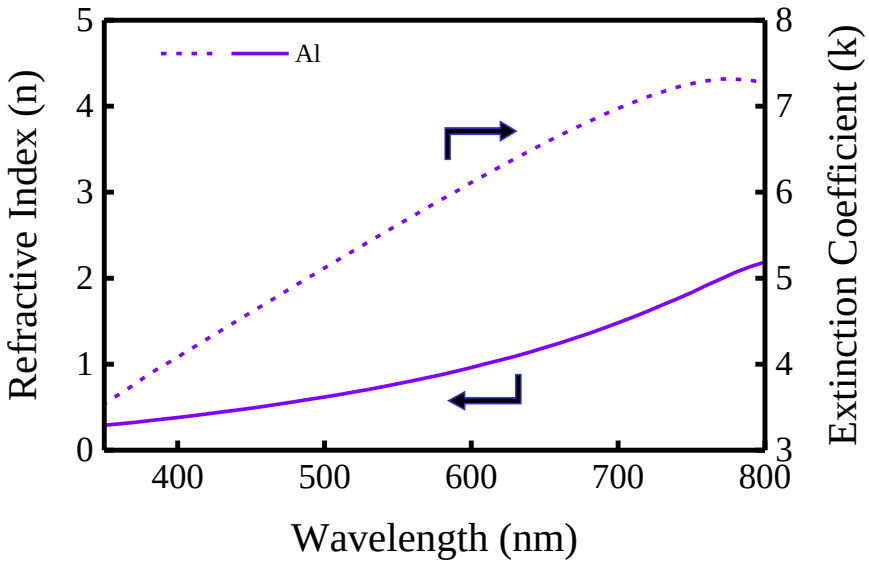

Fig. 3.3 The n-k dispersion for Al cathode used in the simulation programme.

Indium Tin Oxide (ITO)

Pre-coated ITO glass substrates are most popularly used as the conductive anode due to its high work function of about -4.8 eV and high transparency in the visible region.[114)]

Poly(3,4-ethlenedioxythiophene) polystyrene sulfonate (PEDOT:PSS)

PEDOT:PSS has been widely used in OLEDs as either a supplementary anode due to its high conductivity of 10^3 S/cm (after treatment with high dielectric solvents to remove the insulating and excess PSS)[115),116)] and deep work function of -5.2 eV or as the HTL.[117),118)] The inclusion of this layer in the device will be used to represent the OLEDs of low intrinsic transmittance.

N,N'-Bis(naphthalen-1-yl)-N,N'-bis(phenyl)-2,2'-dimethylbenzidine (α-NPD)

α-NPD is popularly used in OLEDs as the HTL material due to its amenability for good hole transport. The energy band of its highest occupied molecular orbital (HOMO) has been reported to be between -5.4 eV and -5.6 eV, while its lowest unoccupied molecular orbital (LUMO) ranges between -2.3 to -2.7 eV.[119)–121)] The deeper HOMO level compared to the work function of ITO and PEDOT:PSS suggests appropriate energy level alignment for hole injection into this layer.

Tris(8-hydroxyquinolinato) aluminium (Alq_3)

Alq_3 functions as both the ETL and EML; as a green, fluorescent emitter, it has the ϕ_{PL} of about 25%. Time-of-flight (TOF) measurements have estimated the electron mobility (μ_e) to be $1x10^{-5}$ cm^2/Vs between the E-fields of $3.9x10^5$ and $1.3x10^6$ V/cm[122)] and the hole (μ_h) mobility on to be around $3x10^{-8}$ cm^2/Vs for an applied E-field of $5x10^5$ V/cm.[123),124)] The HOMO and LUMO of this material are about -5.6 eV and -2.8 eV, respectively,[125)] and thus facilitate the efficient injection and confinement of both holes and electrons for exciton formation.

Lithium fluoride (LiF)

Lithium fluoride is an insulating material that serves as an interfacial electron injection layer between the EML and cathode. After the deposition of the aluminium cathode over LiF, Li atoms and AlF_3 compounds are produced. Li atom

dissociation donates electrons to Alq_3 to form Alq_3 anions which reduce the electron injection barrier, and a good contact is formed with the cathode.[126),127)]

Aluminium (Al)

Al has a work function of about -4.2 eV[128)–131)] and has > 90% reflectivity in the visible region.It is therefore most suitable as the cathode in the OLED structure.

3.4 Simulated optimization of glass patterns

The simulated structure of the OLED devices to be used throughout this study are summarized in Fig. 3.4 Devices A and B are OLEDs have high transmittance while Devices C and D include a relatively thick 85 nm PEDOT:PSS layer and thus have intrinsically low transmittance. Devices A and C with non-patterned substrates serve as the reference devices for patterned substrate devices B and D, respectively.

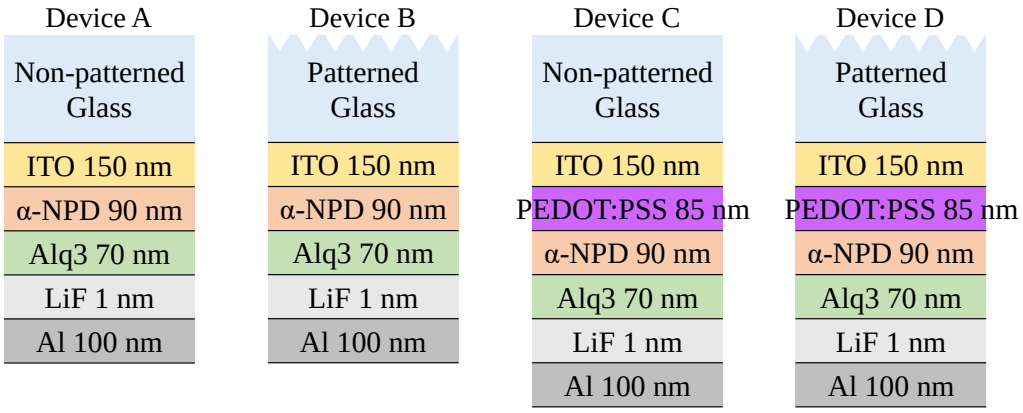

Fig. 3.4 Cross-sectional OLED device structures used in SETFOS simulation.

The patterns to be evaluated are designated ‘glass patterns’ made at the air/glass substrate interface of the OLED. The optimization of the glass patterns’ dimensions for maximum η_{out} will be evaluated using the η_{out} enhancement ($\Delta\eta_{out}$) given by Equation 3.8. The η_{out_patt} and $\eta_{out\_nonpatt}$ is the fraction of outcoupled modes in the devices with patterned and non-patterned substrates, respectively. Thus, only the structures of Devices A and B from Fig. 3.4 are used for the optimization process.

$$\Delta\eta_{out} = \frac{\eta_{out\_patt} - \eta_{out\_nonpatt}}{\eta_{out\_nonpatt}} \times 100\% \qquad (3.8)$$

The parameters used to define the dimensions of the glass hole patterns arranged in a square-like lattice include the depth, diameter, edge-to-edge distance (EE distance) and shape. They are illustrated by Fig. 3.5 and Fig. 3.6.

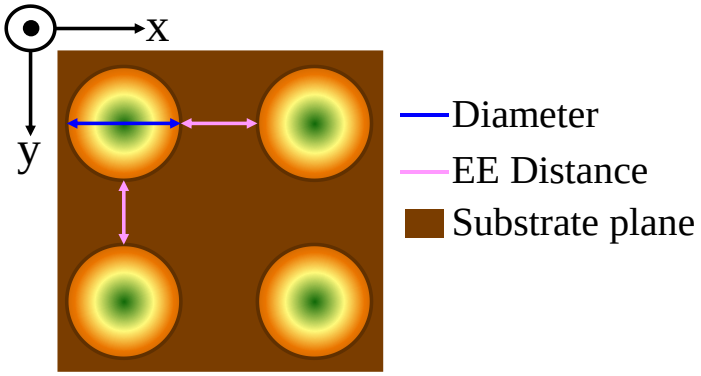

Fig. 3.5 Schematic of hole patterns made on the glass substrate arranged in a square packing lattice. Hole diameter and EE distance (lateral hole edge distances) are represented by the blue and pink arrows, respectively.

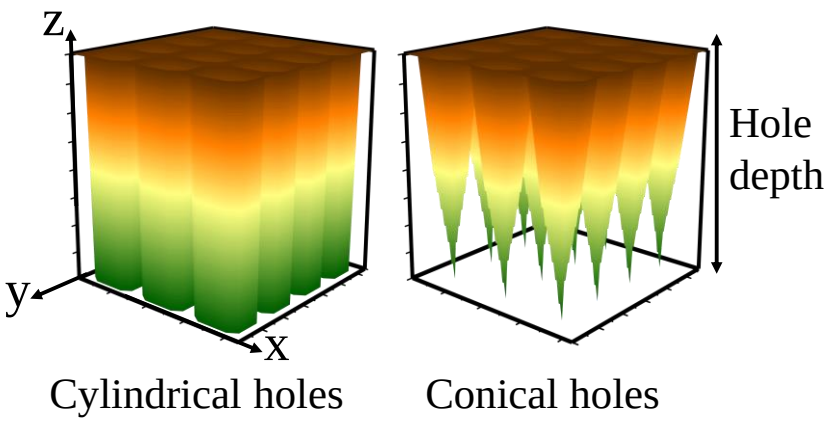

Fig. 3.6 3D representation of cylindrical and conically shaped glass substrate hole patterns. The depth is defined as the distance from the planar surface of the glass substrate to the lowest point of the pattern's feature.

The optimization of the pattern dimensions will proceed in a systematic fashion. First, one parameter (x) is varied while the others are kept constant. The best dimensions of parameter x that yields maximum η_{out} and $\Delta\eta_{out}$ is carried forward to the next optimization step. The second step involves varying another parameter (y) while keeping all other parameters (including optimized x) constant. This process is repeated until all parameters have been optimized to yield the maximum possible η_{out} and $\Delta\eta_{out}$ within the specified range of dimensions that were investigated. The results of the simulation will be presented followed by a discussion.

Optimization of glass hole patterns EE distance

Table 3.1 shows the conditions for simulated optimization of the EE distance for glass patterns using the structure of Device B (Fig. 3.4) and the results are shown in Fig. 3.7. The depth and diameter were chosen randomly for the sake of optimizing the EE distance. A maximum η_{out} ($\Delta\eta_{out}$) of about 24.0% (20.1%) was achieved with an EE distance of 1 μm and is consistent for varying dimensions of depth, diameter and shape; this dimension will be carried forward to the next step.

Table 3.1 Summary of hole pattern dimensions for the optimization of EE distance only.

Parameter	Dimension
EE Distance	Varied
Shape	Cylindrical
Depth	4 μm
Diameter	6 μm

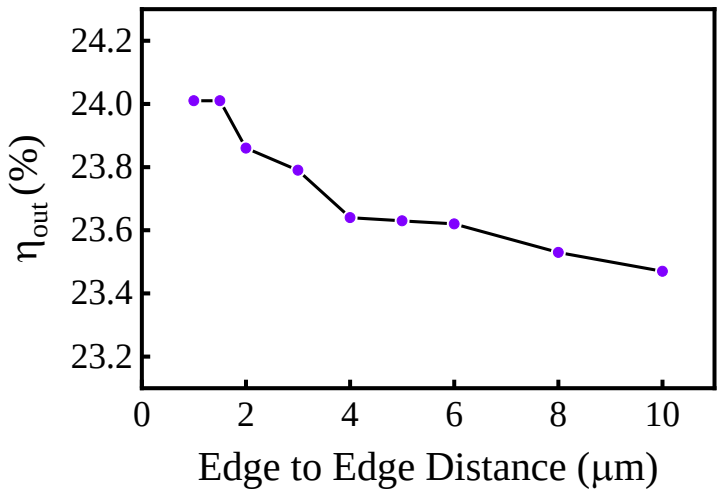

Fig. 3.7 Effect of increasing the EE distance of glass patterns on the η_{out}.

Optimization of glass hole pattern shape

Table 3.2 shows the conditions for optimizing the hole shape of the glass patterns using an optimized EE distance of 1 μm and Fig. 3.8 shows the results of $\Delta\eta_{out}$. Based on the assigned dimensions, conically shaped holes give the better η_{out} ($\Delta\eta_{out}$) of 26.1% (30.4%) and this shape will be used in the next optimization step.

Table 3.2 Summary of hole pattern dimensions for the optimization of glass hole pattern shape only.

Parameter	Dimension
EE Distance	1 μm
Shape	Varied
Depth	4 μm
Diameter	6 μm

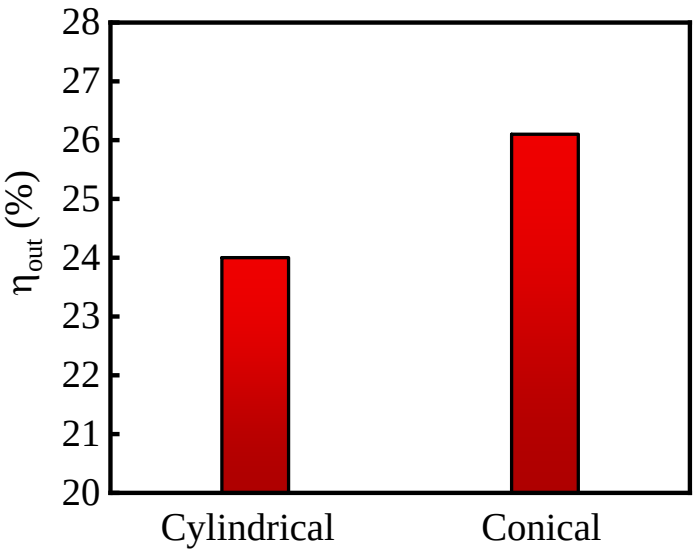

Fig. 3.8 Effect of hole shape on the η_{out} for glass hole patterns with optimized 1 μm EE distance.

Optimization of glass hole pattern diameter and depth

Table 3.3 shows the conditions for optimizing the diameter and depth of glass patterns using the optimized EE distance of 1 μm and conical hole shape. Fig. 3.9 shows the results for the effect of diameter and depth on the η_{out}. A maximal range for η_{out} is found to exist for diameter 4 – 7 μm having depth 3 – 11 μm.

Table 3.3 Summary of hole pattern dimensions for the optimization of diameter and depth of cylindrically shaped holes.

Parameter	Dimension
EE Distance	1 μm
Shape	Conical
Depth	Varied
Diameter	Varied

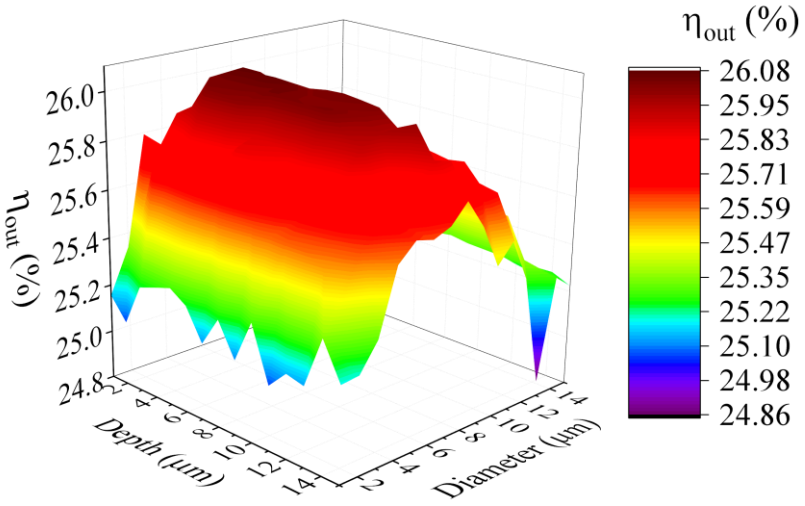

Fig. 3.9 Depth vs. diameter on the η_{out} for conically shaped glass patterns.

Discussion of optimization results

The simulation results presented above clearly demonstrate that OLED devices with patterned glass substrates exhibit enhanced η_{out} over non-patterned glass substrate devices. This result is attributed to the extraction of substrate guided modes into the forward viewing region of the device. Where the refractive index mismatch between the glass (n = 1.5) and air (n = 1) normally induce a θ_c cone in a planar reference substrate, light rays incident on the air/substrate interface at fairly large angles ($\theta_i > \theta_c$) will experience total internal reflection (TIR). The patterned surface discounts this condition via geometrical tilting of a new surface normal. This allows rays at large angles relative to the x-y plane to meet the patterned air/substrate interface at an angle $\theta_i < \theta_c$ and be extracted as outcoupled modes.

Fig. 3.7 illustrates that for glass patterns with a depth of 4 μm, diameter of 6 μm and cylindrical shape, the η_{out} increases as the EE distance decreases. The EE distance is directly proportional to the hole packing density (ρ_{pack}) and therefore defines the number of holes that will occupy a set area over the substrate. An increase in the ρ_{pack} increases the probability and number of rays that will meet the patterned surface and be outcoupled into free space. For example, Fig. 3.10 illustrates that for an arbitrary area over the substrate, 1 μm EE distance between the holes will allow 2x the ρ_{pack} of those with 5 μm EE distance. Thus, a greater η_{out}

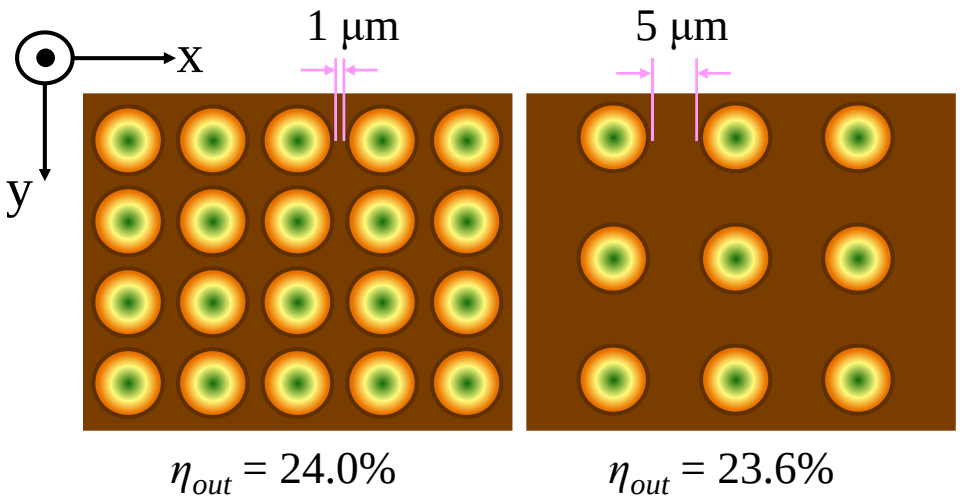

Fig. 3.10 Schematic illustration of how ρ_{pack} of holes is influenced by EE distance.

($\Delta\eta_{out}$) of 24.0% (20.1%) is realized from the 1 μm EE distance patterns compared to the 23.6% (17.8%) from 5 μm EE distance patterns.

Fig. 3.8 shows that for hole patterns with optimized EE distance of 1 μm, the η_{out} ($\Delta\eta_{out}$) can be enhanced to 26.1% (30.36%) by using conically shaped holes over cylindrical ones. The geometry of both the cylindrically and conically shaped holes indeed shifts the surface normal to accommodate for rays impinging on the surface at large θ_i to be outcoupled into the forward viewing direction. Fig. 3.11 illustrates a schematic example of an incident ray with $\theta_i > \theta_c$ relative to a flat reference substrate and its most likely outcoupling or TIR events after contacting either conically or cylindrically shaped holes. The consistent angular surface of the

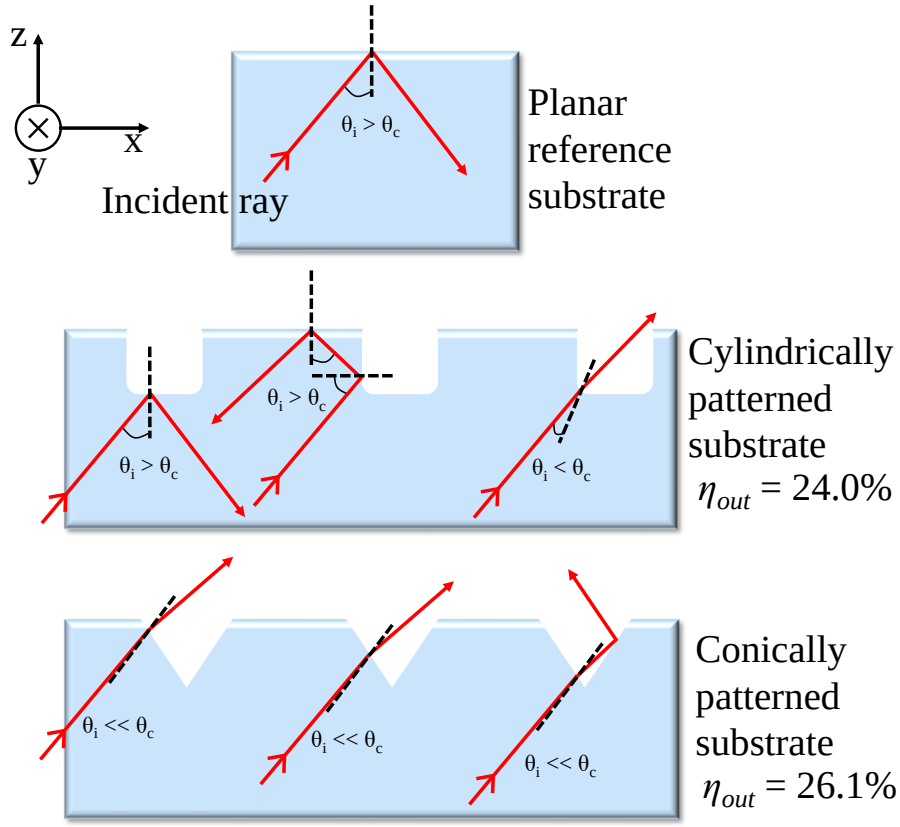

Fig. 3.11 Cross-sectional representation of TIR and outcoupling events for a light ray with $\theta_i > \theta_c$ critical angle for planar reference, conically and cylindrically patterned air/glass interfaces.

conically shaped patterns increase the probability of rays meeting any point along the surface at an angle much smaller than θ_c. These rays are likely to be extracted into the forward viewing free space of the OLED and demonstrates higher η_{out}. Various orientations of the surface normal exist along different points of the cylindrically shaped holes, thus the probability of rays with $\theta_i > \theta_c$ being outcoupled

into free space is dependent on their incident position. Rays impinging on the flat base of the cylindrical hole surface are likely to experience TIR and remain trapped within the substrate or escape as edge emission. Rays that are incident on the side of the cylinder are likely to experience multiple reflection events due to large θ_i made with the surface normal. The most ideal incident position for light rays incident at the angle specified in Fig. 3.11 for outcoupling into free space would be at the corner of the cylindrical pattern.

Fig. 3.9 illustrates a contour plot of changes in the η_{out} with simultaneous variation between the depth and diameter for hole patterns with optimized 1 μm EE distance and conical shape. The results show that the η_{out} is more sensitive to changes in the diameter than it is to the depth of conical holes. This may be attributed to changes to the tapering (base) angle of the hole patterns that is estimated from the isosceles triangle base equation (α). It is reasonable to appreciate that α affects the orientation of the new surface normal created at the slanted interface of the conical pattern and therefore the outcoupling probability of incident light rays with $\theta_i > \theta_c$ (relative to a non-patterned substrate). The change of α with varying depth and diameter of conically shaped holes is illustrated in Fig. 3.12. When the diameter of the conically shaped hole changes between 3 - 7 μm while

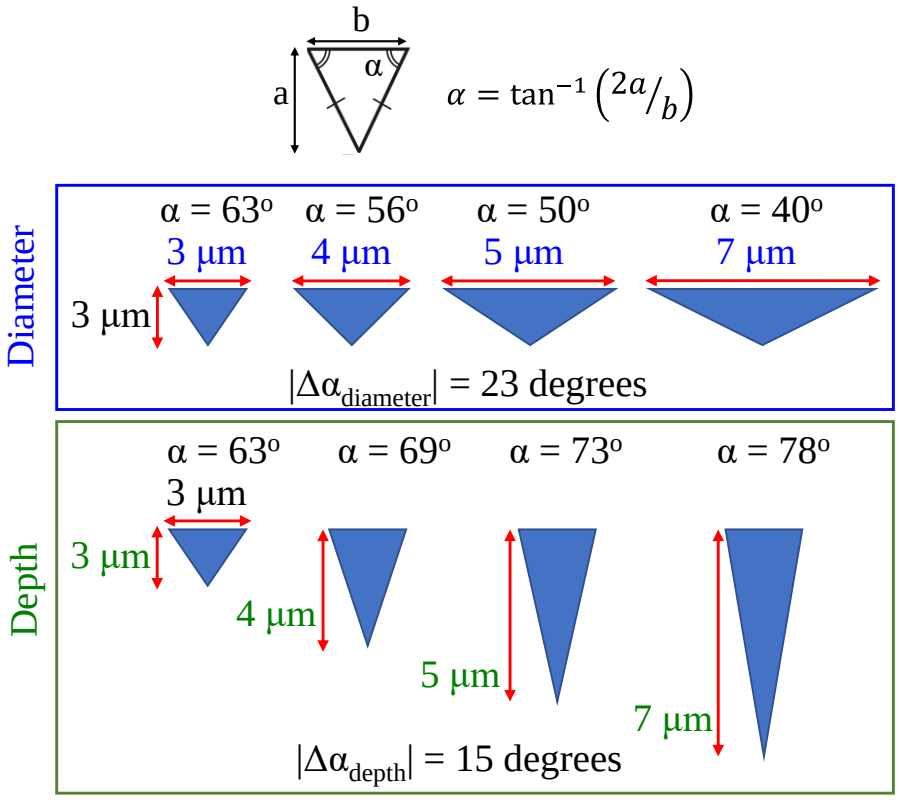

Fig. 3.12 Schematic illustration of how the tapering base angle of conically shaped holes changes of with increasing diameter and depth.

the depth is kept constant at 3 µm, α varies by 23°. When the depth changes between 3 - 7 µm while the diameter is kept constant at 3 µm, α varies by only 15°. The change in η_{out} with increasing diameter is, however, not proportional to the change in α. This suggests that the interplay between ρ_{pack} and diameter are necessary for high η_{out}. The optimal range of η_{out} for which there is an appropriate orientation of the conical hole's new surface normal is found for a depth and diameter of 3 - 11 µm and 4 - 7 µm, respectively.

3.5 Experimental verification of simulated results

3.5.1 Device fabrication

Prior to fabrication of the OLED device, pre-patterned 150 nm ITO glass substrates were first patterned on the air/glass substrate interface using the femtosecond laser developed by IMRA America Inc. The air/glass interface side of a reference substrate was exposed to an ytterbium doped fiber laser (FCPA μJewel DX-0540) having a center wavelength of 1045 nm, pulse duration of 450 fs and a maximum average power of 5W. The patterning process (Fig. 3.13) of conically shaped glass hole patterns with a depth, diameter and EE distance of 10 μm, 5.5 μm and 1 μm were successfully completed. These dimensions were chosen based on the realistic fabrication constraints of the femtosecond laser for a combination of depth and diameter within the cone of maximum η_{out} (Fig. 3.9).

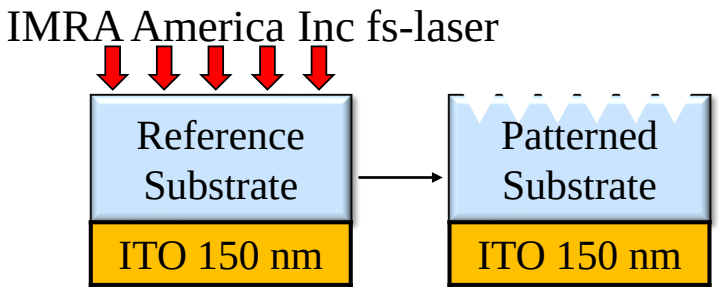

Fig. 3.13 Single step process of patterning the air/glass interface of OLED substrates.

After the air/glass patterning of ITO substrates were completed, the substrates were moved to a clean room for cleaning and fabrication preparation. The two sets of substrates that were prepared include non-patterned and air/glass side patterned ITO substrates. All substrates were ultrasonicated in sequential baths of acetone, semicoclean, pure water and finally isopropyl alcohol. To increase the work function of ITO and remove excess organic contaminants, all substrates were placed in a closed chamber for UV-Ozone irradiation treatment for 30 minutes.[132)–134)]

The OLED devices were then fabricated with the same internal architecture as those illustrated in Fig. 3.4 by depositing the subsequent organic layers over the 150 nm ITO. An 85 nm thick PEDOT:PSS layer was first deposited over the ITO side of a reference and patterned substrate by spin coating at a speed of 1500 RPM for 30 seconds followed by being placed over a 100 ^{o}C hot plate for 10 minutes to remove the excess solvent. The non-patterned substrates excluding and including PEDOT:PSS are used to make devices A and C, respectively. The patterned substrates excluding and including PEDOT:PSS are used to make devices B and C, respectively. Over the 150 nm ITO (A and B) or 85 nm PEDOT:PSS (C and D) the following organic layers were sequentially deposited in an ultra-high vacuum evaporator with a base pressure of 10^{-8} Torr: 90 nm thick layer of α-NPD followed by 70 nm thick layer of Alq_3 at a deposition rate of 0.1 nm/s, 1 nm thick layer of LiF at a deposition rate of 0.01 nm/s and a 100 nm thick layer of Al at a deposition

rate of 0.2 nm/s. Following the device fabrication, all devices were moved to a nitrogen (N_2) filled glovebox via a small vacuum shuttle chamber, wherein they were encapsulated using a glass cover with attached thin desiccant film and UV-cured epoxy seal. This process was done so all devices may be evaluated in air void of oxygen/moisture degradation effects.[135),136)]

3.5.2 Device characterization

The top images of the air/glass patterned substrates were collected using a 3D laser scanning confocal microscope (VK-9700 Keyence) while the cross-sectional images were collected using a desk-top scanning electron microscope (Hitachi SEM TM3030 plus). The current-density-voltage (*J-V-L*) characteristics of the OLED devices were measured using a source-meter (Keithley 2400) and luminance meter (Topcon BM-910D, 1^o solid measurement angle) with an attachment lens (AL-8). The EL spectra were measured using a spectrophotometer (PMA-11 Hamamatsu Photonics) and the η_{ext} was measured using an integrating sphere equipped with a silicon photodiode detector. The $\Delta\eta_{out}$ is derived from the η_{ext} measurements and calculated in a similar manner to Equation 3.8. The luminance enhancement (ΔL) is also calculated according to the luminance of the reference and patterned using Equation 3.8. The viewing angle dependence measurements were performed by mounting the OLED device on a rotation stage wherein the EL spectra were collected using an Ocean Optics USB4000 spectrometer. The view finder of a

luminance meter (Topcon BM-902 with 0.2^{o} solid angle measurement) was used to focus the fibre optic detector on the centre of the OLED's active area. Fig. 3.14 shows a schematic setup for the viewing angle dependent measurements.

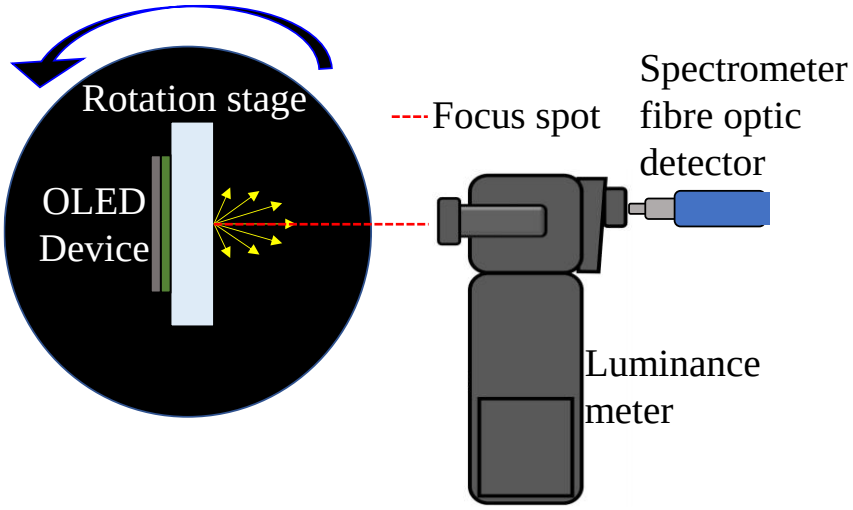

Fig. 3.14 Top view schematic diagram of EL spectra - viewing angle dependent measurements.

3.5.3 Results and discussion

The dimensions of the air/glass patterns were first confirmed via microscopy. The SEM and laser microscope images in Fig. 3.15 confirm the successful patterning of the air/glass interface of ITO substrates. The patterns are confirmed to be conical in shape with a depth of ~ 10 μm, diameter ~5.5 μm and EE distance ~1 μm. These dimensions are well within the cone of maximum η_{out} based on simulated calculations (Fig. 3.9) and their results are suitable for comparison to experimental results. The electrical and optical performance characteristics of all devices are summarized in Fig. 3.16 and are separated between devices of similar internal structure.

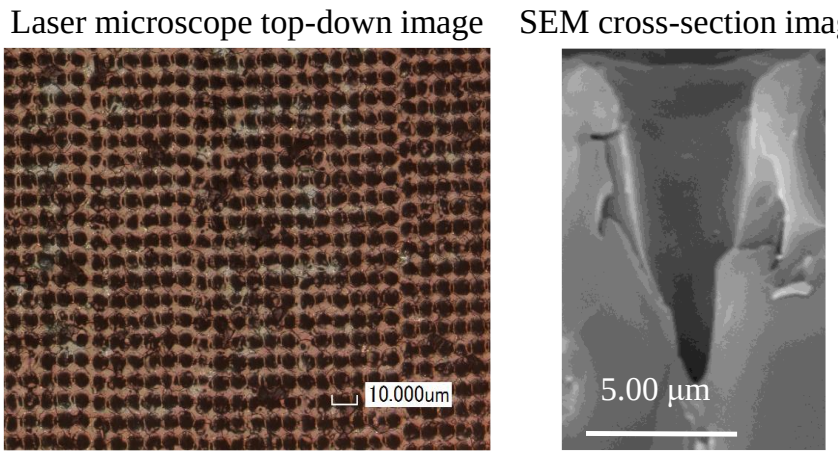

Fig. 3.15 Top-down and cross-sectional images of air/glass substrate patterns fabricated via one-step femtosecond laser (IMRA America Inc.) with optimized dimensions for maximum η_{out}.

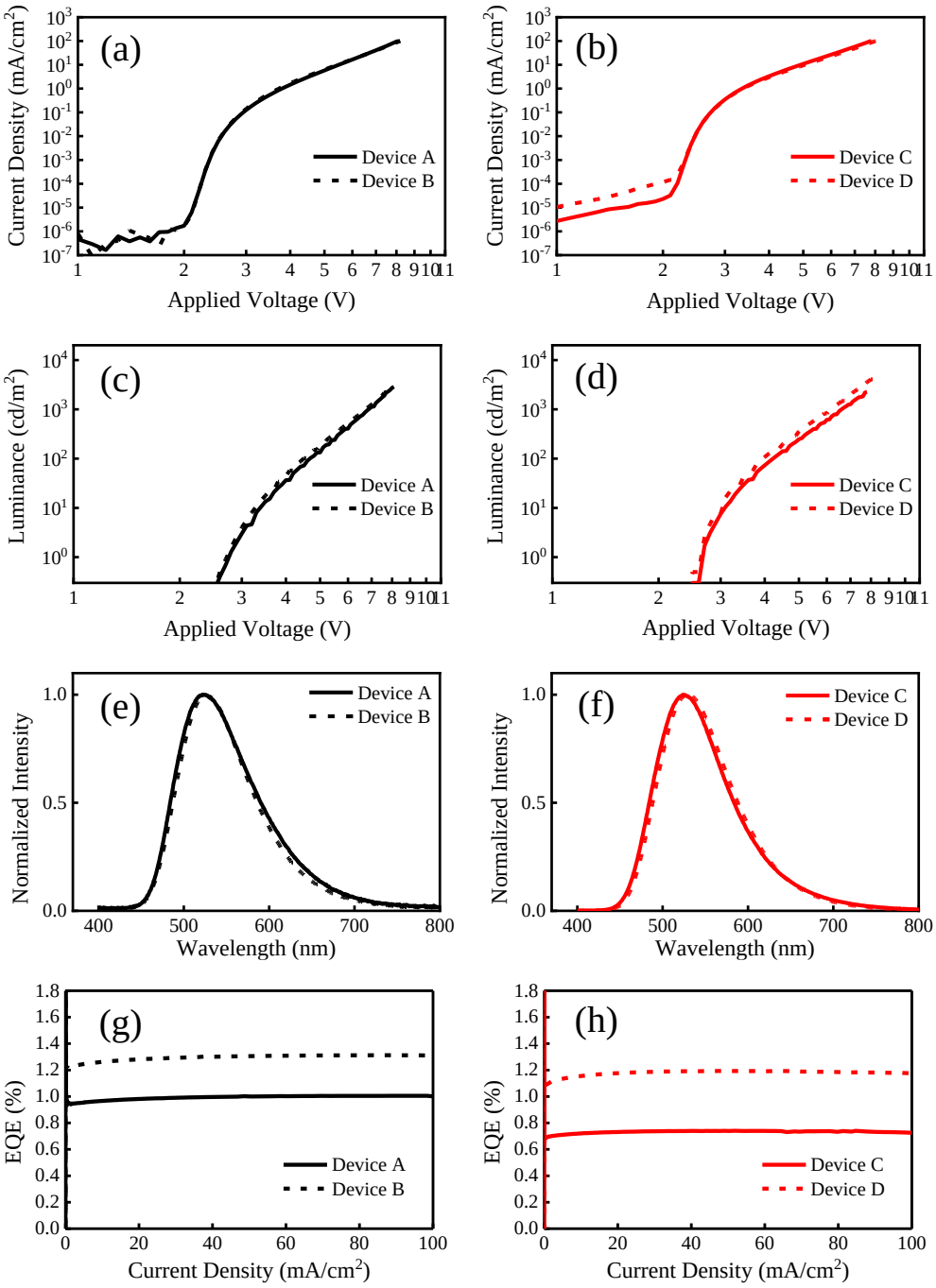

Fig. 3.16 (a, b) Current density-voltage, (c, d) luminance-voltage and (e, f) EL spectra and (g, h) EQE of reference and patterned OLED devices.

The *J-V*, *L-V*, EL spectra and EQE characteristics of devices A and B (without PEDOT:PSS) are shown in Fig. 3.16 (a), Fig. 3.16 (c), Fig. 3.16 (e) and Fig. 3.16 (g), respectively. The *J-V*, *L-V*, EL spectra and EQE characteristics of devices A and B (including PEDOT:PSS) are shown in Fig. 3.16 (b), Fig. 3.16 (d), Fig. 3.16 (f) and Fig. 3.16 (h), respectively. The operational *J-V* and EL spectra characteristics in both sets of devices, with and without PEDOT:PSS, exhibit excellent overlap between the non-patterned and patterned glass substrate devices. This indicates that the air/glass patterns have no effect on the either charge injection characteristics or emission mechanism within the OLED device. Since both sets of devices utilize the same emitter and internal structure below the anode, it is logical to infer that the η_{int} between the non-patterned and its respective patterned device are the same. Any changes in the light extraction characteristics (luminance and η_{ext}) are a direct consequence of changes in η_{out} and therefore η_{ext} measurements are an appropriate representation for such changes (Equation 2.1). Thus, the simulated η_{out} from Section 3.4 are comparable to the measured η_{ext} discussed in this section.

Table 3.4 summarizes the measured luminance and η_{ext} and calculated $\Delta\eta_{ext}$ and ΔL for all devices under similar driving voltage and current densities. $\Delta\eta_{ext}$ and ΔL were calculated in a similar manner to Equation 3.8. To confirm the reproducibility of these results the average values shown in the table were calculated from two sets of each device used in this study. For non-patterned and

patterned devices without PEDOT:PSS, the η_{ext} for device A is 0.98% while its patterned equivalent device B exhibits a superior η_{ext} of 1.28% at an operational current density of 50 mA/cm^2. The calculated $\Delta\eta_{ext}$ of 30.5% is therefore a result of extracted substrate guided modes due to patterning at the air/glass interface and corresponds well to the simulated results (as discussed in Section 3.4). Similar results are observed for non-pattered and patterned devices including PEDOT:PSS where device C and D exhibited η_{ext} of 0.73% and 1.17%, respectively. This corresponded to $\Delta\eta_{ext}$ of 60.6% due to the patterned device.

Glass hole patterns made at the air/glass interface can efficiently extract a portion of the substrate guided modes regardless of the internal device structure. The η_{ext} values represented in this study are typically lower than devices that utilize more complex heterojunction structures to support superior charge transport (and blocking) and highly efficient emitters. The simple Alq_3 OLED device employed in this study is used as a proof-of-concept to demonstrate the air/glass pattern's

Table 3.4 Summary of optical characteristics for all devices under similar driving voltage and current density characteristics.

Device	***V*** **(V)**	***J*** **(mA/cm^2)**	***L*** **(cd/m^2)**	***ΔL*** **(%)**	η_{ext} **(%)**	$\Delta\eta_{ext}$ **(%)**
A	7.3	50.5	1358	-	0.98	-
B	7.4	50.8	1669	23.0	1.28	30.5
C	7.3	51.0	1135	-	0.73	-
D	7.5	50.6	1934	70.5	1.17	60.6

ability to enhance the η_{ext} (and by extension, the η_{out}). Similar results of $\Delta\eta_{ext}$ are expected in devices with similar refractive index/optical architecture. Indeed, the enhancements in η_{ext} are due purely to substrate guided modes being redirected into the forward viewing direction. Since the patterning is made on the 'outside' of the device at the air/glass interface, only substrate guided modes are affected. Organic waveguided modes and surface plasmons are confined to the 'inside' of the device at the substrate/organic and organic/metal interfaces, respectively, and therefore the air/glass patterns cannot redirect nor extract these modes.

Comparison between the reference OLEDs show that device C exhibits inferior η_{ext} (and luminance) of 0.73% (1135 cd/m^2) compared to the 0.98% (1358 cd/m^2) observed in device A. This is expected and is a consequence of the thick 85 nm PEDOT:PSS layer used in device C which lowers the intrinsic transmittance of the substrate. A generous fraction of light generated within the emissive layer is expected to be absorbed by the substrate before being outcoupled into free space. Contrary to this trend is the comparison between the patterned devices. The PEDOT:PSS inclusive device D exhibits an inferior η_{ext} of 1.17% compared to 1.28% in device B without PEDOT:PSS, while device D exhibits a superior luminance of 1934 cd/m^2 compared to 1669 cd/m2 in device B. This phenomenon may be explained in the differences between the measurement techniques used to

collect luminance and η_{ext} and the distribution of light in patterned devices with and without PEDOT:PSS.

During the luminance measurement, the luminance meter is positioned directly above the OLED and collects light propagating along the normal viewing direction ($\theta = 0^o$ only). During the measurement of η_{ext}, the integrating sphere collects light emitted over all angles in the forward viewing direction of the device ($-89^o \leq \theta \leq 89^o$). These points are illustrated by Fig. 3.17 which show the difference in measurement setups between η_{ext} and luminance. To compliment this argument, the EL spectra intensity as a function of viewing angle was collected for all devices and shown in Fig. 3.19. A close look at the viewing angle EL spectra distribution for the patterned devices shows that device D has a greater spectral distribution in narrow viewing angles (between 0^o and 30^o) compared to device B that has greater spectral distribution at wider viewing angles (between 30^o and 80^o). Thus, a higher

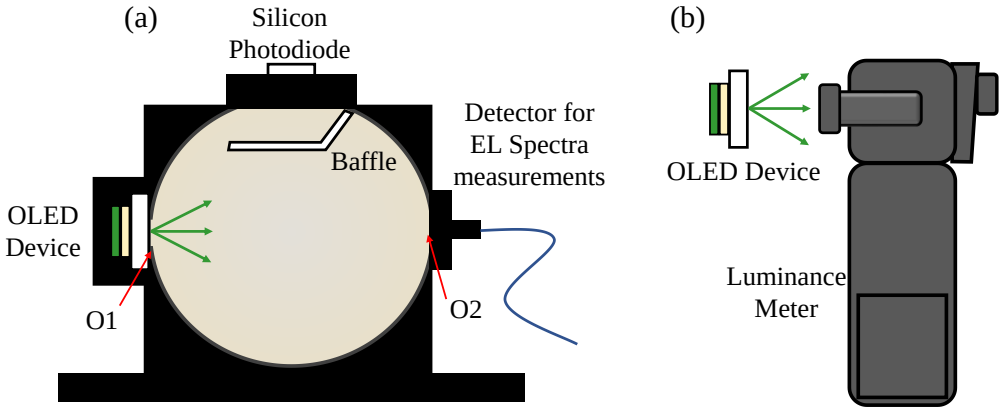

Fig. 3.17 Measurement setup for (a) η_{ext} and (b) luminance.

luminance would be detected for device D since its spectral distribution is strongest in the direction of measurement. The true description of light extraction efficiency, however, is represented by η_{ext} since light from all directions are collected. This also explains why the $\Delta\eta_{ext}$ and ΔL because of the patterned interface for each set of devices are not equal (where the ΔL is less than the $\Delta\eta_{ext}$). The results in Fig. 3.19 also confirm the mechanism for light extraction in patterned devices. Both patterned OLEDs (devices B and D) demonstrate higher spectral distribution in wider viewing angles compared to their respective reference OLEDs (A and C) confirming that the scattering mechanism redistributes substrate guided modes to outcoupled modes.

Fig. 3.18 shows the simulated contribution of modes in all devices after 100% of light is generated in the EML. The fraction of outcoupled modes (η_{out}) agree well with the experimental data presented in Table 3.4. The patterns at the air/glass interface do not excite SPs, shift the emission zone nor affect the Alq_3 TDM orientation, therefore the evanescent mode contributions remain unaffected in all devices. The increased fraction of absorbed modes in device C (8%) compared to device A (2%) confirms the lower intrinsic transmission through the non-patterned OLED substrates that include a thick layer of PEDOT:PSS. Device C also exhibits higher organic waveguided modes (17%) than device A (11%) due to the refractive index mismatch between PEDOT:PSS and ITO (according to Fig. 3.2 the $n_{PEDOT:PSS}$ ~1.5 < n_{ITO} ~1.9 at 520 nm).[137] Light entering the ITO layer will be subjected to a

cone of critical angle limitation and thus increases the fraction of rays guided within the organic layers.

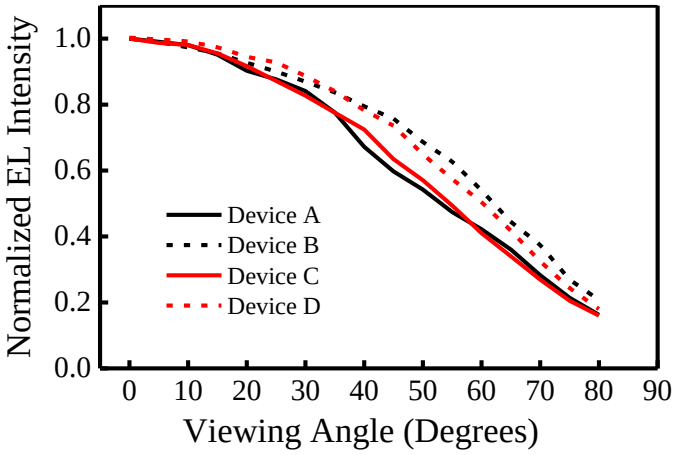

Fig. 3.19 Normalized EL intensity viewing angle distribution of all devices.

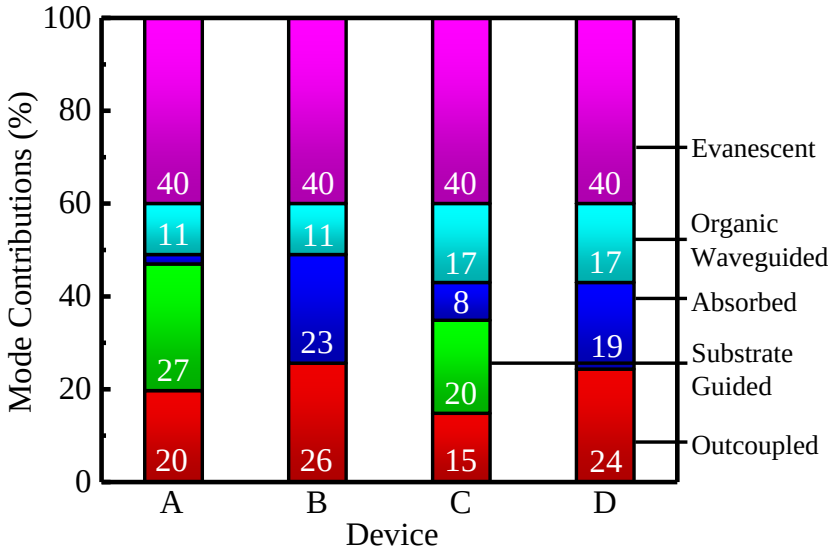

Fig. 3.18 Simulated contribution to all modes after 100% light generation in the in the emissive layer for all OLEDs used in this study (correct to 2 signification figures).

In device B a portion of light rays propagating within the substrate will be subjected to multiple reflection events between the patterned air/glass interface and the glass/organic interface [138),139)] while the portion that remains trapped within the substrate or propagates through organic layers is counted towards 'absorbed' contribution. This explains the increase in absorbed modes in device B (23%) compared to device A (2%). The backscattered rays in device D have a higher probability of experiencing TIR when incident on the PEDOT:PSS/organic interface since $n_{PEDOT:PSS}$ ~1.5 < $n_{organic}$ ~1.8 - 1.9 at 520 nm. Upon re-entry into the substrate at smaller angles, they will have an additional opportunity to be coupled into free space after impinging on the patterned air/glass interface. The re-entry of back scattered rays into the substrate reduces their likelihood of being trapped within the substrate or organic layers and accounts for the lower contribution of absorbed modes (19%) compared to device B (23%). This accounts for the higher $\Delta\eta_{out}$ of 60.6% observed in device D (relative to the non-patterned device B) over $\Delta\eta_{out}$ in device B of 30.5% (relative to the non-patterned device A).[8)]

Since the dimensions patterns (μm-scale) are much larger than the wavelength of emitted light (nm-scale), the geometrical ray optic treatment is appropriate for explaining the mechanisms behind the enhancement of η_{out}. Additionally, it is expected that similar results can be achieved for OLEDs of different colours due to this emitted wavelength independence.

3.6 Viewing angle dependence

The viewing angle dependence in all the OLED devices used within this study are shown in Fig. 3.20. Common between both sets of non-patterned OLED devices (A and C) is the shifting of the EL spectra peak by 11 – 12 nm as the viewing angle increases from the normal (0^o) to large viewing angle directions (80^o). Both sets of patterned devices (B and D), however, exhibit a reduction in the spectral shifting to only 4 - 5 nm. The randomization of the light path due to scattering at the air/glass interface (confirmed in Fig. 3.19) is effective for disarraying the interference effects that lead to colour shifting in the first place. The small EE distance of 1 μm between the holes and high ρ_{pack} factor contribute to the high scattering power experienced in these devices. The reduction of the viewing angle dependence by the air/glass substrate hole patterns used in this study are also expected to be

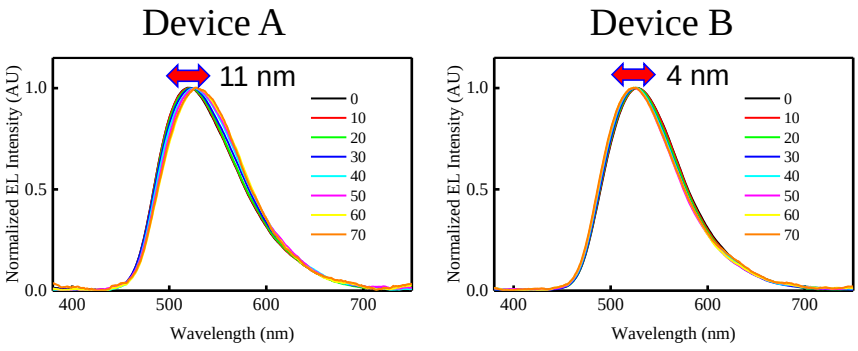

Fig. 3.20 Normalized viewing angle dependence of EL spectra for all devices used in this study.

applicable to devices that exhibit stronger microcavity effects, for example in top emission OLEDs where up to 19 nm in colour shifting is possible.[6)] The weak microcavity device employed here functions as a proof-of-concept to demonstrate the effect of scattering power on the EL spectral dependence.

To visually illustrate the effect of colour shifting in OLEDs, the chromaticity coordinates of the EL spectra plotted over the 1931 CIE (x, y) coordinate diagram using the 'Chromaticity Diagram' tool in OriginPro 2022 (9.9.0.225). The CIE diagram (Fig. 3.21 (a)) is a mathematically mapped colour space bound by the pure red-green-blue (RGB) monochromatic wavelengths and is used to quantify the colours perceived by the human eye. The EL spectra taken at varying viewing angles from the non-patterned and patterned devices cover the general region indicated by the black box. Fig. 3.21 (b) and Fig. 3.21 (c) show a 'zoomed-in-view' of the chromaticity feature for non-patterned and patterned devices, respectively where each plotted point represents the EL spectra at a specific viewing angle. Fig. 3.21 (b) shows that the colour from the non-patterned device covers a wider range of the CIE coordinate diagram as the viewing angle changes from 0^{o} to 80^{o} compared to the patterned device in Fig. 3.21 (c). This visual representation shows

the reduction of viewing angle dependence and colour shifting in OLEDs via patterning at the air/glass interface.

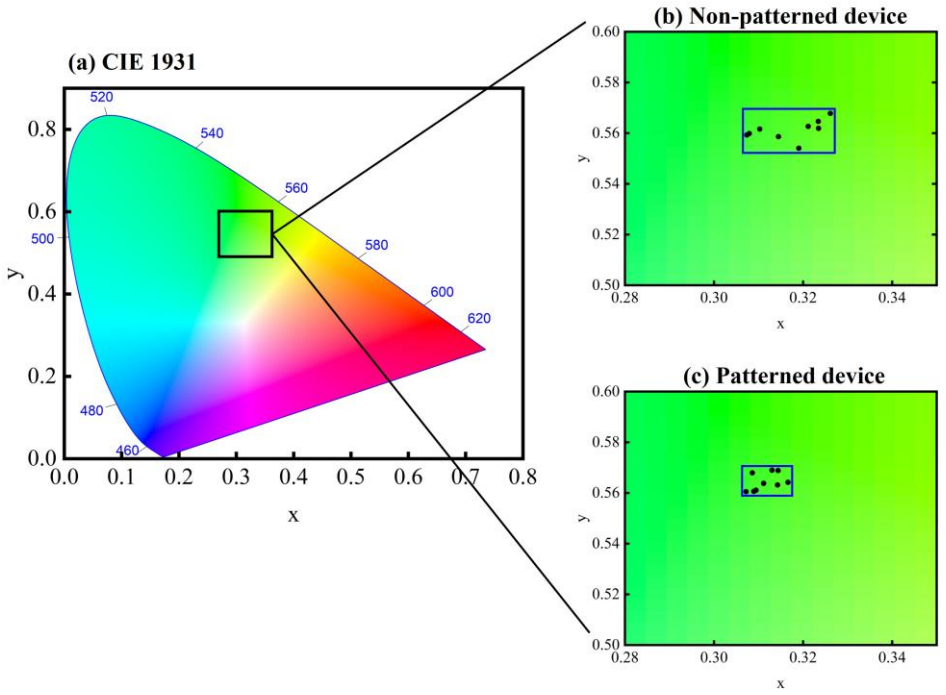

Fig. 3.21 (a) Plot of the CIE 1931 colour space (black box outlines probing area) and zoomed in plots of the emitted colour distribution from (b) non-patterned and (c) patterned devices based on the EL spectra (converted to *x*-*y* coordinates) taken between 0^{o} and 80^{o} viewing angle.

3.7 Conclusion

This work overcomes the limitations experienced by past research when attempting to improve the η_{out} in OLED devices. The fabrication of outcoupling structures may be tedious and complex and, in some cases, induces stronger viewing angle dependence of the EL spectra than in the planar reference OLED. This work demonstrates that by using an Yb-doped femtosecond laser (IMRA America Inc.) the complexity of fabrication is reduced to a single-step method. Inscribing a high density of conical holes at the air/glass interface allows the realization of simultaneous enhancement in the η_{out} and reduction of viewing angle dependence due to extraction of substrate guided modes and high scattering at the air/glass interface, respectively. For OLEDs with a high intrinsic transmittance, the η_{out} can be enhanced from 20% to 26% and demonstrates a 30.5% enhancement. For OLEDs with a low intrinsic transmittance, the η_{out} can be enhanced from 15% to 24% and demonstrates a 60.6% enhancement.

3.8 Outlook

The future of utilizing scattering structures at the air/glass interface of OLED substrates can be enhanced further by marrying nm- and μm-scale structures. A popular and well researched example involves the manmade replication of bio-inspired moth-eye nanostructures where nm-scale dome-like patterns are arranged in μm-scale hemispherical structures. They have shown excellent applications for organic opto-electronic device applications; enhancing light outcoupling in OLEDs, enhancing light harvesting in organic solar cells (OSCs)[140] and as antireflection/antifogging structures for both OLED and OSC devices.[141]

We have recently applied this concept to the air/glass substrate hole patterns discussed in the previous section, where nm-sized surface roughness is applied to the planar areas between the μm-sized hole patterns. The samples made are meant to be representative proof-of-concept and thus consist of unoptimized (relative to the optimized parameters discussed in previous sections) air/glass holes with arbitrary dimensions. The holes' pitch (EE distance + diameter) of either 2 - 3 μm, >10 μm depth, hexagonal packing type and cylindrical shape were chosen based on the capability of the manufacturer to realistically fabricate both μm- and nm-sized patterns.

Cylindrical patterns with smooth surface [Pitch = 3 μm, hexagonal lattice packing]

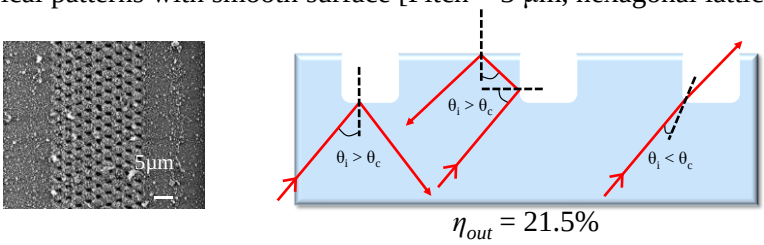

Cylindrical patterns with rough surface [Pitch = 2 μm, hexagonal lattice packing]

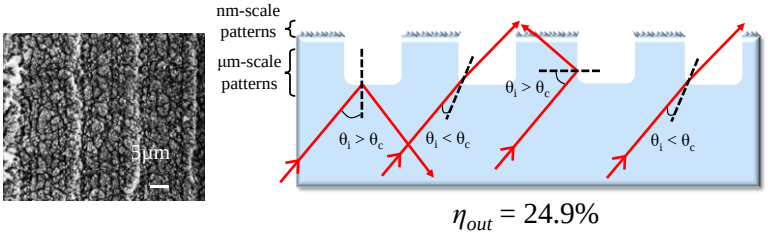

Fig. 3.22 SEM images (left images) and light outcoupling enhancement mechanism (right cross-sectional schematic diagrams) for cylindrically shaped patterns arranged in a hexagonal lattice that exclude (top) and include (bottom) nm-sized surface roughness.

Fig. 3.22 illustrates the comparison between the η_{out} of experimentally fabricated OLED devices having air/glass patterns that exclude and include nm-sized rough surface patterns. The top-view SEM images of the air/glass patterns are on the left and the proposed mechanism of light outcoupling enhancement are illustrated on the right. The results show that by combining patterns of smaller pitch and including nm-sized surface roughness between the hole patterns, the η_{out} ($\Delta\ \eta_{out}$ compared to non-patterned devices) can be enhanced from 21.5% (7.4%) to 24.9%

(24.4%). This represents an impressive 3x increase in $\Delta\eta_{out}$ for cylindrically shaped holes arranged in a hexagonal packing lattice. Indeed, the smaller pitch increases the hole packing density and probability of light rays meeting a new surface normal (as explained in detail in Section 3.4). Where light rays would have initially experienced TIR events and remain trapped within the substrate as substrate guided modes, the nm-sized surface roughness areas in between the holes provide additional scattering centres for the redirection of light into free space. The nm-sized surface roughness covers a much larger area compared to the ideal contact point of cylindrical holes for ray outcoupling, thus accounting for the high η_{out} compared to OLED devices without any rough surface.

This study implies that a higher η_{out} in OLED devices with optimized air/glass patterns dimensions (conical hole shape, 1 μm EE distance) inclusive of nm-size rough surfaces should be expected once drawbacks related to fabrication constraints are overcome in the future. The air/glass hole patterns via femtosecond laser may also be applied to flexible plastic substrates and provide an advantage over popular outcoupling structures (ex. hemispherical macro lenses) in that they are amenable to flexible/foldable needs. Hemispherical macro lens cannot contour to any shape outside of a flat surface and thus are not amenable to aesthetic applications that require the bendability/flexibility of OLEDs.

Chapter 4
Reducing losses to evanescent modes via TDM orientation

4.1 Introduction

The thermal evaporation of small molecule fluorescent emitters is well known in literature to produce films with randomly oriented molecular chains. Controlling the molecular orientation in the *x*-*y*-*z* plane for Alq_3 used in the previous Sections during the vacuum evaporation is especially difficult due to its compact nature and is not practically feasible for large scale manufacturing.[142] Fig. 4.1 (a) illustrates an TDM orientation of Alq_3 where thin film deposition via vacuum evaporation produces amorphous thin films with isotropic molecular orientation.[143–145] Losses to evanescent modes through the coupling of TM-polarized radiation with SPs at the organic/cathode interface is therefore inevitable since isotropic oriented emitters are classified to have 1/3 of their TDM oriented vertically with respect to the *x*-*y* plane of the substrate. This is the largest loss that accounts for about 40% of the light generated within OLEDs according to Fig. 3.19 and therefore significantly reduces the far-field luminous intensity and overall η_{ext}.[146] Indeed, the patterns

made at the air/glass substrate interface cannot suppress losses to evanescent modes since the TM-polarized radiation and coupling events are confined to the organic/cathode interface. It is logical to therefore appreciate that non-patterned and patterned OLED devices exhibit the same contributions to evanescent modes (Section 3.5.3).

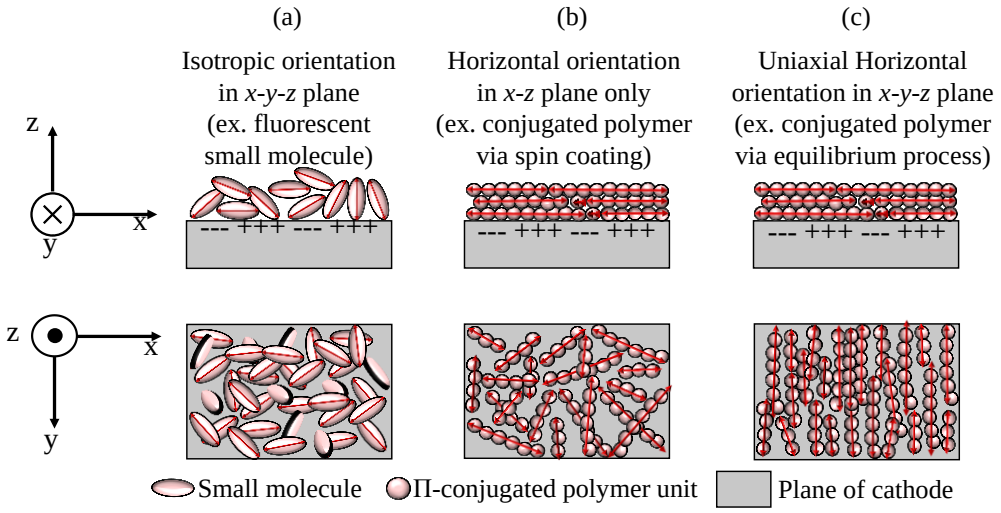

Fig. 4.1 TDM orientations in (a) isotropic (b) horizontal *x*-*z* plane and (c) uniaxial horizontal orientation in *x*-*y*-*z* plane.

The solution for eliminating losses to evanescent modes is by controlling the orientation of TDM in the emissive species. High η_{ext} > 29.6% have been realized in OLED devices utilizing small molecule TADF emitters without additional outcoupling structures thanks to advances in molecular design which promote near exclusive horizontal molecular orientation and high ϕ_{PL}.[82),147)–150)] Small molecule

devices deposited from vacuum evaporation processes are very unattractive for large scale production due to limited substrate scalability. Conversely, luminescent π-conjugated polymer emitters provide an excellent alternative to small molecule emitters. They can be deposited from solution processes (ex. spin coating) and their intrinsic horizontal orientation of the TDM vector relative to the *x*-*z* plane of the substrate as shown in Fig. 4.1 (b) make them amenable for both large-scale manufacturing the realization of OLEDs with high η_{ext}, respectively. OLEDs using these emitters therefore experience reduced losses to evanescent modes due to a negligible proportion of TM-polarized radiation from vertically oriented TDMs and outcoupled modes are enhanced by 45% (Fig. 4.2).[10),151)]

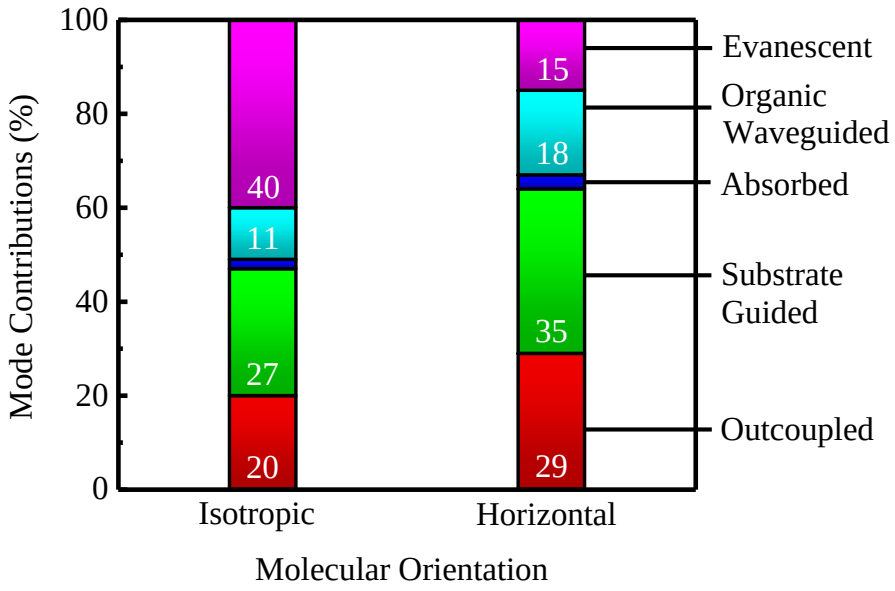

Fig. 4.2 Simulated mode contributions of OLED devices with isotropic and purely horizontally oriented molecular orientation.

High efficiency OLED displays for practical applications demands that scientist engineer solutions that consider the structure of the multi-level panel. OLED panels are currently fitted with circular polarizers to improve the colour quality and ambient contrast ratio (CR) from the display by eliminating reflected ambient light.[152),153)] The schematic for this mechanism is represented in Fig. 4.3. The unpolarized ambient light first passes through a linear polarizer (with a vertically oriented transmission axis) and will become vertically polarized relative to the direction of propagation. The polarized light passes through a quarter-wave ($\lambda/4$) retardation film which generates right circularly polarized light (r-CPL). After passing through the OLED transparent substrate and organic thin films, the r-CPL

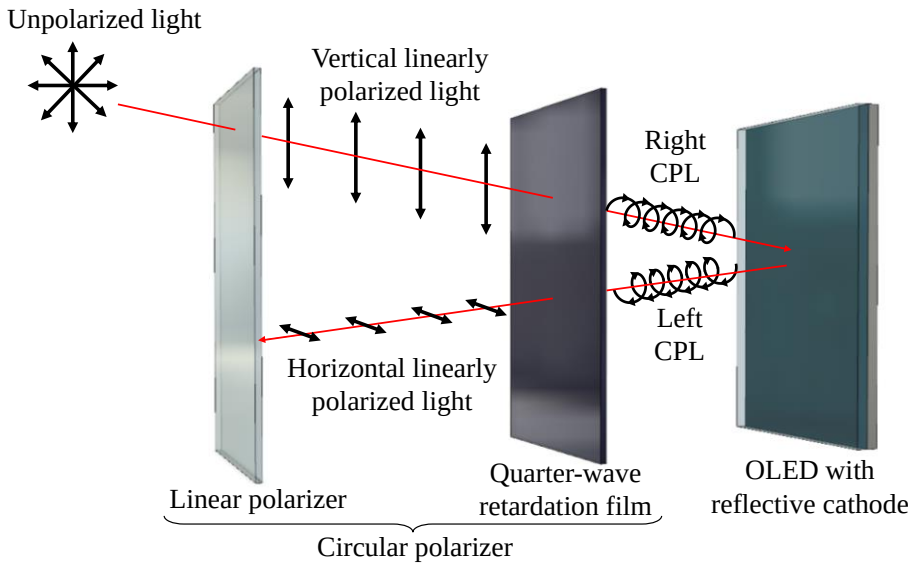

Fig. 4.3 Mechanism of how the circular polarizer reduces the reflection of ambient light (red line depicts direction of light propagation).

is reflected by the metal cathode and becomes left circularly polarized light (l-CPL). L-CPL becomes horizontally polarized after passing through the $\lambda/4$ retardation film and is then blocked by the linear polarizer since its transmission axis is oriented in the vertical direction.[154] While the circular polarizer mechanism significantly reduces ambient reflection to only 4-6%, the implication of including a linear polarizer is that it diminishes the radiative emission and η_{ext} from an OLED device that utilizes an isotropic emitter (ex. Alq_3) by 50%.[155),156]

A solution to overcome the problem of light loss due to the linear polarizer is to have the OLED produce intrinsic linearly polarized emission (LPE). In this case, 100% of the outcoupled modes will be allowed to pass through the linear polarizer and the η_{ext} will not be diminished. LPE can be realized by the uniaxial orientation of the TDM[157)–159)] since the TDM vector lies along the longest backbone axis of the molecular chain and is the typical situation for luminescent π-conjugated polymer species.[10)] High degrees of LPE also expand the application of OLEDs to being suitable 3D display sources since the image quality depends on elimination of cross-talk between orthogonally polarized sources.[160)] The ideal alignment of the TDM in the emitting species is described in Fig. 4.1 (c) where uniaxial alignment in all planes is achieved. Non-equilibrium and fast drying solution deposition processes like spin coating, however, exert no driving force to control the directional preference of the molecular chains in the *x-y* plane[161)] and are not

attractive for high through-put manufacturing and are difficult to scale using large substrates.

Past research efforts to achieve LPL from OLED devices include controlling the uniaxial orientation of the molecular chains in the popular fluorescent conjugated emissive polymer poly(9,9-di-n-octylfluorenyl-2,7-diyl)-alt-(benzo[2,1,3]thiadiazol -4,8-diyl)] (F8BT). The well-studied "rubbing" technique involves spin coating F8BT over an underlying rubbed polyimide film[162),163)] or rubbed PEDOT:PSS[164)] followed by annealing to induce the alignment of molecular chains. This technique was also successful in achieving uniaxial orientation in poly(p-phenylenevinylene) (PPV) as the emitter and rubbed species. An alternative to rubbing is the nanoconfinement technique that has shown promise for aligning conjugated polymers for both OLED and organic field effect transistors (OFET)[165)] applications. This process typically involves a master cast template with nanochannels of dimensions varying between 50 - 500 nm that is used to imprint the polymer thin film during annealing. During this process the polymer chains self-organize in a liquid crystalline phase with the backbone oriented uniaxially in the direction of the grooves.[166),167)] The friction-transfer technique has previously been applied to Poly (9,9-dioctylfluorene) (PFO) wherein a 'pellet' of the material is drawn directly over a heated ITO substrate and molecular chains uniaxially align in the drawing direction.[168)] The techniques mentioned above are physically invasive

and require many pre- and post-deposition steps that may disturb the purity of the thin film EML and further complicate the OLED fabrication process. Self-assembly solution processable deposition techniques that support uniaxial molecular alignment are much more attractive since the alignment and thin film formation processes occur simultaneously. The need for pre- and post-processing steps become unnecessary to induce molecular alignment and the OLED fabrication process can be simplified.

Researchers have looked towards meniscus guided coating (MGC) techniques as viable alternatives for simultaneous molecular alignment and thin film deposition. The general working principle across all techniques includes the linear translation of either the substrate or a coating tool that directs the movement and formation of a solution meniscus. The three-phase contact line promotes solvent evaporation, solution concentration behind the meniscus and precipitation for film formation. The molecular alignment is supported by directional fluid flow and shearing mechanisms within the bulk of the solution and interactions closer to the substrate surface, respectively.[169)] The majority of MGC methods to obtain highly aligned molecular films have been applied for the purpose of achieving highly efficient OFET devices. Achieving good control over morphology, microstructure and resulting crystalline domains are crucial parameters for realizing

good charge transport properties and overall device performance.[161),170),171)] This area of study is therefore of key interest to both OLED and OFET applications.

Many MGC techniques exist for the formation of thin films with highly oriented molecular chains. The solution shearing coating technique illustrated in Fig. 4.4 (a) involves the deposition of a small volume droplet of solution onto a substrate mounted on a translational stage and a stationary shearing blade. The movement of the substrate at a set speed exposes the meniscus to air for drying and

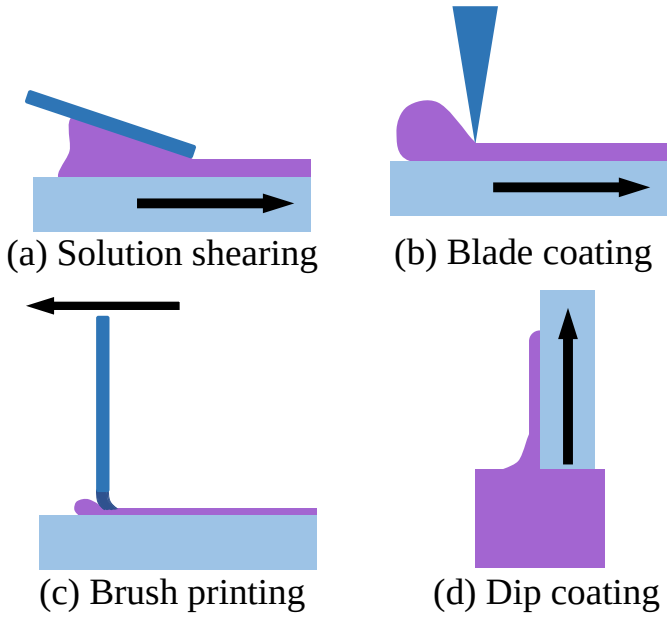

Fig. 4.4 Schematic of meniscus guided coating techniques for the deposition of aligned films for organic electronic devices: (a) solution shearing, (b) blade-coating, (c) brush painting and (d) dip coating.

film formation. High degrees of molecular alignment in the direction of the substrate translation direction have been achieved by tuning the polymer solution concentration and substrate speed. The improved molecular alignment demonstrated drastic improvements in the charge transport anisotropy in subsequently fabricated OFET devices.[172),173)] Modifications to the solution shearing technique include the use of shearing blades fashioned with micropillar patterns to enhance the extensional flow field alignment of molecular chains[174)] or applying an E-field to the shearing field whereby molecular alignment is supported by dielectrophoresis forces.[175),176)] The most attractive feature of utilizing an E-field to induce molecular alignment is its chemically agnostic nature: it can be universally applied to a variety of polymer and small molecule emitter species and is independent of material specific interactions. The blade coating technique shown in Fig. 4.4 (b) has a similar setup to solution shearing and exercises similar mechanisms for molecular alignment.[177)] The brush printing technique shown in Fig. 4.4 (c) utilizes a brush attached to a translation stage placed over a stationary substrate and the movement rate of the meniscus is controlled by the movement of the fibres. Extensional and shearing flow fields beneath and between the fibres induce high levels of molecular alignment in the direction of the brush movement and is most suited for thin films less than 100 nm thick.[178)] The dip coating technique shown in Fig. 4.4 (d) involves immersing a substrate attached to a mechanical arm that controls its withdrawal rate from the solution where the

meniscus is formed at the surface. Optimization of withdrawal speed, tilting angle[179] and surface energy of the substrate are key parameters for achieving continuous films with good molecular alignment and charge transport anisotropy.[180]

Dip coating techniques have been widely regarded as the key methodology to fabricating large area OLEDs. To the best of our knowledge, there have not been reports of OLED devices fabricated from any dip coating technique derivative that have demonstrated high degrees of molecular chain alignment and LPE.[96),98] The aim of this study is to develop a MGC technique that is suited for this purpose which can adequately satisfy realistic and scalable fabrication needs. A 'solution withdrawal coating (SWC)' technique is proposed wherein the substrate remains stationary and the solution is withdrawn at a fixed speed. The SWC technique eliminates the need for translational stages or mechanical arms used for supporting substrates. Easy scalability to large area and non-uniform substrates, material conservation and films with preferential uniaxial molecular alignment akin to literature can therefore be realized. The proof-of-concept achieved is expected to be chemically agnostic and universal to all conjugated polymers used as the emitting layer for OLEDs, irrespective of their intrinsic solution-state alignment.

4.2 Experimental

4.2.1 Materials

In addition to the materials previously mentioned in Section 3.3, the following materials were used in the film preparation and device fabrication processes throughout the rest of this study.

Poly(9,9-di-n-octylfluorenyl-2,7-diyl)-alt-(benzo[2,1,3]thiadiazol-4,8-diyl)] (F8BT)

The chemical structure of F8BT is shown in Fig. 4.5 and is commonly used in solution processed OLEDs as a fluorescent emissive layer thanks to its solubility in various low and high boiling point organic solvents.[164] The energy band of its HOMO and LUMO lie around -5.9 eV and -3.5 eV, respectively[181] and are appropriate for the efficient injection of electrons and confinement of holes for the exciton formation process.

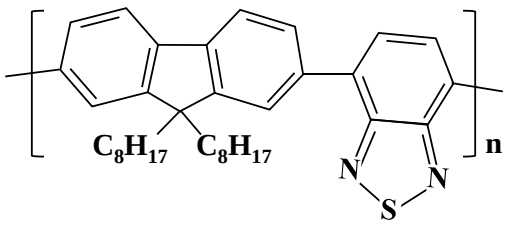

Fig. 4.5 Chemical structure of F8BT.

Poly(9,9-dioctylfluorene-co-N-(4-butyl- phenyl)-diphenylamine) (F8-TFB)

The chemical structure of F8-TFB is shown in Fig. 4.6 (a) and is used in solution processed OLEDs as a hole transport/electron blocking layer since its HOMO and LUMO energy band are around -5.3 eV and -2.3 eV, respectively.[182)]

Poly(3-hexylthiophene) P3HT

The chemical structure of P3HT is shown in Fig. 4.6 (b) and is commonly used in the OSC field as the electron donor species.[183),184)] P3HT readily achieves solution-state alignment via the formation of polymer fibrils prior to thin film formation[185)] and will be used as a "proof-of-concept" polymer to demonstrate uniaxial alignment in the SWC process.

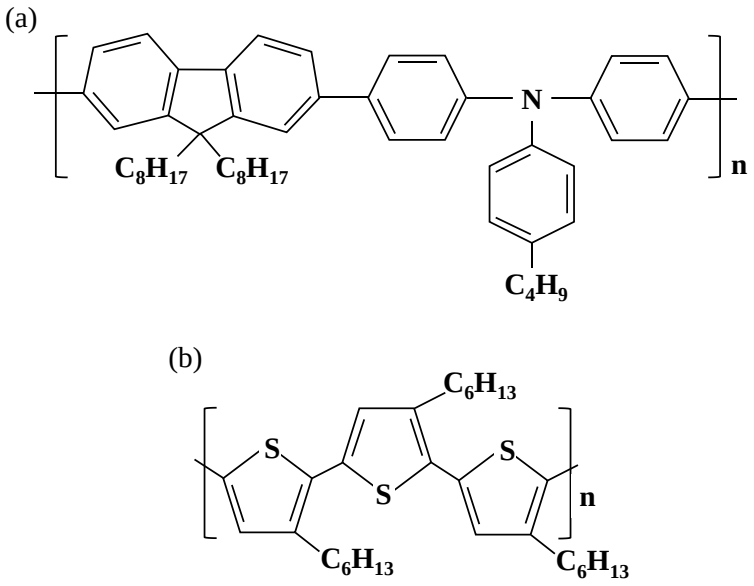

Fig. 4.6 Chemical structure of (a) F8-TFB and (b) P3HT.

Solvents

The solvents are used to dissolve the polymers for deposition during spin coating or SWC processes. The chemical structure for p-xylene, dichloromethane and chloroform are shown in Fig. 4.7 (a), Fig. 4.7 (b) and Fig. 4.7 (c), respectively. P-xylene (purity > 98.0%) and chloroform (spectroscopic grade stabilized by amylene, purity > 99.0%) were both supplied by Kanto Chemical and dichloromethane (DCM) (amylene stabilizer, anhydrous > 99.6%) was supplied by Sigma Aldrich. The boiling points for p-xylene, dichloromethane and chloroform are around 138 ^{o}C, 39 ^{o}C and 61 ^{o}C respectively.

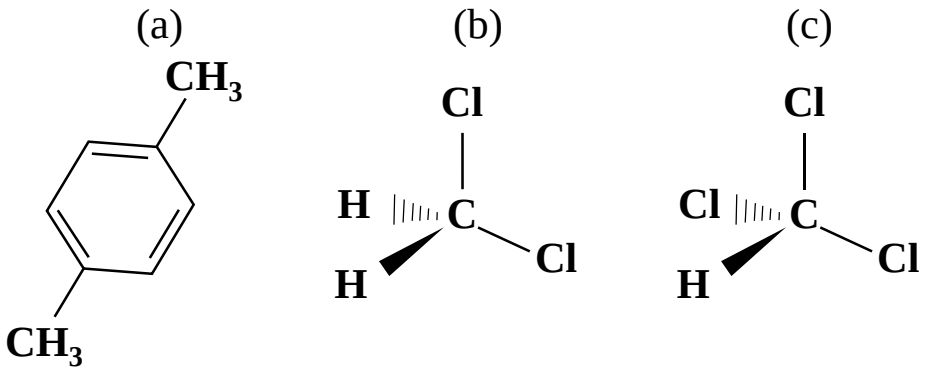

Fig. 4.7 Chemical structures of solvent used throughout this study: (a) p-xylene (b) dichloromethane and (c) chloroform.

4.2.2 Solution processed OLED device fabrication

Glass substrates with pre-deposited ITO of 150 nm thickness were ultrasonicated in sequential baths of acetone, semicoclean, pure water and finally isopropyl alcohol in a clean room. To increase the work function of ITO and remove excess organic contaminants, all substrates were placed in a closed chamber for UV-Ozone irradiation treatment for 30 minutes.[132)–134)] PEDOT:PSS was then filtered through a 0.45 μm polyvinylidene difluoride (PVDF) filter and spin coated over the ITO at 1600 RPM for 30 s followed by annealing at 100 ^{o}C for 10 minutes to remove any excess solvent. The resulting PEDOT:PSS film is about 70 nm thick and serves as the hole injection layer.

The substrates were then moved from the clean room and into a nitrogen (N_2) filled glovebox. In the glovebox a 9.38 mg/mL solution of F8-TFB and 18.5 mg/mL solution of F8BT were both prepared using p-xylene as the solvent. Both solutions were filtered through a 0.2 μm polytetrafluoroethylene (PTFE) filter prior to deposition. F8-TFB was spin coated over the PEDOT:PSS layer at 1600 RPM for 30 s followed by annealing at 180 ^{o}C for 15 minutes. F8BT was then spin coated over the F8-TFB at 2000 RPM for 30 s followed by annealing at 130 ^{o}C for 10 minutes. The thicknesses of F8-TFB and F8BT were determined to be about 30 nm and 63 nm respectively. The substrates were then transferred to the ultra-high vacuum evaporator with a base pressure of 10^{-8} Torr where 3 nm of LiF was

deposited at rate of 0.01 nm/s and 100 nm of Al was deposited at a rate of 0.2 nm/s. Following the device fabrication, all devices were moved to a nitrogen (N_2) filled glovebox via a small vacuum shuttle chamber, wherein they were encapsulated using a glass cover with attached thin desiccant film and UV-cured epoxy seal. This process was done so all devices may be evaluated in air void of oxygen/moisture degradation effects.[135),136)]

4.2.3 Solution withdrawal coating

The schematic of the proposed SWC setup is described in Fig. 4.8 where two substrates are held upright by substrate holders in a cuvette filled with a desired polymer solution. The solution is withdrawn from the cuvette through a needle attached to a glass syringe. The body of the syringe is kept stationary by a stage while its plunger is connected to a mechanical syringe pump that controls the withdrawal rate of the plunger and the solution from the cuvette. The downward motion of the solution during withdrawal directs the movement of the meniscus down the length of the substrates leaving behind the solid polymer film. This deposition method is used to produce polymer films with high degrees of uniaxial alignment. The inset of Fig. 4.8 shows the dual substrate setup where the substrates are separated by 2.35 mm. The substrates are either held upright in a non-tilted fashion or tilted by 21^o during the SWC process.

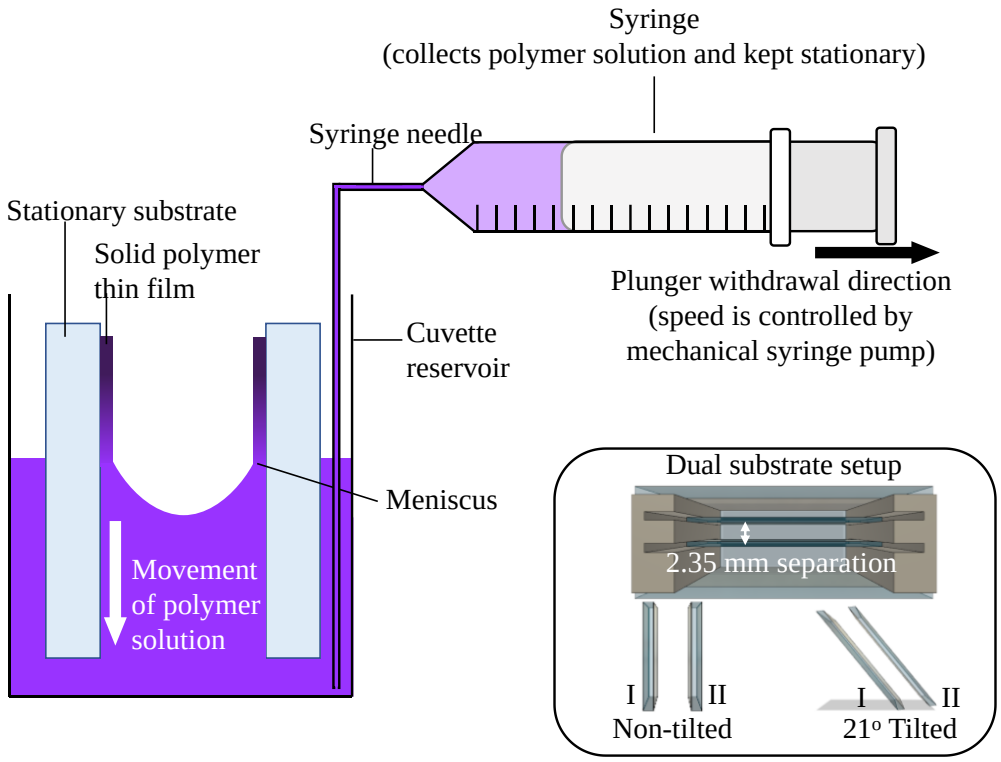

Fig. 4.8 Schematic for the solution withdrawal coating (SWC) process. Inset shows dual substrate setup in non-tilted and tilted configurations.

4.2.4 Film and OLED device characterization

Film thicknesses were evaluated using an atomic force microscope (AFM) (VN-8000 Keyence) and the thickness mapping of SWC samples were performed using an optical thickness meter (Otsuka OPTM-A1). The phase images of the films were evaluated using a scanning probe microscope in tapping mode (Hitachi AFM5000 II) with a micro cantilever (type SI-DF20). The absorbance spectra of thin film samples were performed using a UV-Vis spectrophotometer (JASCO V770). By fitting a linear polarizer in front of the light source, the polarized absorbance spectra were used to evaluate the molecular alignment of TDM (Fig. 4.9 (a) and (b)). The polarized luminance spectra were used to characterize the polarization state of the OLED electroluminescence. The device was driven at a constant current density and positioned in front of a linear polarizer and luminance meter (Topcon BM-902). The polarizer is rotated relative to the *x-y* plane of the device and the luminance as a function of the polarizer's transmission axis is recorded (Fig. 4.9 (c)).

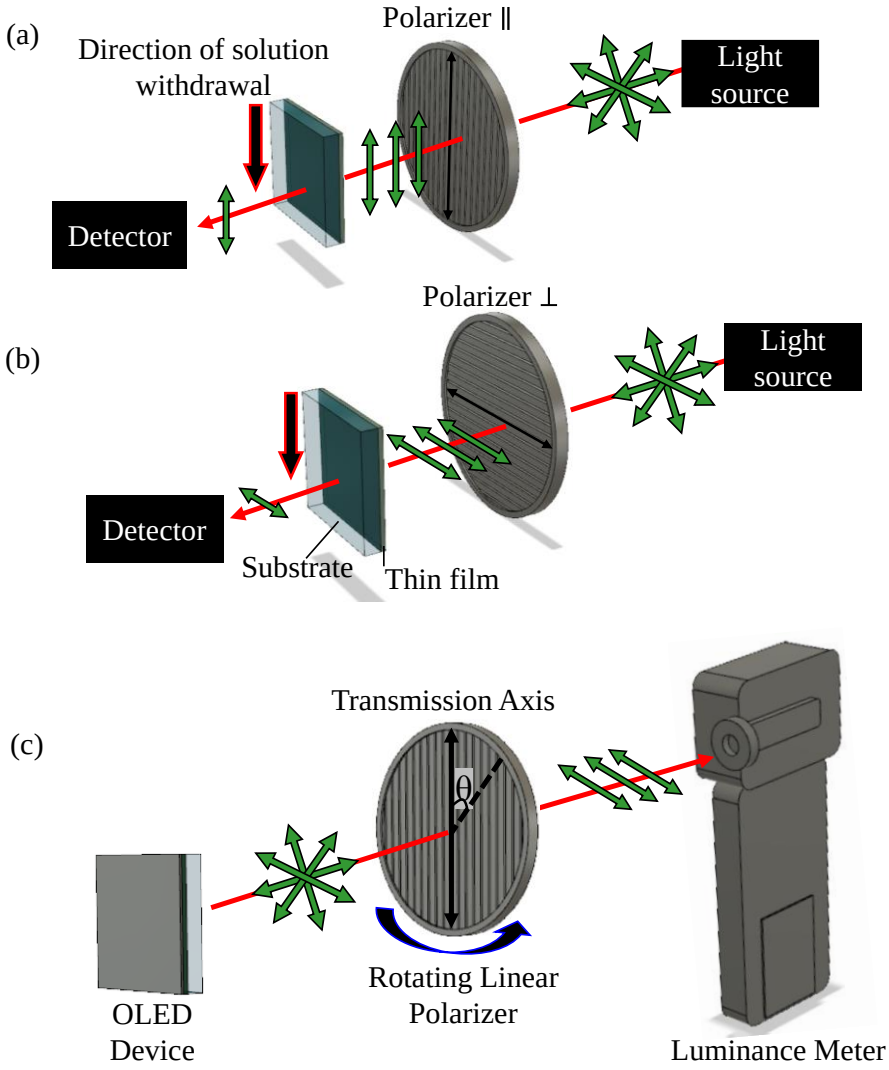

Fig. 4.9 Schematic of setup used to measure polarized absorbance of thin films where the polarizer and solution withdrawal direction are oriented (a) parallel or (b) perpendicular to each other and (c) schematic of setup for measuring polarized luminance of OLED devices.

The TDM of conjugated polymers used for OLED, OFET and OSC applications principally lies along the long axis of the polymer chain backbone. The absorbance spectra will therefore be most intense when the orientation of the polarized light and TDM are aligned parallel to each other.[186] The orientation of the TDMs can be quantified by the dichroic ratio ($D = A_{\parallel} / A_{\perp}$): the ratio between the parallel ($A_{\parallel}$) and perpendicular ($A_{\perp}$) absorbance intensity at the primary electronic transition wavelength (peak of absorbance spectra). This characterization technique therefore does not reflect a 3D description of TDM orientation and can only be used to assess in-plane alignment (although a non-zero orientational component in the *z*-axis may exist). Nevertheless, the dichroic ratio scales with the magnitude of TDMs along the light source polarization direction where $A_{\parallel} \propto \langle cos^2\theta \rangle$ and θ is the angle between the TDM and light polarization axis.[187] Purely isotropic orientation of the polymer chains and TDMs correspond to a dichroic ratio of 1. A dichroic ratio greater (less) than 1 indicates preferential orientation of the polymer chains parallel (perpendicular) to the direction of withdrawal.

4.3 Spin coated F8BT and vacuum evaporated Alq_3 OLED devices

The performance of OLED devices made from vacuum evaporated (small molecule Alq_3 EML) and spin coated processes (conjugated polymer F8BT EML) will first be compared to assess the impact of intrinsic isotropic and horizontally oriented emitters (relative to *z*-axis only), respectively, on the practical η_{ext}. The device characteristics of the F8BT and Alq3 devices are shown in Fig. 4.10.

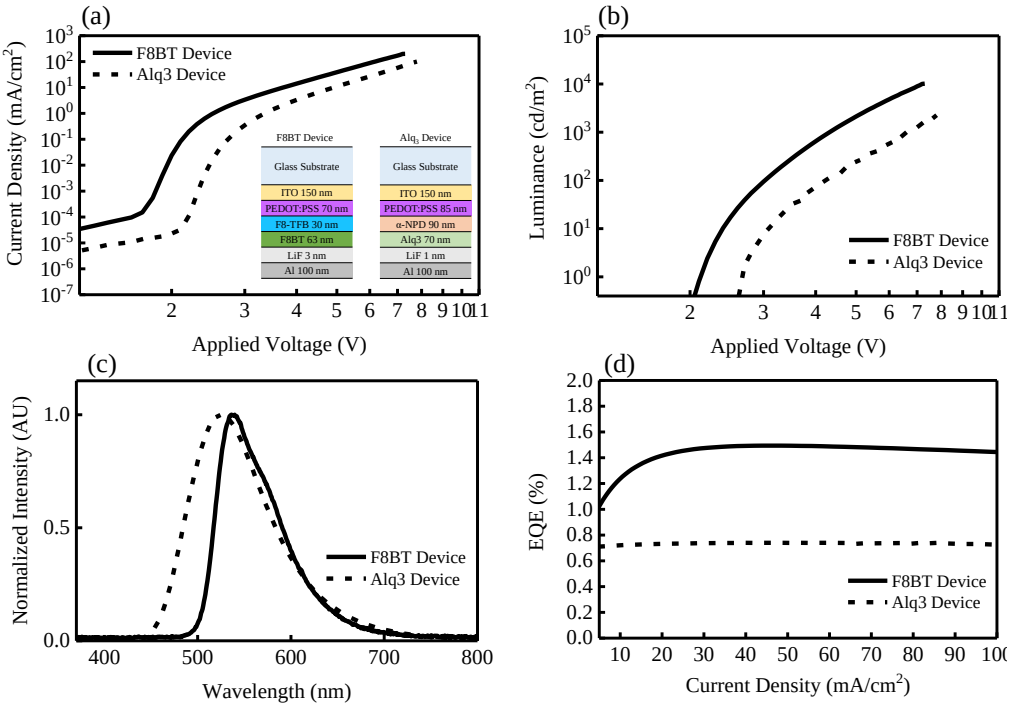

Fig. 4.10 (a) *J-V*, (b) *L-V*, (c) El spectra and (d) EQE device characteristics of F8BT and Alq3 devices.

The results show that the *J-V* characteristics between the devices in Fig. 4.10 (a) do not overlap, where the F8BT device turn-on voltage (1.9 V) is much lower than the Alq_3 device (2.4 V) and generates higher current as the driving voltage increases. The different internal device structures utilized by each device dictate that the charge injection characteristics will not be the same and indeed follows that η_{int} will be different. Although both devices emit within the green region of the visible region as shown in the EL spectra of Fig. 4.10 (c) and are fluorescent emitters (therefore similar η_{exc}), their ϕ_{PL} are different. According to literature, the ϕ_{PL} of F8BT in xylene can range between 48.3 – 77.0%[188] and ϕ_{PL} of Alq_3 films may vary between 22 – 32%.[189),190] The superior current generation and ϕ_{PL} in F8BT therefore infers superior η_{int} over Alq_3 devices and will lead to higher luminance at the same driving voltage (Fig. 4.10 (b)). Coupled with a possible higher degree of horizontal alignment of molecular chains relative to the *x-y* plane of the substrate in F8BT[151], these devices will exhibit superior η_{ext} compared to Alq_3 devices (Fig. 4.10 (d)) due to reduced losses to evanescent modes.

In summary, the superior η_{ext} in F8BT devices may be attributed to enhancements in both η_{int} (charge injection characteristics and ϕ_{PL}) and η_{out} (horizontal TDM (Fig. 4.1)). Although each parameter may not be isolated to elucidate their empirical influence on the η_{ext}, conjugated polymer OLEDs clearly provide an avenue for enhanced η_{ext} from a materials engineering perspective.

4.4 Alignment in spin coated F8BT films and OLED devices

The polarized absorbance spectra of a spin coated 67 nm thick F8BT film over a glass substrate is first demonstrated in Fig. 4.11, where the glass substrates were cleaned and treated prior to film deposition in the same manner as ITO substrates described in Section 3.2. The primary electronic transition between the ground and excited states of F8BT occurs around 465 nm and corresponds to the peak absorbance intensity from which the dichroic ratio is calculated. The spectra shows equal absorbance intensity when the polarizer's axis is oriented in a parallel

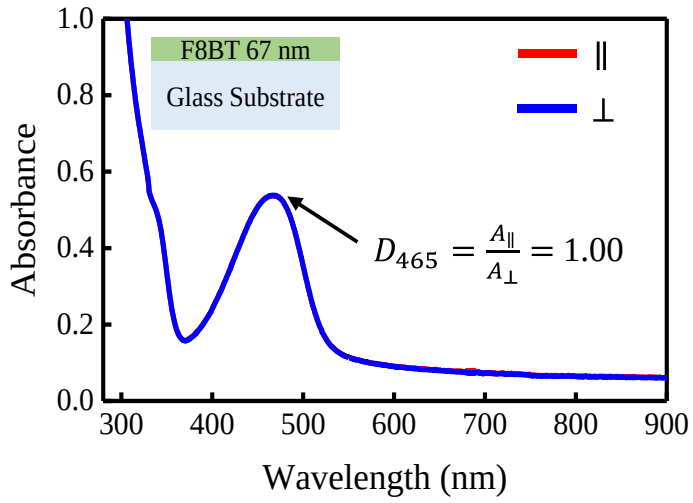

Fig. 4.11 Polarized absorbance spectra of F8BT film deposited from spin coating (inset shows schematic of F8BT film over glass substrate).

and perpendicular direction relative to the film (dichroic ratio = 1). This indicates that although the polymer chains in F8BT deposited from spin coating may have high degrees of orientation relative to the *z*-direction (horizontal orientation, lying on the substrate) they demonstrate isotropic orientation relative to the *x*-*y* plane. The polarized luminance of a spin coated F8BT OLED device is shown in Fig. 4.12 and indicate that there is no preferential polarization state of the device's emitted electroluminescence. This agrees with Fig. 4.11 such that isotropic polymer chain orientation results in non-polarized electroluminescence. It is apparent that spin coating cannot induce uniaxial orientation of F8BT films, therefore the deposition of F8BT via SWC will be investigated.

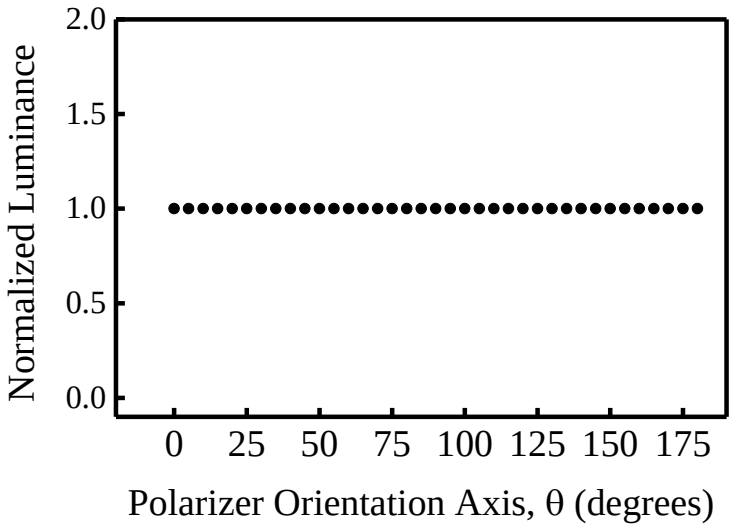

Fig. 4.12 Polarized luminance of spin coated F8BT OLED device driven at 25 mA/cm^2.

4.5 SWC F8BT films

The thicknesses and overall uniformity of SWC films are determined by the withdrawal rate of the solution and solvent evaporation rate. Fig. 4.13 shows the evolution of thin film thickness for various withdrawal speeds during the SWC process (single substrate configuration) using a 10 mg/mL solution of F8BT (M_w 39,000 g/mol) in p-xylene over glass substrates at room temperature. The plotted thicknesses and error bars represent an average of 225 points taken over a 169 mm^2 area in the centre of the substrate. The graph shows that the trend of film thickness is not directly proportional to the withdrawal speed and give rise to 3 regimes of deposition: the evaporative, transition and Landau-Levich (LL) regime.

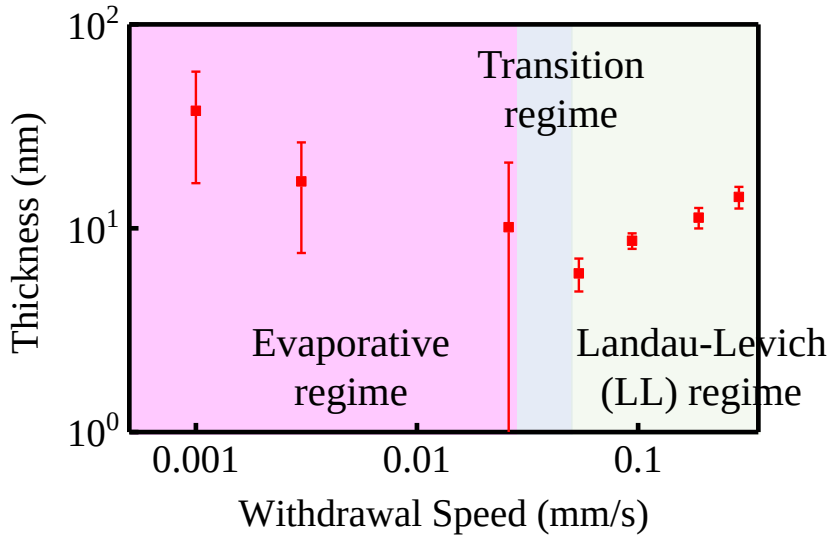

Fig. 4.13 SWC F8BT film thickness with varying solution withdrawal speeds.

These regimes arise because of differing dynamics that control film formation at low and high withdrawal speeds. The mechanisms of film formation in the evaporative and LL regimes are shown in Fig. 4.14 (a) and Fig. 4.14 (c),

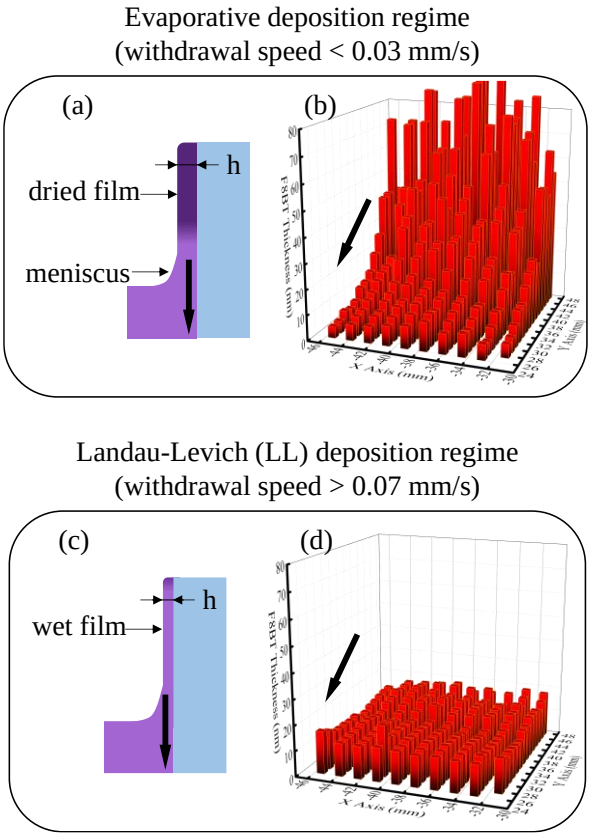

Fig. 4.14 A schematic of film formation mechanisms in the (a) evaporative and (c) LL regimes of deposition. Examples of the thickness distribution of F8BT films over a 169 mm^2 area of the substrate in the (b) evaporation and (d) Landau-Levich (LL) regimes of deposition. The black arrow indicates the direction of menisucs movement; from the top to the bottom of the substrate.

respectively. In the evaporative regime, the rate of solvent evaporation and solution withdrawal occur on similar time scales resulting in film formation in front of the meniscus contact line. Capillary flow forces solution to rush behind the meniscus and establishes a continuous concentration gradient supply of solute (like the coffee ring effect). This process is supported by the out-of-plane temperature gradient between the bulk solution and thin film that arises from evaporative cooling at the air-liquid interface. The thickness of the film is characterized by the power law decrease relationship described by Equation 4.1 where h is the film thickness, C is the solution concentration, Q_{evap} is the rate of solvent evaporation, ρ is the solute density, L is the meniscus width and v is the withdrawal rate of the solution.

$$h = \frac{C Q_{evap}}{\rho L} v^{-1} \tag{4.1}$$

In the LL regime, the solvent evaporation rate is much slower than the withdrawal rate and thus a wet film is first drawn out on the substrate and followed by subsequent drying of the film.[173),179),191)] The film thickness can be characterized by a power law increase and the relationship is described by Equation 4.2 where η is the solution viscosity and g is the gravitational constant. The precise power exponent in the evaporative and LL regime will therefore depend on the evaporation rate of the solvent and solution viscosity, respectively.[161)]

$$h = C \left(\frac{\eta v}{\rho g}\right)^{\frac{1}{2}} \tag{4.2}$$

The unique setup used in the SWC process where the film is never fully exposed to air gives rise to unique thickness distributions compared to other MGC techniques where films deposited in the evaporative region exhibit poor uniformity down the length of the substrate shown in Fig. 4.14 (b). During solution withdrawal, the solvent evaporates and the vapour pressure entrained between the substrate and cuvette wall increases. Increasing vapour saturation decreases the solvent evaporation rate and solution behind the meniscus, thus resulting in thinner films. Conversely, the films fabricated in the LL regime show much better uniformity as illustrated in Fig. 4.14 (d). Film formation in this regime is based purely on viscous flow dynamics and is independent of the solvent evaporation rate. Small differences in evaporation rate due to increasing vapour pressure of the solvent therefore has an almost negligible effect on film formation.

The aperture size of the UV-Vis spectrophotometer is only 20 mm^2, therefore correlating these results to an average thickness taken over a 169 mm^2 area of the substrate would be inappropriate, thus a 36 mm^2 area will be used. Common among MGC technique literature sources is that the evaporative regime of thin film deposition is most optimal for achieving molecular alignment. Unidirectional extensional flow fields and shearing forces are exerted on the molecular species to induce polymer chain alignment in this slow evaporation rate region. The evaporative regime will therefore be of primary investigation in this study.[192),193)]

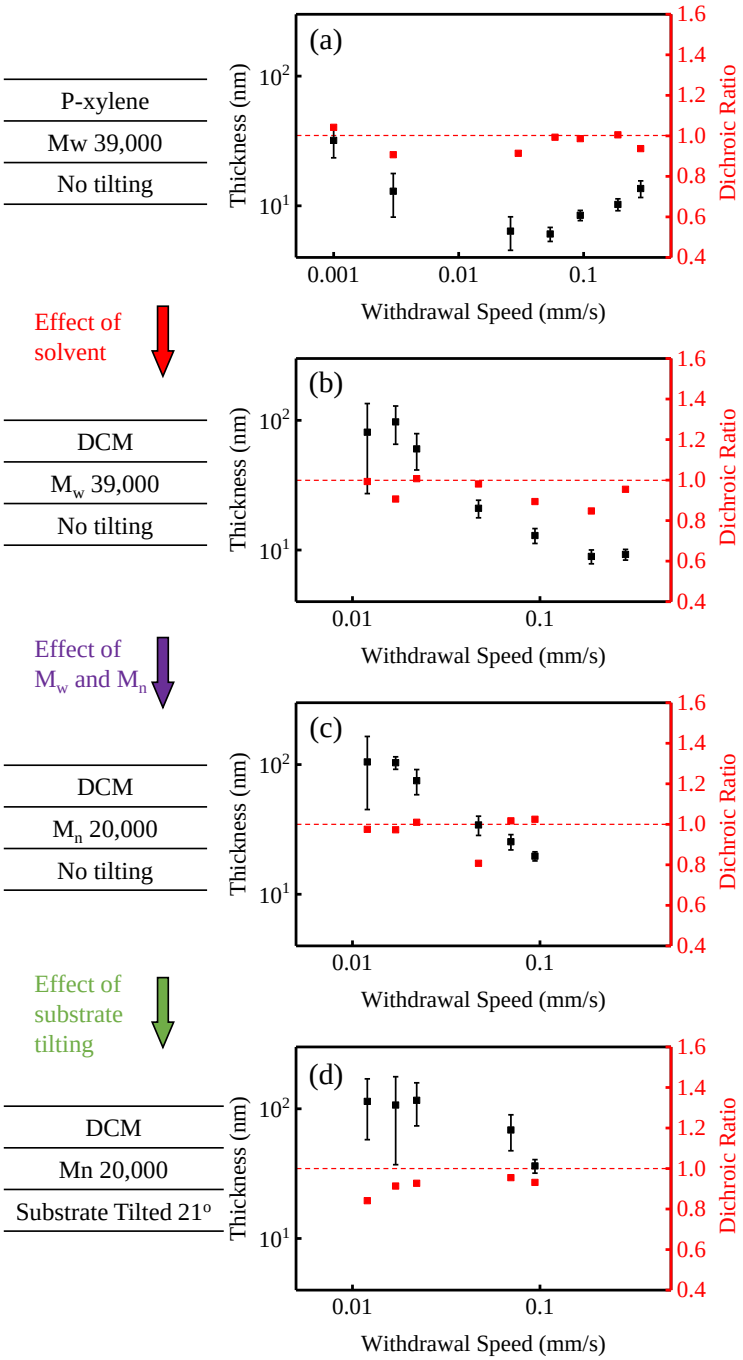

Fig. 4.15 Thickness (black plotted points) and dichroic ratios (red plotted points) for SWC F8BT films deposited under various fabrication conditions.

Fig. 4.15 shows the evolution of film thickness and dichroic ratios of SWC films as a function of withdrawal speed and various fabrication conditions. The dotted red line indicates the dichroic ratio of 1 and isotropic molecular orientation; plotted points above (> 1) and below (< 1) indicates preferential orientation of molecular chains in the parallel and perpendicular directions to withdrawal. By changing the solvent from p-xylene in Fig. 4.15 (a) to DCM in Fig. 4.15 (b), all the thin film deposition regimes can be shifted to faster withdrawal speeds where thicker films can be obtained. This is due to the lower boiling point, higher volatility and faster evaporation rate of DCM compared to p-xylene. Varying the withdrawal speed has been shown in past literature (ex. in the solution shearing technique) to affect the shearing rate of polymer chains within the bulk of the solution, wherein preferential alignment can be achieved.[172),173)] The dichroic ratios for films made from p-xylene in Fig. 4.15 (a) and DCM in Fig. 4.15 (b), however, all maintain dichroic ratios near to 1 and suggests isotropic molecular chain alignment in the *x*-*y* plane. Neither changes in film formation dynamics nor evaporation rate affect molecular orientation of the F8BT chains.

Other studies have suggested that by utilizing an intermediate M_w (M_n) of the conjugated polymer and optimizing the withdrawal speed, tuning of the uniaxial alignment can be achieved.[174)] The F8BT with M_n of 20,000 g/mol, however, also demonstrates negligible preferential alignment in films of varying thicknesses as

shown in Fig. 4.15 (c). The shape of the meniscus in previous studies have also demonstrated a direct impact on film formation and molecular alignment where Equation 4.1 dictates that a smaller meniscus results in thicker films. When the substrate is tilted by 21^{o} away from the meniscus, its shape and solute entrainment region becomes smaller. Mass transport of the solute can be enhanced, and this results in the thicker films observed for tilted substrates in Fig. 4.15 (d) compared to non-tilted substrates under similar withdrawal rates in Fig. 4.15 (c). Fig. 4.15 (d) shows a generally weak preferential alignment of molecular chains perpendicular to the direction of withdrawal over all thicknesses (dichroic ratios all less than 1). This suggests that the smaller meniscus promotes greater interaction between polymer chains in the bulk and shear dominant forces. The dynamics between a non-slip boundary at the solution/substrate interface and drag forces within the bulk can force polymer chains to turn clock-wise and align perpendicular to the direction of the moving meniscus.[173)]

In summary, the F8BT polymer chains exhibit very weak preferential molecular chain alignment response to SWC i.e., they remain near isotropic orientation in the *x-y* plane of the substrate. The macroscale dynamic forces used in SWC (ex. extensional flow, shearing fields, etc.) cannot effectively overcome the nm-scale entanglements of the F8BT polymer chains and so realizing uniaxial orientation of un-treated F8BT solution cannot be realized.

The absence of any solution-state alignment/aggregation of F8BT polymer chains to induce the formation of larger scale structures (for example, as polymer fibrils) is apparent in all polarized UV-Vis spectra (Fig. 4.11) where fibril formation is normally indicated by the presence of vibronic peaks next to the main electronic transition peak. Unfortunately, the attempts to induce F8BT polymer fibril formation via UV-irradiation, aging and ultrasonication proved unsuccessful. Conversely, the ease of polymer fibril formation in P3HT solutions has been very well studied.[185),194),195)] P3HT will therefore be used from now on as a proof-of-concept material to demonstrate that the preferential alignment of polymer chains in a specific direction using the SWC can be realized.

4.6 Spin coated and SWC P3HT films

4.6.1 Experimental

Two (2) grades of P3HT will be used in this study: (a) P3HT (EE97902 Lisicon SP001 supplied by Merck) with 96% regioregularity (RR), polydispersity index (PDI) of 1.9 and M_w of 43,600 g/mol and (b) P3HT (EF431002 Lisicon SP0016 supplied by Merck) with 99% RR, PDI of 4 and M_w of 197,600 g/mol. All P3HT solutions were prepared in the same manner: 5 mg/mL of P3HT in chloroform solvent were stirred at 55^{o}C for 60 minutes for complete dissolution of the solute followed by cooling to room temperature for 3 - 5 hrs. UV-irradiated

P3HT solutions stored in a quartz vial were irradiated with a handheld 254 nm wavelength UV-lamp (AXEL corp, 0.61 mW/cm^2 50 mm from source) while being stirred at 300 RPM for various time periods. Glass substrates were cleaned and treated with UV-Ozone (Section 3.5.1) prior to spin coating (SC) and SWC processes. SC samples were deposited at a rate of 1500 RPM for 60 s in air and SWC samples were prepared using the dual substrate setup as described in Fig. 4.8 (c) within the evaporative deposition regime of chloroform in a N_2 glovebox.

4.6.2 UV-Irradiation and uniaxial alignment of P3HT

Achieving high degrees of uniaxial alignment of polymer chains while employing MGC techniques for thin film deposition will require some degree of solution-state alignment/aggregation. Solution-state aggregation of P3HT chains have been well researched in literature and can be achieved via UV-irradiation. Past studies have shown that the aggregation state in solution survives the SC process, therefore P3HT films made from SC can be used to represent the solution-state molecular interactions between the P3HT chains.[194),195)] In this Section, we will investigate how UV-irradiation affects P3HT solution-state molecular interactions and uniaxial alignment of polymer chains during SWC.

The comparison between pristine and UV-irradiated P3HT solutions and their chemical structures are shown in Fig. 4.16 (a) and Fig. 4.16 (b), respectively. In the pristine light brown/orange P3HT, the ground state conformation of molecular

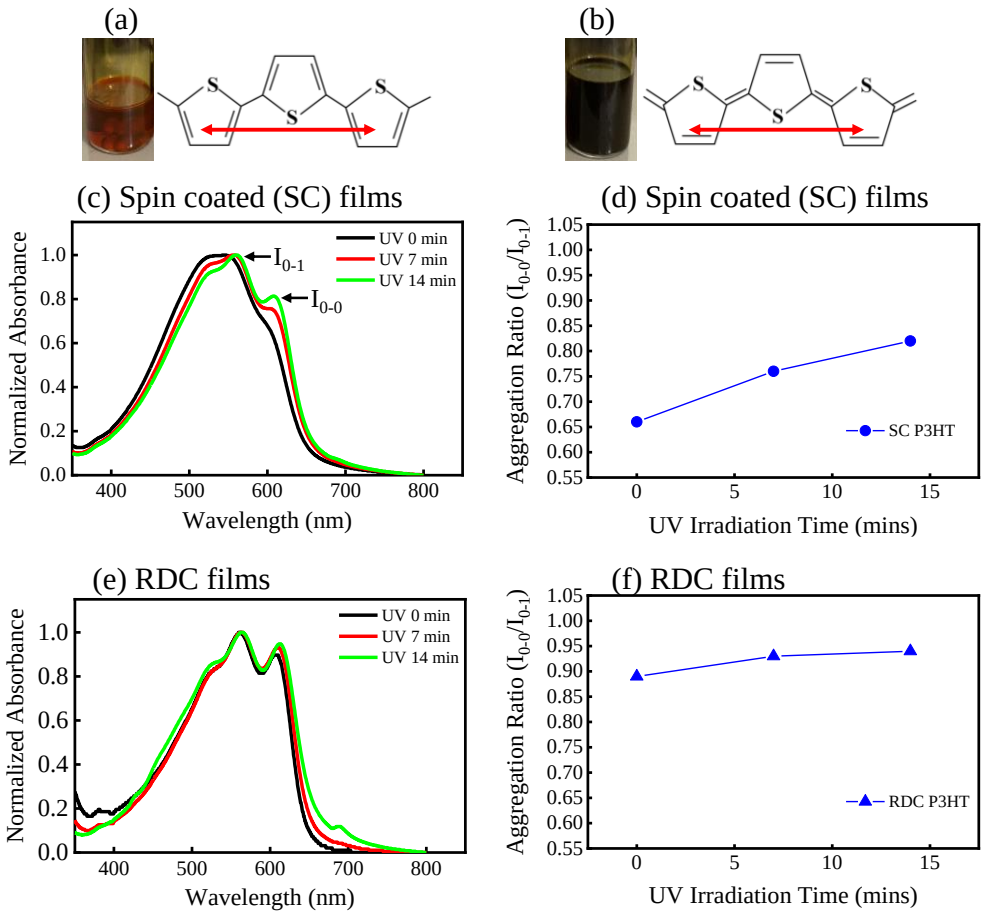

Fig. 4.16 Pictures of (a) pristine and (b) UV-irradiated P3HT solutions and their chemical structure. The red arrow indicates the direction of TDM. The normalized absorbance spectra of (c) SC and (e) SWC films were used to calculate the the aggregation ratio for (d) SC and (f) SWC films, respectively.

chains exhibit an “aromatic” like conformation. Due to the high twisting degree of freedom around the C-C bonds, the aromatic state is characterized by entangled conformation. The dark-brown UV-irradiated P3HT solution contains a higher

proportion of excited state “quinoidal” like conformation. The rigidity around the C=C bonds promote high degrees of backbone planarity and thus stronger intermolecular (π- π) interactions are made possible.[194] The TDM of P3HT is indicated by the red arrow in Fig. 4.16 and as confirmed in literature is parallel to the long backbone axis of the polymer chain.[187]

Characteristics of the intra- and inter-molecular interactions between P3HT chains are quantified by the intensities of their $I_{0\text{-}1}$ and $I_{0\text{-}0}$ peaks that represent a vibronic transition around 567 and 605 nm, respectively. The normalized UV-Vis absorption spectra of SC samples Fig. 4.16 (c)) shows a bathochromic shift of the $I_{0\text{-}1}$ peak and increasing intensity of the $I_{0\text{-}0}$ peak with increasing UV-irradiation time. This spectral feature is indicative of the aggregation of P3HT chains into nanofibrillar structures in solution. The strength of this intermolecular interaction can be quantified by the aggregation ratio ($I_{0\text{-}0}/I_{0\text{-}1}$) according to Spano’s H-aggregate model[196),197] as shown in Fig. 4.16 (d). With increasing UV-irradiation time, the aggregation ratio increases and indicates the increased nucleated growth of nanofibrillar structures under extended UV-irradiation exposure. SWC P3HT samples demonstrate very small increases in $I_{0\text{-}1}$ peak (Fig. 4.16 (e)) and aggregation ratio with increasing UV-irradiation time (Fig. 4.16 (f)) and may indicate nearing the saturation point at 14 minutes. Comparison between Fig. 4.16 (d) and Fig. 4.16 (f) show that SWC P3HT films generally demonstrate stronger

intermolecular interactions than SC ones. This suggests that the solution-state aggregation not only survives the SWC process, but it is enhanced by the evaporative assembly during SWC. Exploration into the mechanism behind this phenomenon will be explored in a later Section.

To support the results of Fig. 4.16, the AFM phase images of pristine- and UV-irradiated- SC and SWC films are shown in Fig. 4.17. The pristine spin coated films in Fig. 4.17 (a) show no discernible features, however after UV irradiation, small fibril formation features appear with undistinguishable orientation in Fig. 4.17 (b). All the SWC P3HT films demonstrate polymer fibril formation with the features being of larger size in UV-irradiated samples (Fig. 4.17 (d)) than in pristine ones (Fig. 4.17 (c)). The aggregation in the pristine SWC film is clearly supported

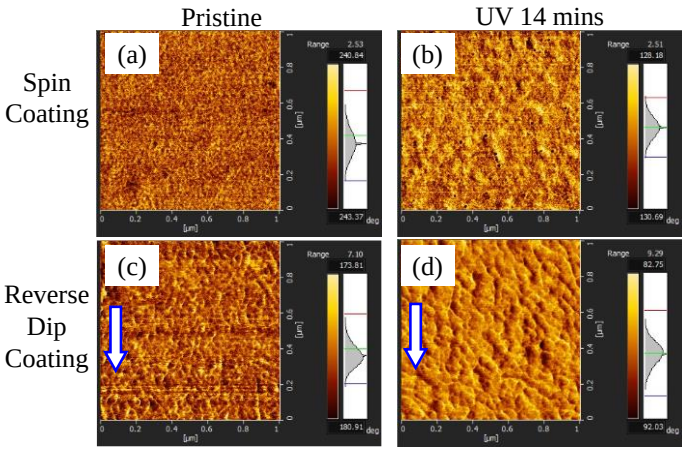

Fig. 4.17 AFM phase images of pristine (a) SC and (b) SWC films and 14 mins UV-irradiated (b) SC and (d) SWC P3HT films. The white arrows indicate the direction of solution withdrawal.

by evaporative driven self-assembly of polymer chains during the SWC process and indicate that the ground state-type aggregation forms fibrils of smaller dimensions. These results are therefore consistent with the aggregation ratio trends in Fig. 4.16 (d) and Fig. 4.16 (f) and confirm the physical formation of polymer nanofibrillar structures.

The effect of UV-irradiation time and nanofibrillar formation on the uniaxial orientation of polymer chains are shown in the polarized UV-vis absorbance spectra in Fig. 4.18. The spectral peaks at 567 nm were used to calculate the dichroic ratio and the results show that as the UV-irradiation time increases from 0 (Fig. 4.18 (b)) to 7 (Fig. 4.18 (d)) to 14 minutes (Fig. 4.18 (f)), the optical anisotropy increases linearly from 0.96 to 0.65 to 0.43. This indicates that the polymer chains exhibit preferential alignment in the direction perpendicular to the direction of solution withdrawal and is directly influenced by the UV-irradiation time. Coupled with the results from the AFM phase images which show that the fibrillar features in the UV-irradiated SWC sample demonstrate alignment in the general direction parallel to the solution withdrawal direction. The schematic images of P3HT chain orientation and polymer fibril formation are proposed and shown to the left of the polarized UV-vis absorption spectra where the polymer nanofibril consist of P3HT chains aggregating in a π-π stacking fashion.

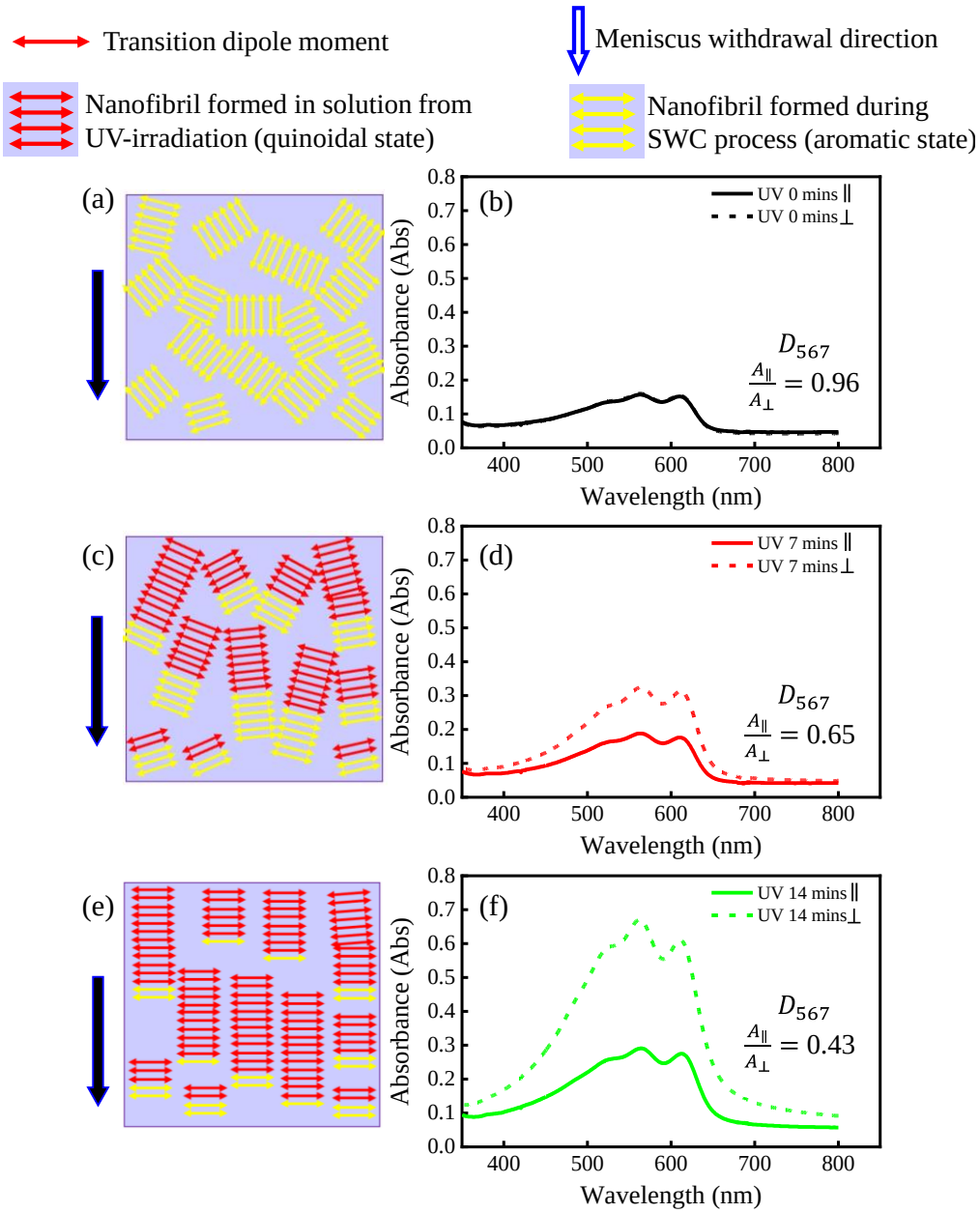

Fig. 4.18 Polarized UV-vis absorbance spectra of SWC P3HT films after UV-irradiation for (b) 0, (d) 7 and (f) 14 mins and their respective length and orientation of nanofibrils ((a), (c) and (d)) are shown in the schematic images on the left. The black arrow indicates the direction of solution withdrawal.

Although the presence of strong intermolecular interactions and formation of polymer fibrils exist in the pristine SWC P3HT sample, they demonstrate no optical anisotropy (Fig. 4.18 (a) and Fig. 4.18 (b)). This can be attributed to film formation and polymer chain aggregated growth occurring on simultaneously during SWC. The molecular interactions that may lead to the growth of polymer nanofibrils cannot be overcome and controlled by flow fields used to direct molecular chain alignment. Their spontaneous growth behind the meniscus line and immediate solidification will therefore lead to random orientation.

The 7- and 14-minute UV-irradiated SWC films show very similar aggregation ratios of 0.93 and 0.94 from Fig. 4.16 (f) but drastically different optical anisotropies of 0.65 (Fig. 4.18 (d)) and 0.43 (Fig. 4.18 (f)), respectively. The solution state aggregation ratio of 0.76 and 0.82 for 7- and 14- minute UV-irradiated SC films, respectively, suggest initially shorter nanofibrils in the 7-minute solution. During SWC for the 7-minute film there may exist competition between the extensional flow fields that maybe used to align the fibrils in the direction of solution withdrawal and nucleated growth of the fibrils themselves (like the situation that could not be overcome by the pristine SWC P3HT sample). Nanofibril growth and length in solution is nearer to saturation in the 14-minute UV-irradiated P3HT solution, thus extensional flow fields have less competition from nucleated-growth aggregation that is clearly enhanced during SWC. The

extensional flow fields can easily align the nanofibrils in the direction of solution withdrawal thus owing to the significantly higher optical anisotropy.

4.6.3 Uniqueness of P3HT aggregation in SWC

As mentioned in Section 4.7.2 and as shown in Fig. 4.16 (c) and Fig. 4.18 (b), pristine P3HT deposited via SWC demonstrates strong intermolecular interactions and the formation of polymer nanofibrils, despite their absence in solution (Fig. 4.16 (c)). This phenomenon in P3HT is unique to the SWC technique and to the best of our knowledge has not been demonstrated via other MGC techniques. Common in literature is that the formation of P3HT aggregates as nanofibrils solely occurs for UV-irradiated films and is absent in pristine films deposited from both spin coating and SWC.[194)] SWC therefore provides a new avenue for the realization of enhanced intermolecular interactions and nanofibril formation in P3HT.

It is well known in literature that low M_w P3HT readily forms nanofibril structures under the influence of aggregation drivers (ex. UV-irradiation, aging, ultrasonication, etc.) compared to high M_w P3HT. To elucidate the mechanisms behind aggregation during SWC, both low and high M_w pristine P3HT will be investigated. To verify whether the nanofibrils are formed behind the meniscus or within the bulk during SWC, the following experiment was done:

1. SWC procedure as normal for the deposition of P3HT film on glass substrate.
2. The collected solution in the glass syringe following step 1 was then used to fabricate a spin coated P3HT sample.

The collected solution therefore represents the aggregation state of P3HT chains within the bulk of the solution during SWC. Comparison between the SWC and SC films for low and high M_w P3HT are shown in Fig. 4.19 (a) and Fig. 4.19 (b), respectively. Common to both P3HT is that the SC film indicates negligible formation of nanofibrils due to low aggregation ratios of 0.61 and 0.52 in the low and high M_w P3HT, respectively. The SWC films indicate the presence of enhanced intermolecular interactions and formation of nanofibrils due to higher aggregation ratios of 0.97 and 0.85 in the low and high M_w P3HT, respectively. Although the high M_w P3HT has superior 99% RR, less entanglements in lower M_w P3HT imply easier formation of aggregated nanofibrils with high degrees of planarity. It is therefore logical to infer that the aggregation of pristine P3HT during SWC occurs behind the meniscus and not within the bulk of the solution and is independent of M_w.

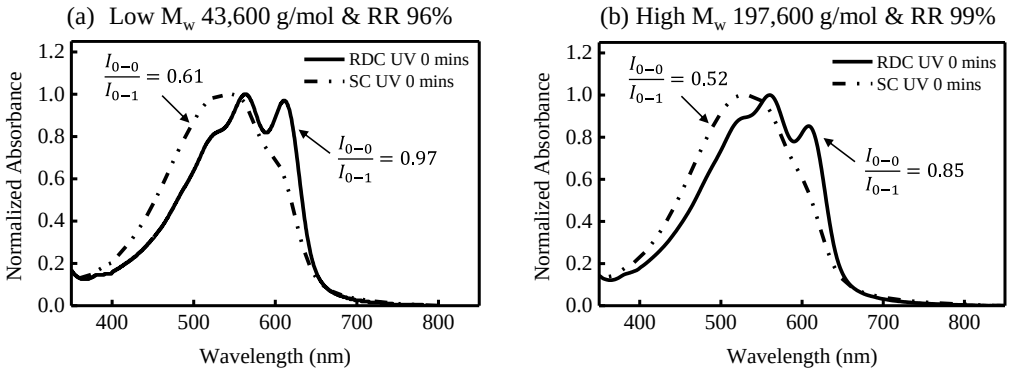

Fig. 4.19 Normalized UV-Vis absorbance spectra of (a) low and (b) high M_w P3HT deposited from SC and SWC.

Pristine P3HT films were deposited via SWC at various withdrawal speeds to investigate the influence of drying kinetics on molecular aggregation. The thicknesses of the SWC films were estimated using the absolute value of the UV-Vis absorption spectra peak at 567 nm and were used to confirm that withdrawal speeds across all 3 deposition regimes were investigated. The SWC film thickness for both low and high pristine M_w P3HT is shown in Fig. 4.20 (a) and their respective aggregation ratios are shown in Fig. 4.20 (b). Although the withdrawal speed changes the film formation dynamics, the aggregation ratio did not scale linearly to the changes in the resulting film thickness and withdrawal speed. This indicates that the aggregation during SWC is not influenced by drying kinetics. The nucleated growth of polymer fibrils during MGC may therefore rely on molecular level interactions where the formation of these structures are the most energetically feasible for self-assembly.

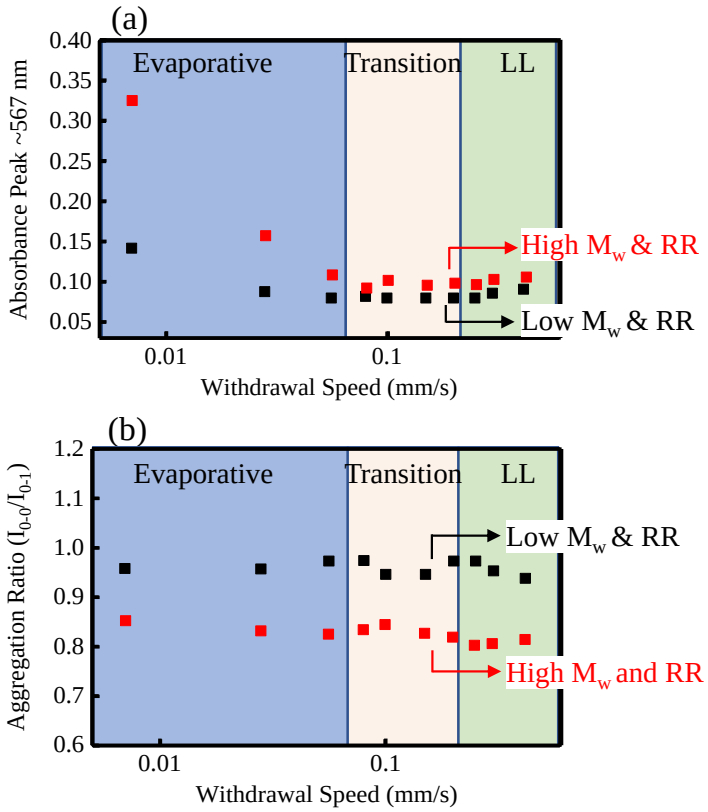

Fig. 4.20 (a) Estimated thickness using the absolute value of the UV-Vis absorbance peak at 567 nm and (b) aggregation ratio of low and high pristine M_w P3HT deposited at various speeds covering the evaporative, transition and LL regimes of deposition using chloroform solvent.

4.7 Conclusion

This work has shown the successful design of a SWC setup that can be used as a MGC technique to deposit thin film π-conjugated polymers that exhibit preferential alignment relative to the withdrawal direction of the solution. This simplicity in design of this technique is expected to be easily scalable to larger substrates for the realization of large-scale manufacturing and high throughput of OLEDs. P3HT was used as the proof-of-concept vehicle material since, via UV-irradiation, it demonstrated H-type aggregation of polymer chains in solution. This solution-state alignment prior to film deposition is the most important feature to realizing high degrees of orientation with SWC since the nanofibril features can be aligned via extensional flow fields during SWC. Dichroic ratios up to 0.43 (preferential perpendicular alignment of polymer chains) have been realized with SWC and are comparable to literature. Achieving solution-state alignment in emissive polymers used for OLED applications may require alternative techniques, for example, via the application of a voltage between the substrates to align the polymer chains in the direction of the E-Field and having them relax vertically down the substrate during SWC. Once this characteristic is realized, it is expected that achieving high η_{out} (due to reduced losses to evanescent modes) and linearly polarized emission (uniaxially aligned molecular chains and TDM) can be realized.

Chapter 5
Conclusions

This body of work investigated methods to improve the η_{out} in OLEDs within the scope of two major applications: general lighting and display. Considerations were made for investigating methods that were simple, cost-effective, scalable and realistic for their application in realistic large-scale fabrication conditions.

For general lighting applications, blurring of the emitted light is not of major concern therefore patterning techniques can be used and the air/glass interface was targeted. A simple single-step fs-laser (IMRA America Inc.) was used to pattern the air/glass interface of an OLED and demonstrated that the η_{out} could be enhanced by 31% and 61% due to the extraction of substrate guided modes in low and high transmittance devices, respectively. High scattering at the air/glass interface also proved useful for simultaneously decreasing the viewing angle dependence.

For display applications, patterning would not be appropriate since the overall image would be compromised thus materials-based solutions were targeted in solution processed OLED devices. By utilizing π-conjugated emissive polymer species, the η_{ext} could be enhanced thanks to enhancements in η_{out} via molecular chains being oriented horizontally relative to the *z*-axis and reduced losses to

evanescent modes (no preferential alignment in *x-y* plane). Exploration into uniaxial alignment was done via our simple and scalable SWC design for solution processed film formation with highly oriented molecular chains. P3HT was used as a proof-of-concept material and demonstrates that with solution-state aggregation, high degrees of uniaxial alignment in films may be achieved (dichroic ratio up to 0.43). This concept is expected to be useful for polymer EML materials used in OLEDs since uniaxial orientation of TDM produces LPE and this is essential for achieving highly efficient displays.

Bibliography

1) C. W. Tang and S. A. Vanslyke, Appl. Phys. Lett. **51** [12], 913 (1987).

2) A. Salehi, X. Fu, D. H. Shin and F. So, Adv. Funct. Mater. **29** [15], 1 (2019).

3) K. Saxena, V. K. Jain and D. S. Mehta, Opt. Mater. (Amst). **32** [1], 221 (2009).

4) B. Jiao, Y. Yu, Y. Dai, X. Hou and Z. Wu, Opt. Express **23** [4], 4055 (2015).

5) N. S. Kim, W. Y. Lee, B. Pyo and M. C. Suh, Org. Electron. **44**, 232 (2017).

6) M. C. Suh, B. Pyo and H. S. Kim, Org. Electron. physics, Mater. Appl. **28**, 31 (2016).

7) S. Lloyd, T. Tanigawa, H. Sakai and H. Murata, IEICE Trans Electron **E102-C** [2], 180 (2019).

8) S. Lloyd, K. Higashimine, T. Tanigawa and H. Murata, Jpn. J. Appl. Phys. **60**, SBBG01 (2021).

9) Y. Wang, M. Liu, J. Wang, Y. Zhang, Y. Qin, Y. Lu, Y. Chen, X. Zhang and W. Huang, Thin Solid Films **732** [June], 138791 (2021).

10) A. Senes, S. C. J. Meskers, H. Greiner, K. Suzuki, H. Kaji, C. Adachi, J. S.

Wilson and R. A. J. Janssen, J. Mater. Chem. C **5** [26], 6555 (2017).

11) L. S. Hung and C. H. Chen, Mater. Sci. Eng. R Reports **39** [5–6], 143 (2002).

12) B. Geffroy, P. le Roy and C. Prat, Polym. Int. **55** [6], 572 (2006).

13) Q. Wei, N. Fei, A. Islam, T. Lei, L. Hong, R. Peng, X. Fan, L. Chen, P. Gao and Z. Ge, Adv. Opt. Mater. **6** [20], 1 (2018).

14) R. Shinar and J. Shinar, J. Phys. Photonics **4**, 032002 (2022).

15) S. R. Forrest, D. D. C. Bradley and M. E. Thompson, Adv. Mater. **15** [13], 1043 (2003).

16) S. Y. Kim, W. I. Jeong, C. Mayr, Y. S. Park, K. H. Kim, J. H. Lee, C. K. Moon, W. Brütting and J. J. Kim, Adv. Funct. Mater. **23** [31], 3896 (2013).

17) J.-S. Kim, P. K. H. Ho and N. C. Greenham, J. Appl. Phys. **88**, 1073 (2000).

18) K. H. Kim and J. J. Kim, Adv. Mater. **30** [42], 1705600 (2018).

19) W. Brütting, J. Frischeisen, T. D. Schmidt, B. J. Scholz and C. Mayr, Phys. Status Solidi Appl. Mater. Sci. **210** [1], 44 (2013).

20) M. Furno, R. Meerheim, S. Hofmann, B. Lüssem and K. Leo, Phys. Rev. B **85**, 115205 (2012).

21) T. D. Schmidt, T. Lampe, M. R. Daniel Sylvinson, P. I. Djurovich, M. E. Thompson and W. Brütting, Phys. Rev. Appl. **8** [3], 1 (2017).

22) D. Ma, T. Tsuboi, Y. Qiu, L. Duan, D. Ma, Y. Qiu, L. Duan and T. Tsuboi, Adv. Mater. **29**, 1603253 (2016).

23) W. Zhao, Z. He, J. W. Y. Lam, Q. Peng, H. Ma, Z. Shuai, G. Bai, J. Hao and B. Z. Tang, Chem **1** [4], 592 (2016).

24) M. A. Baldo, D. F. O'brien, Y. You, A. Shoustikov, S. Sibley, M. E. Thompson and S. R. Forrest, Nature **395** [6698], 151 (1998).

25) J. Chen, W. Tao, W. Chen, Y. Xiao, K. Wang, C. Cao, J. Yu, S. Li, F. Geng, C. Adachi, C. Lee and X. Zhang, Angew. Chemie **131** [41], 14802 (2019).

26) T. Miwa, S. Kubo, K. Shizu, T. Komino, C. Adachi and H. Kaji, Sci. Rep. **7** [1], 1 (2017).

27) T. Tsutsui, M. Yahiro, H. Yokogawa, K. Kawano and M. Yokoyama, Adv. Mater [15], 1149 (2001).

28) M. K. Wei, C. W. Lin, C. C. Yang, Y. W. Kiang, J. H. Lee and H. Y. Lin, Int. J. Mol. Sci. **11** [4], 1527 (2010).

29) N. C. Greenham, R. H. Friend and D. D. C. Bradley, Adv. Mater. **6** [6], 491 (1994).

30) A. Chutinan, K. Ishihara, T. Asano, M. Fujita and S. Noda, Org. Electron. **6** [1], 3 (2005).

31) L. H. Smith, J. A. E. Wasey, I. D. W. Samuel and W. L. Barnes, Adv. Funct. Mater. **15** [11], 1839 (2005).

32) T. Bocksrocker, J. Benedikt Preinfalk, J. Asche-Tauscher, A. Pargner, C. Eschenbaum, F. Maier-Flaig, U. Lemmer, H. Kim, C. M. Gilmore, A. Piqué, J. S. Horwitz, H. Mattoussi, J. Murata, Z. H. Kafafi, D. B. Chrisey, J. Zhou, N. Ai, L. Wang, H. Zheng, C. Luo, Z. Jiang, S. Yu, Y. Cao and J. Wang, Opt. Express **20** [106], A932 (2012).

33) R. R. Chance, A. Prock and R. Silbey, J. Chem. Phys. **60** [7], 2749 (1974).

34) R. R. Chance, A. Prock and R. Silbey, J. Mol. Struct. **147** [1–2], 191 (1986).

35) K. A. Neyts, J. Opt. Soc. Am. A **15** [4], 962 (1998).

36) J. D. Jackson and R. F. Fox, *Classical Electrodynamics, 3rd ed.* (American Association of Physics TeachersAAPT, 1999) Vol. 67.

37) J. Song, H. Lee, E. Gyo Jeong, K. Cheol Choi, S. Yoo, J. Song, H. Lee, E. G. Jeong, K. C. Choi and S. Yoo, Adv. Mater. **32** [35], 1907539 (2020).

38) W. L. Barnes, J. Mod. Opt. **45** [4], 661 (1998).

39) S. Nowy, B. C. Krummacher, J. Frischeisen, N. A. Reinke and W. Brütting, J. Appl. Phys. **104** [12], 123109 (2008).

40) G. Gomard, J. B. Preinfalk, A. Egel and U. Lemmer, J. Photonics Energy **6**

[3], 030901 (2016).

41) M. (Anthony M. Fox, *Optical properties of solids* (Oxford University Press, New York, 2010) 2nd ed.

42) S. A. Maier, *Plasmonics: Fundamentals and applications* (Springer US, 2007).

43) A. Salehi, Y. Chen, X. Fu, C. Peng and F. So, ACS Appl. Mater. Interfaces **10**, 9595 (2018).

44) C. Fuchs, P.-A. Will, M. Wieczorek, M. C. Gather, S. Hofmann, S. Reineke, K. Leo and R. Scholz, Phys. Rev. B **92**, 245306 (2015).

45) P. A. Hobson, J. A. E. Wasey, I. Sage and W. L. Barnes, Sel. Top. Quantum Electron. IEEE J. **8** [2], 378 (2002).

46) M. Flämmich, M. C. Gather, N. Danz, D. Michaelis, A. H. Bräuer, K. Meerholz and A. Tünnermann, Org. Electron. physics, Mater. Appl. **11** [6], 1039 (2010).

47) Y. Y. Noh, J. J. Kim, Y. Yoshida and K. Yase, Adv. Mater. **15** [9], 699 (2003).

48) K. Meerholz and D. C. Müller, Adv. Funtional Mater. **11** [4], 251 (2001).

49) H. S. Kim, S. Il Moon, D. E. Hwang, K. W. Jeong, C. K. Kim, D. G. Moon and C. Hong, Opt. Laser Technol. **77**, 104 (2016).

50) S. Möller and S. R. Forrest, J. Appl. Phys. **91**, 3324 (2002).

51) T. W. Koh, J. M. Choi, S. Lee and S. Yoo, Adv. Mater. **22** [16], 1849 (2010).

52) J. Moon, E. Kim, S. K. Park, K. Lee, J. W. Shin, D. H. Cho, J. Lee, C. W. Joo, N. S. Cho, J. H. Han, B. G. Yu, S. Yoo and J. I. Lee, Org. Electron. **26**, 273 (2015).

53) J. Y. Oh, J. H. Kim, Y. K. Seo, C. W. Joo, J. Lee, J. I. Lee, S. Yu, C. Yun, M. H. Kang, B. H. Choi and Y. H. Kim, Dye. Pigment. **136**, 92 (2017).

54) Y.-S. Park, K.-H. Han, J. Kim, D.-H. Cho, J. Lee, Y. Han, J. T. Lim, N. S. Cho, B. Yu, J.-I. Lee and J.-J. Kim, Nanoscale **9** [1], 230 (2017).

55) Q. Yue, W. Li, F. Kong and K. Li, Adv. Mater. Sci. Eng. **2012**, 1 (2012).

56) J.-J. Kim, J. Lee, S.-P. Yang, H. G. Kim, H.-S. Kweon, S. Yoo and K.-H. Jeong, Nano Lett. **16** [5], 2994 (2016).

57) C.-H. Shin, E. Y. Shin, M.-H. Kim, J.-H. Lee and Y. Choi, Opt. Express **23** [3], A133 (2015).

58) T. Nakamura, H. Fujii, N. Juni and N. Tsutsumi, Opt. Rev. **13** [2], 104 (2006).

59) H.-W. Chang, K.-C. Tien, M.-H. Hsu, Y.-H. Huang, M.-S. Lin, C.-H. Tsai, Y.-T. Tsai and C.-C. Wu, J. Soc. Inf. Disp. **19** [2], 196 (2011).

60) T.-W. Koh, J. A. Spechler, K. M. Lee, C. B. Arnold and B. P. Rand, ACS

Photonics **2**, 1366 (2015).

61) T. Nakamura, N. Tsutsumi and N. Juni, J. Appl. Phys **97**, 54505 (2005).

62) S. Reineke, F. Lindner, G. Schwartz, N. Seidler, K. Walzer, B. Lüssem and K. Leo, Nature **459** [7244], 234 (2009).

63) S. Mladenovski, K. Neyts, D. Pavicic, A. Werner and C. Rothe, Opt. Express **17** [9], 7562 (2009).

64) Y. Sun and S. R. Forrest, Nat. Photonics **2** [8], 483 (2008).

65) T. Bocksrocker, F. Maier-Flaig, C. Eschenbaum and U. Lemmer, Opt. Express **20** [6], 6170 (2012).

66) Y. Qu, M. Slootsky and S. R. Forrest, Nat. Photonics **9** [11], 758 (2015).

67) D. H. Kim, J. Y. Kim, D. Y. Kim, J. H. Han and K. C. Choi, Org. Electron. physics, Mater. Appl. **15** [11], 3183 (2014).

68) J. Lee, Y. Y. Kwon, E.-H. Choi, J. Park, H. Yoon and H. Kim, Opt. Express **22** [S3], A705 (2014).

69) T.-B. Lim, K. H. Cho, Y.-H. Kim and Y.-C. Jeong, Opt. Express **24** [16], 17950 (2016).

70) S. Belousov, M. Bogdanova and A. Teslyuk, J. Phys. D. Appl. Phys. **49** [8], 85102 (2016).

71) K. Ishihara, M. Fujita, I. Matsubara, T. Asano, S. Noda, H. Ohata, A. Hirasawa, H. Nakada and N. Shimoji, Appl. Phys. Lett. **90** [11], 111114 (2007).

72) Q. D. Ou, L. Zhou, Y. Q. Li, S. Shen, J. De Chen, C. Li, Q. K. Wang, S. T. Lee and J. X. Tang, Adv. Funct. Mater. **24** [46], 7249 (2014).

73) B. Riedel, I. Kaiser, J. Hauss, U. Lemmer and M. Gerken, Opt. Express **18** [S4], A631 (2010).

74) C. Y. Chen, W. K. Lee, Y. J. Chen, C. Y. Lu, H. Y. Lin and C. C. Wu, Adv. Mater. **27** [33], 4883 (2015).

75) W. Youn, J. Lee, M. Xu, R. Singh and F. So, ACS Appl. Mater. Interfaces **7** [17], 8974 (2015).

76) S. Y. Kim and J. J. Kim, Org. Electron. physics, Mater. Appl. **11** [6], 1010 (2010).

77) C. L. Lin, T. Y. Cho, C. H. Chang and C. C. Wu, Appl. Phys. Lett. **88** [8], 081114 (2006).

78) J. B. Kim, J. H. Lee, C. K. Moon, S. Y. Kim and J. J. Kim, Adv. Mater. **25** [26], 3571 (2013).

79) L. H. Smith and W. L. Barnes, Org. Electron. **7** [6], 490 (2006).

80) C. W. Y. Law, K. S. Wong, Z. Yang, L. E. Horsburgh and A. P. Monkman, Appl. Phys. Lett. **76** [11], 1416 (2000).

81) C. Mayr, S. Y. Lee, T. D. Schmidt, T. Yasuda, C. Adachi and W. Brütting, Adv. Funct. Mater. **24** [33], 5232 (2014).

82) D. H. Kim, K. Inada, L. Zhao, T. Komino, N. Matsumoto, J. C. Ribierre and C. Adachi, J. Mater. Chem. C **5** [5], 1216 (2017).

83) J. Frischeisen, Q. Niu, A. Abdellah, J. B. Kinzel, R. Gehlhaar, G. Scarpa, C. Adachi, P. Lugli and W. Brütting, Opt. Express **19** [101], A7 (2010).

84) H.-W. Chang, J. Lee and S. Hofmann, J. Appl. Phys **113**, 204502 (2013).

85) C. Dong, X. Fu, L. Cao, S. Amoah, K. Gundogdu, J. Li and F. So, ACS Appl. Mater. Interfaces **12** [28], 31667 (2020).

86) U. Geyer, J. Hauss and B. Riedel, J. Appl. Phys **104**, 93111 (2008).

87) B. Riedel, J. Hauss and U. Geyer, Appl. Phys. Lett **96**, 243302 (2010).

88) J. Hauss, T. Bocksrocker and B. Riedel, Appl. Phys. Lett **99**, 103303 (2011).

89) L. Ye, X. Jiao, M. Zhou, S. Zhang, H. Yao, W. Zhao, A. Xia, H. Ade and J. Hou, Adv. Mater. **27** [39], 6046 (2015).

90) M. T. Lee, C. L. Wang, C. S. Chan, C. C. Fu, C. Y. Shih, C. C. Chen, K. H. Lin, Y. H. Chen, W. J. Su, C. H. Liu, C. M. Ko, Z. X. Weng, J. H. Lin, Y. C.

Chin, C. Y. Chen, Y. C. Chang, A. T. Y. Huang, H. H. Lu and Y. H. Lin, SID Symp. Dig. Tech. Pap. **25** [4], 229 (2017).

91) K. Watanabe, Y. Iwaki, Y. Uchida, D. Nakamura, H. Ikeda, M. Katayama, T. Cho, H. Miyake, Y. Hirakata and S. Yamazaki, J. Soc. Inf. Disp. **24** [1], 12 (2016).

92) Y. Jeon, H. R. Choi, M. Lim, S. Choi, H. Kim, J. H. Kwon, K. C. Park and K. C. Choi, Adv. Mater. Technol. **3** [5], 1700391 (2018).

93) W. Kim, S. Kwon, S. M. Lee, J. Y. Kim, Y. Han, E. Kim, K. C. Choi, S. Park and B. C. Park, Org. Electron. **14** [11], 3007 (2013).

94) Y. Huang, E.-L. Hsiang, M.-Y. Deng and S.-T. Wu, Light Sci. Appl. **9** [1], 1 (2020).

95) D. Wang, J. Hauptmann and C. May, MRS Adv. **4** [24], 1367 (2019).

96) Y. Chen, J. Wang, Z. Zhong, Z. Jiang, C. Song, Z. Hu, J. Peng, J. Wang and Y. Cao, Org. Electron. **37**, 458 (2016).

97) W. H. Kim, A. J. Mäkinen, N. Nikolov, R. Shashidhar, H. Kim and Z. H. Kafafi, Appl. Phys. Lett. **80** [20], 3844 (2002).

98) Y. M. Xie, Q. Sun, T. Zhu, L. S. Cui, F. Liang, S. W. Tsang, M. K. Fung and L. S. Liao, Org. Electron. **55**, 1 (2018).

99) Y. J. Wang, J. G. Lu and H. P. D. Shieh, IEEE Photonics J. **8** [1], 1 (2016).

100) W. Sekundo, K. S. Kunert and M. Blum, Br. J. Ophthalmol. **95** [3], 335 (2011).

101) H. Nishiyama, M. Mizoshiri, T. Kawahara, J. Nishii and Y. Hirata, Opt. Express **16** [22], 17288 (2008).

102) K. Koenig, I. Riemann, P. Fischer and K. J. Halbhuber, Cell. Mol. Biol. **45** [2], 195 (1999).

103) Y. Kondo, J. Qiu, T. Mitsuyu, K. Hirao and T. Yoko, Jpn. J. Appl. Phys. **38**, L1146 (1999).

104) M. Masuda, ✉ K Sugioka, Y. Cheng, N. Aoki, M. Kawachi, K. Shihoyama, K. Toyoda, H. Helvajian and K. Midorikawa, Appl. Phys. A **76** [5], 857 (2003).

105) R. R. Gattass and E. Mazur, Nat. Photonics **2** [4], 219 (2008).

106) H. Liang, W. H. Wright, S. Cheng, W. He and M. W. Berns, *Exp. Cell Res.*, 1993, 204, 110–120.

107) A. Physics, B. A. Vogel, J. Noack and G. Paltauf, Appl. Phys. A **76** [5], 857 (2005).

108) Z. Lin and M. Hong, Ultrafast Sci. **2021**, 1 (2021).

109) R. Santbergen and R. J. C. van Zolingen, Energy Convers. Manag. **47** [20], 3572 (2006).

110) T. Lanz, K. Lapagna, S. Altazin, M. Boccard, F.-J. Haug, C. Ballif and B. Ruhstaller, Opt. Express **23** [11], A539 (2015).

111) S. Altazin, C. Reynaud, U. M. Mayer, T. Lanz, K. Lapagna, R. Knaack, L. Penninck, C. Kirsch, K. P. Pernstich, S. Harkema, D. Hermes and B. Ruhstaller, SID Symp. Dig. Tech. Pap. **46** [1], 564 (2015).

112) J. A. Mayer, University of Basel (2017).

113) S. Altazin, L. Stepanova, J. Werner, B. Niesen, C. Ballif and B. Ruhstaller, Opt. Commun. **26** [10], A579 (2018).

114) J. Lee, B. J. Jung, J. I. Lee, H. Y. Chu, L. M. Do and H. K. Shim, J. Mater. Chem. **12** [12], 3494 (2002).

115) E. Salsberg and H. Aziz, Org. Electron. **69** [2018], 313 (2019).

116) S. Liu, H. Yu, Q. Zhang, F. Qin, X. Zhang, L. Zhang and W. Xie, J. Mater. Chem. C **7** [18], 5426 (2019).

117) S. Piravadili Mucur and E. Tekin, Turkish J. Phys. **42** [1], 1 (2018).

118) A. M. Nardes, M. Kemerink, M. M. de Kok, E. Vinken, K. Maturova and R. A. J. Janssen, Org. Electron. **9**, 727 (2008).

119) A. Cester, D. Bari, J. Framarin, N. Wrachien, G. Meneghesso, S. Xia, V. Adamovich and J. J. Brown, Microelectron. Reliab. **50**, 1866 (2010).

120) C. Giebeler, H. Antoniadis, D. D. C. Bradley and Y. Shirota, J. Appl. Phys. **85** [1], 608 (1999).

121) S. L. M. van Mensfoort, V. Shabro, R. J. de Vries, R. A. J. Janssen and R. Coehoorn, J. Appl. Phys. **107**, 113710 (2010).

122) S. Barth, P. Müller and H. Riel, J. Appl. Phys. **89**, 3711 (2000).

123) H. Aziz, Z. D. Popovic, N.-X. Hu, A.-M. Hor and G. Xu, Science (80-.). **283** [5409], 1900 (1999).

124) S. Naka, H. Okada, H. Onnagawa, J. Kido and T. Tsutsui, Jpn. J. Appl. Phys. **38**, L1252 (1999).

125) K. Narayan, S. Varadharajaperumal, G. Mohan Rao, M. Manoj Varma and T. Srinivas, Curr. Appl. Phys. **13** [1], 18 (2013).

126) C.-I. Wu, G.-R. Lee and W. Pi, J. Appl. Phys. **87**, 212108 (2005).

127) H. Heil, J. Steiger and S. Karg, J. Appl. Phys. **89**, 420 (2001).

128) B. Ofuonye, J. Lee, M. Yan, C. Sun, J. M. Zuo and I. Adesida, Semicond. Sci. Technol. **29** [9], 095005 (2014).

129) G. E. Jabbour, B. Kippelen, N. R. Armstrong and N. Peyghambarian, Appl.

Phys. Lett. **73** [9], 1185 (1998).

130) G. E. Jabbour, Y. Kawabe, S. E. Shaheen, J. F. Wang, M. M. Morrell, B. Kippelen and N. Peyghambarian, Appl. Phys. Lett. **71** [13], 1762 (1997).

131) S. E. Shaheen, G. E. Jabbour, M. M. Morrell, Y. Kawabe, B. Kippelen, N. Peyghambarian, M. F. Nabor, R. Schlaf, E. A. Mash and N. R. Armstrong, J. Appl. Phys. **84** [4], 2324 (1998).

132) D. Yamashita, A. Ishizaki and T. Yamamoto, Mater. Trans. **56** [9], 1445 (2015).

133) S. Y. Kim, J.-L. Lee, K.-B. Kim and Y.-H. Tak, J. Appl. Phys. **95** [5], 2560 (2004).

134) T. Hu, F. Zhang, Z. Xu, S. Zhao, X. Yue and G. Yuan, Synth. Met. **159**, 754 (2009).

135) A. P. Ghosh, L. J. Gerenser, C. M. Jarman and J. E. Fornalik, Appl. Phys. Lett **86**, 223503 (2005).

136) J. H. Park, S. D. Baek, J. Il Cho, J. Y. Yoo, S. Y. Yoon, S. Kim, S. Lee, Y. S. Kim and J. M. Myoung, Compos. Part B Eng. **175**, 107188 (2019).

137) K. Fehse, K. Walzer, K. Leo, W. Lövenich and A. Elschner, Adv. Mater. **19** [3], 441 (2007).

138) C. Hippola, R. Kaudal, E. Manna, T. Xiao, A. Peer, R. Biswas, W. Dennis Slafer, T. Trovato, J. Shinar, R. Shinar, C. Hippola, R. Kaudal, T. Xiao, R. Biswas, J. Shinar, E. Manna, A. Peer, R. Shinar and W. D. Slafer, Adv. Opt. Mater. **6**, 1701244 (2018).

139) Y. Chen, N. Zhang, Y.-F. Li, Y.-G. Bi, Y.-Y. Yue, J. Feng and H.-B. Sun, Adv. Opt. Mater. **6**, 1701348 (2018).

140) L. Zhou, Q.-D. Ou, J.-D. Chen, S. Shen, J.-X. Tang, Y.-Q. Li and S.-T. Lee, Sci. Rep. **4** [1], 1 (2014).

141) H. K. Raut, S. S. Dinachali, Y. C. Loke, R. Ganesan, K. K. Ansah-Antwi, K. Ansah-Antwi, A. Góra, E. H. Khoo, V. A. Ganesh, M. S. M. Saifullah and S. Ramakrishna, ACS Nano **9** [1], 1305 (2015).

142) D. Yokoyama, J. Mater. Chem. **21** [48], 19187 (2011).

143) M. Brinkmann, G. Gadret, M. Muccini, C. Taliani, N. Masciocchi and A. Sironi, J. Am. Chem. Soc. **122** [21], 5147 (2000).

144) T. Gavrilko, R. Fedorovich, G. Dovbeshko, A. Marchenko, A. Naumovets, V. Nechytaylo, G. Puchkovska, L. Viduta, J. Baran and H. Ratajczak, J. Mol. Struct. **704** [1–3], 163 (2004).

145) K. Bagchi, N. E. Jackson, A. Gujral, C. Huang, M. F. Toney, L. Yu, J. J. De Pablo and M. D. Ediger, J. Phys. Chem. Lett. **10** [2], 164 (2019).

146) X. Liang, Z. L. Tu and Y. X. Zheng, Chem. - A Eur. J. **25** [22], 5623 (2019).

147) M. Vasilopoulou, A. Rashid bin Mohd Yusoff, M. Daboczi, J. Conforto, A. Emanuel Ximim Gavim, W. Jose da Silva, A. Gerniski Macedo, A. Soultati, G. Pistolis, F. Kurt Schneider, Y. Dong, P. Jacoutot, G. Rotas, J. Jang, G. C. Vougioukalakis, C. L. Chochos, J.-S. Kim and N. Gasparini, Nat. Commun. **12** [1], 1 (2021).

148) T. Komino, H. Tanaka and C. Adachi, Chem. Mater **26**, 3671 (2014).

149) H. Jung, S. Kang, H. Lee, Y.-J. Yu, J. H. Jeong, J. Song, Y. Jeon and J. Park, ACS Appl. Mater. Interfaces **10**, 30022 (2018).

150) M.-C. Tang, W.-K. Kwok, S.-L. Lai, W.-L. Cheung, M.-Y. Chan, V. Wing and W. Yam, Chem. Sci. **10**, 594 (2019).

151) T. Marcato and C. J. Shih, Helv. Chim. Acta **102** [5], e1900048 (2019).

152) H. W. Chen, J. H. Lee, B. Y. Lin, S. Chen and S. T. Wu, Light Sci. Appl. **7** [3], 17168 (2018).

153) H. Chen, G. Tan and S.-T. Wu, Opt. Express **25** [26], 33643 (2017).

154) R. Singh, K. N. Narayanan Unni, A. Solanki and Deepak, Opt. Mater. (Amst). **34** [4], 716 (2012).

155) G. J. Choi, Q. Van Le, K. S. Choi, K. C. Kwon, H. W. Jang, J. S. Gwag and

S. Y. Kim, Adv. Mater. **29** [36], 1 (2017).

156) G. Tan, R. Zhu, Y. S. Tsai, K. C. Lee, Z. Luo, Y. Z. Lee and S. T. Wu, Dig. Tech. Pap. - SID Int. Symp. **47** [1], 1509 (2016).

157) X. Wu, G. Xie, C. P. Cabry, X. Xu, S. J. Cowling, D. W. Bruce, W. Zhu, E. Baranoff and Y. Wang, J. Mater. Chem. C **6** [13], 3298 (2018).

158) J. Koo, S. I. Lim, S. H. Lee, J. S. Kim, Y. T. Yu, C. R. Lee, D. Y. Kim and K. U. Jeong, Macromolecules **52** [4], 1739 (2019).

159) K. Sakamoto, K. Miki, M. Misaki, K. Sakaguchi, M. Chikamatsu and R. Azumi, Appl. Phys. Lett. **91** [18], 2005 (2007).

160) M. Y. Lin, H. H. Chen, K. H. Hsu, Y. H. Huang, Y. J. Chen, H. Y. Lin, Y. K. Wu, L. A. Wang, C. C. Wu and S. C. Lee, IEEE Photonics Technol. Lett. **25** [14], 1321 (2013).

161) X. Gu, L. Shaw, K. Gu, M. F. Toney and Z. Bao, Nat. Commun. **9** [1], 1 (2018).

162) S. I. Jo, Y. Kim, J. H. Baek, C. J. Yu and J. H. Kim, Jpn. J. Appl. Phys. **53** [3], 03CD04 (2014).

163) D.-M. Lee, J.-H. Jung, Y.-J. Lee, C. Yu and J.-H. Kim, SID Symp. Dig. Tech. Pap. **48** [1], 2018 (2017).

164) H. Zhang, Q. Zhang, Q. Zhang, H. Sun, G. Hai, J. Tong, H. Xu and R. Xia, Chinese Phys. B **28** [7], 078108 (2019).

165) B. H. Lee, B. B. Y. Hsu, S. N. Patel, J. Labram, C. Luo, G. C. Bazan and A. J. Heeger, Nano Lett. **16** [1], 314 (2016).

166) Z. Zheng, K. H. Yim, M. S. M. Saifullah, M. E. Welland, R. H. Friend, J. S. Kim and W. T. S. Huck, Nano Lett. **7** [4], 987 (2007).

167) X. H. Li, X. Z. Shen, X. Gao and Y. Y. Weng, RSC Adv. **7** [88], 55885 (2017).

168) M. Misaki, Y. Ueda, S. Nagamatsu, M. Chikamatsu, Y. Yoshida, N. Tanigaki and K. Yase, Appl. Phys. Lett. **87** [24], 1 (2005).

169) Y. Diao, L. Shaw, Z. Bao and S. C. B. Mannsfeld, Energy Environ. Sci. **7** [7], 2145 (2014).

170) B. B. Patel and Y. Diao, Nanotechnology **29** [4], 044004 (2018).

171) J. H. Li, Y. Xi, L. D. Pozzo, J. T. Xu and C. K. Luscombe, J. Mater. Chem. C **5** [21], 5128 (2017).

172) L. Shaw, P. Hayoz, Y. Diao, J. A. Reinspach, J. W. F. To, M. F. Toney, R. T. Weitz and Z. Bao, ACS Appl. Mater. Interfaces **8** [14], 9285 (2016).

173) G. Qu, X. Zhao, G. M. Newbloom, F. Zhang, E. Mohammadi, J. W. Strzalka,

L. D. Pozzo, J. Mei and Y. Diao, ACS Appl. Mater. Interfaces **9** [33], 27863 (2017).

174) S. Nikzad, H. C. Wu, G. J. N. Wang, H. Yan, S. A. Schneider, M. F. Toney and Z. Bao, ACS Appl. Electron. Mater. **1** [11], 2445 (2019).

175) F. Molina-Lopez, H. Yan, X. Gu, Y. Kim, M. F. Toney and Z. Bao, Adv. Funct. Mater. **27** [8], 1605503 (2017).

176) F. Molina-Lopez, H. C. Wu, G. J. N. Wang, H. Yan, L. Shaw, J. Xu, M. F. Toney and Z. Bao, Adv. Electron. Mater. **4** [7], 1 (2018).

177) J. Soeda, T. Uemura, T. Okamoto, C. Mistui, M. Yamagishi and J. Takeya, Appl. Phys. Express **6**, 76503 (2013).

178) T. Sakata, D. Kajiya and K. I. Saitow, ACS Appl. Mater. Interfaces **12**, 46598 (2020).

179) K. Zhang, Z. Wang, T. Marszalek, M. Borkowski, G. Fytas, P. W. M. Blom and W. Pisula, Mater. Horizons **7** [6], 1631 (2020).

180) X. Liu, Y. Zhang, X. Zhang, R. Li and W. Hu, Sci. China Mater. **63** [7], 1257 (2020).

181) Q. Zhang, Q. Wei, X. Guo, G. Hai, H. Sun, J. Li, R. Xia, Y. Qian, S. Casado, J. R. Castro-Smirnov and J. Cabanillas-Gonzalez, Adv. Sci. **6** [1], 1801455

(2019).

182) S. Lee, B. R. Lee, J. S. Kim and M. H. Song, J. Mater. Chem. C **2** [41], 8673 (2014).

183) V. Vohra, Y. Matsunaga, T. Takada, A. Kiyokawa, L. Barba and W. Porzio, Small **17** [2], 2004168 (2021).

184) G. Luo, X. Ren, S. Zhang, H. Wu, W. C. H. Choy, Z. He and Y. Cao, Small **12** [12], 1547 (2016).

185) N. Kleinhenz, C. Rosu, S. Chatterjee, M. Chang, K. Nayani, Z. Xue, E. Kim, J. Middlebrooks, P. S. Russo, J. O. Park, M. Srinivasarao and E. Reichmanis, Chem. Mater. **27** [7], 2687 (2015).

186) M. C. Gather and D. D. C. Bradley, Adv. Funct. Mater. **17** [3], 479 (2007).

187) B. O'Connor, R. J. Kline, B. R. Conrad, L. J. Richter, D. Gundlach, M. F. Toney and D. M. DeLongchamp, Adv. Funct. Mater. **21** [19], 3697 (2011).

188) L. Sardone, C. Sabatini, G. Latini, F. Barigelletti, G. Marletta, F. Cacialli and P. Samorì, J. Mater. Chem. **17** [14], 1387 (2007).

189) D. Z. Garbuzov, V. Bulović, P. E. Burrows and S. R. Forrest, Chem. Phys. Lett. **249** [5–6], 433 (1996).

190) C. Pérez-Bolívar, S. Y. Takizawa, G. Nishimura, V. A. Montes and P.

Anzenbacher, Chem. - A Eur. J. **17** [33], 9076 (2011).

191) M. Le Berre, Y. Chen and D. Baigl, Langmuir **25** [5], 2554 (2009).

192) H. N. Tsao, D. Cho, J. W. Andreasen, A. Rouhanipour, D. W. Breiby, W. Pisula and K. Müllen, Adv. Mater. **21** [2], 209 (2009).

193) K. Ali, U. Pietsch and S. Grigorian, J. Appl. Crystallogr. **46** [4], 908 (2013).

194) P. H. Chu, N. Kleinhenz, N. Persson, M. McBride, J. L. Hernandez, B. Fu, G. Zhang and E. Reichmanis, Chem. Mater. **28** [24], 9099 (2016).

195) A. R. Aiyar, J. Il Hong, J. Izumi, D. Choi, N. Kleinhenz and E. Reichmanis, ACS Appl. Mater. Interfaces **5** [7], 2368 (2013).

196) M. Chang, J. Lee, P.-H. Chu, D. Choi, B. Park and E. Reichmanis, ACS Appl. Mater. Interfaces **6**, 21541 (2014).

197) J. Clark, J.-F. Chang and F. C. Spano, Appl. Phys. Lett **94**, 163306 (2009).

Published Journal Papers

[1] **Savanna Lloyd**, Koichi Higashimine, Tatsuya Tanigawa and Hideyuki Murata, "Optimized Femtosecond laser patterning of organic light-emitting diode substrates for the extraction of substrate guided modes", Japanese Journal of Applied Physics, **60 (SB)**, SBBG01, January 2021.

[2] Duy Cong Le, Duong Dai Nguyen, **Savanna Lloyd**, Toshi-kazu Suzuki and Hideyuki Murata, "Degradation of fluorescent organic light-emitting diodes caused by quenching of singlet and triplet excitons", Journal of Materials Chemistry C, **8**, 14873-14879, October 2020.

[3] **Savanna Lloyd**, Tatsuya Tanigawa, Heisuke Sakai and Hideyuki Murata, "Patterning of OLED glass substrate for improving light outcoupling efficiency", IEICE Transactions on Electronics, E102-C, 180-183, February 2019.

[4] Takahiro Takumi, **Savanna Lloyd**, Hideyuki Murata and Varun Vohra, "Low-cost manipulation coatings for polymer solar cell photocurrent increase under various incident angles", Materials Research Letters, **7(2)**, 68-74, January 2019.

Conferences

1. SPIE Photonics Europe International Symposium (**May 2022**)

   Virtual Forum

   "Patterning of organic light-emitting diode substrates for the simultaneous enhancement of the outcoupling efficiency and reduction of spectral shifting".

   Savanna Lloyd, Koichi Higashimine, Tatsuya Tanigawa, Hideyuki Murata.

2. 16th Study Group on Organic Electronic Devices and Physical Characteristics (**August 2021**)

   Virtual Forum

   "Femtosecond laser patterning of organic light-emitting diode substrates for the simultaneous enhancement of outcoupling efficiency and reduction of spectral shifting".

   Savanna Lloyd, Tatsuya Tanigawa and Hideyuki Murata,

3. 12th Asian Conference on Organic Electronics (A-COE) (**November 2020**)

   Virtual Forum

   "Substrate patterning of organic light-emitting diodes for enhancement of the outcoupling efficiency and reduction of spectral shifting simultaneously".

Savanna Lloyd, Koichi Higashimine, Tatsuya Tanigawa and Hideyuki Murata.

4. 52nd International Conference on Solid State Devices and Materials (SSDM) (**September 2020**)

   Virtual Forum

   "Femtosecond laser patterning of organic light emitting diode substrates for the enhancement of outcoupling efficiency".

   Savanna Lloyd, Koichi Higashimine, Tatsuya Tanigawa and Hideyuki Murata.

5. SPIE Photonics Europe International Symposium (**March 2020**)

   Virtual Forum

   A micrometer scale patterning of OLED substrates for the enhancement of outcoupling efficiency by the redirection of substrate and organic waveguided modes.

   Savanna Lloyd, Koichi Higashimine, Tatsuya Tanigawa and Hideyuki Murata.

6. 66th Japan Society of Applied Physics (JSAP) Spring Meeting (**March 2019**)

   Tokyo Institute of Technology, Ookayama Campus, Tokyo, Japan

   "Design of OLED glass patterns for enhanced outcoupling efficiency and good colour stability".

   Savanna Lloyd, Tatsuya Tanigawa, Heisuke Sakai and Hideyuki Murata.

7. 10th International Symposium on Organic Molecular Electronics (ISOME)

   (**June 2018**)

   Sunmesse Tosu, Saga, Japan.

   "Patterning of OLED glass substrate for improving outcoupling efficiency".

   Savanna Lloyd, Tatsuya Tanigawa, Heisuke Sakai and Hideyuki Murata.